Measurement of Inelastic Charmonium Production at HERA

by

Michael Steder

Measurement of Inelastic Charmonium Production at HERA

Dissertation

zur Erlangung des Doktorgrades
des Department Physik
der Universität Hamburg

vorgelegt von

MICHAEL STEDER

aus Lübeck

Hamburg
2008

Gutachter der Dissertation:	PD Dr. Andreas Meyer Prof. Dr. Robert Klanner
Gutachter der Disputation:	PD Dr. Andreas Meyer JProf. Dr. Johannes Haller
Datum der Disputation:	27. August 2008
Vorsitzender des Prüfungsausschusses:	PD Dr. Michael Martins
Vorsitzender des Promotionsausschusses:	Prof. Dr. Joachim Bartels
Dekan der MIN Fakultät:	Prof. Dr. Arno Frühwald
Leiter des Department Physik:	Prof. Dr. Robert Klanner

Kurzfassung

Diese Arbeit präsentiert die Ergebnisse der Messungen inelastischer J/Ψ Mesonen in Photoproduktion und tief inelastischer Streuung bei HERA. Die Daten wurden mit dem H1 Experiment während der HERA II Datennahmeperiode aufgezeichnet. Der untersuchte Photoproduktions-Datensatz entspricht einer integrierten Luminosität von $\mathcal{L} \approx 315\ \mathrm{pb}^{-1}$, während für die Elektroproduktionsanalyse Daten mit einer integrierten Luminosität von $\mathcal{L} \approx 166\ \mathrm{pb}^{-1}$ verwendet wurden. Beide Analysen werden in einem mittleren Elastizitätsbereich der J/Ψ Mesonen ($0.3 \leqslant \mathrm{z} \leqslant 0.9$) durchgeführt. Der kinematische Bereich der Photoproduktionsanalyse ist definiert durch $\mathrm{Q}^2 \approx 0\,\mathrm{GeV}^2$, $60 \leqslant \mathrm{W}_{\gamma p} \leqslant 240\,\mathrm{GeV}$ und $\mathrm{P}_{\mathrm{T},\Psi} \geqslant 1\,\mathrm{GeV}^2$, wohingegen die Untersuchung der Elektroproduktion auf $3.6 \leqslant \mathrm{Q}^2 \leqslant 100\,\mathrm{GeV}^2$, $50 \leqslant \mathrm{W}_{\gamma p} \leqslant 225\,\mathrm{GeV}$ und $\mathrm{P}^*_{\mathrm{T},\Psi} \geqslant 1\,\mathrm{GeV}$ beschränkt ist. Hierbei bezeichnet $\mathrm{P}^*_{\mathrm{T},\Psi}$ den Transversalimpuls des J/Ψ Mesons im γp Schwerpunktsystem.

In beiden kinematischen Bereichen werden einfach und doppelt differentielle Wirkungsquerschnitte mit verbesserter Genauigkeit im Vergleich zu früheren Analysen gemessen. Die Polarisation der erzeugten J/Ψ Mesonen wird mit Hilfe einer Anpassung an die Zerfallswinkelverteilungen $\cos(\Theta^*)$ und ϕ^* untersucht.

Die gemessenen Wirkungsquerschnitte werden mit verschiedenen theoretischen Vorhersagen verglichen. Die erfolgreichste Beschreibung der Daten gelingt einem Modell, das einen $\mathrm{k_T}$ Faktorisierungsansatz im ‘Color Singlet Model’ (CSM) nutzt, in dem Korrekturen höherer Ordnung berücksichtigt werden. Außerdem werden Vorhersagen von Rechnungen im Rahmen des CSM in führender und nächstführender Ordnung untersucht. Die Polarisationsvariablen werden, zusätzlich zu den CSM Vorhersagen in führender Ordnung, mit Rechnungen im Faktorisierungsansatz der NRQCD verglichen.

Abstract

This thesis presents measurements of inelastic photoproduction and electroproduction of J/Ψ mesons in ep scattering at HERA. The data was collected by the H1 detector during the HERA II running and corresponds to an integrated luminosity of $\mathcal{L} \approx 166\ \mathrm{pb}^{-1}$ in the photoproduction analysis and $\mathcal{L} \approx 315\ \mathrm{pb}^{-1}$ in the electroproduction analysis. In both analyses the elasticity of the J/Ψ meson is restricted to a medium range of $0.3 \leqslant \mathrm{z} \leqslant 0.9$. The kinematic range of the photoproduction analysis is defined by $\mathrm{Q}^2 \approx 0\,\mathrm{GeV}^2$, $60 \leqslant \mathrm{W}_{\gamma p} \leqslant 240\,\mathrm{GeV}$ and $\mathrm{P}_{\mathrm{T},\Psi} \geqslant 1\,\mathrm{GeV}^2$, whereas the electroproduction analysis is restricted to $3.6 \leqslant \mathrm{Q}^2 \leqslant 100\,\mathrm{GeV}^2$, $50 \leqslant \mathrm{W}_{\gamma p} \leqslant 225\,\mathrm{GeV}$, and $\mathrm{P}^*_{\mathrm{T},\Psi} \geqslant 1\,\mathrm{GeV}$. Here $\mathrm{P}^*_{\mathrm{T},\Psi}$ denotes the transverse momentum of the J/Ψ in the $\gamma\mathrm{p}$ center of mass frame.

In both kinematic ranges, single differential and double differential cross sections are measured with increased precision with respect to previous analyses. The polarisation of the J/Ψ mesons is studied in fits to the decay angular distributions $\cos(\Theta^*)$ and ϕ^*.

The measured cross sections are compared to different theoretical predictions. The most successful calculation in describing the data accounts for higher order corrections by using a $\mathrm{k_T}$ factorisation ansatz in the color singlet model (CSM). In addition, this thesis reviews the description of the data by calculations at leading and next to leading order in the CSM. The polarisation variables are compared to calculations in the factorisation ansatz in NRQCD, in addition to the leading order CSM predictions.

Contents

CHAPTER 1

Introduction

The field of high energy physics in the 1950's and 1960's was marked by various discoveries of new particles. Most of these particles (hadrons, resonances) decay by strong interactions and thus have a very short lifetime. The hope of the physicists was to explain this particle zoo within a simple substructure model. In 1963 the 'quark model' was introduced independently by Murray Gell-Mann and George Zweig. In this model the hadrons are identified as combinations of two ($q\bar{q}$, mesons) or three (qqq, baryons) quarks. All known hadrons of that time could be build up by only three quarks, which were called *up*, *down* and *strange* (u,d,s). A big success of the quark model was, that it predicted the existence of new hadrons which were soon discovered, like the Ω^- (sss) meson in 1964. Existing problems of the developing theory were solved by introducing a fourth quark flavour called *charm* (c), predicted in 1970 by Sheldon Lee Glashow, John Iliopoulos and Luciano Maiani. It took however some years to prove the existence of this fourth quark flavour experimentally. The discovery of a new resonance in 1974 became later known as the 'November revolution of particle physics'. Two groups around Samuel C. C. Ting in Brookhaven ('J') and Burton Richter in Stanford ('Ψ') discovered independently the J/Ψ meson at a mass of 3.1 GeV. The J/Ψ meson was identified as being a bound state of a charm and an anticharm quark (charmonium). The importance of this discovery was realized immediately and only two years later Ting and Richter were awarded the Nobel Prize in 1976.

Up to now the J/Ψ meson is an outstanding particle from both the experimental and the theoretical point of view. It can be produced in large numbers in strong interactions, but decays into charmed hadrons can not occur, since its mass is below the threshold of two charmed mesons. This explains the narrow decay width of the J/Ψ meson ($\Gamma_{J/\Psi} \approx 95\,\mathrm{keV}$) and results in an unusually large electromagnetic branching ratio into two muons or electrons of $\mathcal{BR}_{\ell\ell} \approx 12\,\%$. The leptonic decay channels provide a very clean event signature and most kinematic quantities can be calculated from the two precisely measurable lepton tracks.

Nowadays, the theory of strong interactions between quarks and gluons, quantum chromodynamics (QCD), is well understood. In the presence of a hard scale it allows precise predictions in perturbative calculations (pQCD). In particular processes involving heavy quarks can be calculated in pQCD, since the large quark masses provide a hard scale on their own. However, up to now no calculations exist which describe all aspects of J/Ψ meson production properly. The analysis of J/Ψ meson production thus poses an interesting challenge to the theory and the description of perturbative QCD and the non perturbative formation of the bound $c\bar{c}$ state.

At HERA two different production mechanisms for J/Ψ mesons are accessible, the elastic and the inelastic process via boson gluon fusion (BGF). In BGF the incoming lepton is seen as a source of photons interacting with a gluon from the proton via formation of a $q\bar{q}$ pair. In diffraction the photon fluctuates into a $q\bar{q}$ state which subsequently interacts with the proton without the exchange of quantum numbers. Depending on the virtuality Q^2 of the photon, two kinematic regions are distinguished. In *photoproduction* (γp) the beam lepton is scattered under a small angle and the emitted photon is (quasi-)real. The region of *electroproduction* (DIS) starts at virtualities of few GeV^2, where the scattering angle of the beam lepton becomes large enough to be within the acceptance of the main detector.
This thesis presents the results from the analyses of inelastic photoproduction and electroproduction of J/Ψ mesons at the H1 experiment. To study the production process differential and double differential cross sections are measured. To study the helicity structure of the J/Ψ mesons, the polarisation variables α and ν are extracted. In addition, the cross section of Ψ(2S) mesons relative to the J/Ψ cross section is measured in photoproduction. The data are compared with theoretical predictions of the color singlet model (CSM) in leading and next to leading order and to a k_T factorisation approach in this model.
The thesis starts with a discussion of the theoretical frame work of heavy quark and inelastic J/Ψ meson production at HERA. The second chapter explains briefly the HERA accelerator and the relevant components of the H1 experiment. Subsequently the identification of decay leptons (chapter 4) and the analysis triggers (chapter 5) are described. Chapter 6 introduces the cuts which are used for the selection of the event sample. The results of the photoproduction and electroproduction analyses are presented in the chapters 7 and 8. The thesis finishes with a conclusion in chapter 9.

Although the analyses themselves are performed independently, they would not have been possible without the use of the analysis framework, reconstruction algorithms, and calibrations developed and implemented by many H1 collaborators over the last twenty years. In parallel to the analyses my main contribution in the H1 collaboration was the improvement of the read out software of the muon detector in order to activate the third trigger level. In addition I have been on call to support the shift crews in all aspects concerning the muon system and served as librarian for the muon finding software in the object oriented analysis framework H1OO.

CHAPTER 2

Charmonium Production

2.1 Kinematics in ep Scattering

The interaction between electrons and protons at HERA can be described by the exchange of a gauge boson as illustrated in the generic feynman diagram for ep scattering in figure 2.1. Here $\mathbf{k}$ and $\mathbf{P}$ denote the four momentum vector of the incoming lepton and proton respectively, $\mathbf{k}'$ and $\mathbf{P}'$ the four momentum of the scattered lepton and the hadronic finale state X (HFS) accordingly. The negative square of the four momentum transfer $\mathbf{q}$ defines the virtuality Q^2 of the exchanged gauge boson

$$\mathrm{Q}^2 = -\mathbf{q}^2 = -(\mathbf{k} - \mathbf{k}')^2. \tag{2.1}$$

There are neutral current processes (NC) with the exchange of a γ or Z^0 and charged current (CC) processes, where a $\mathrm{W}^\pm$ boson is exchanged. In charged current processes, the beam lepton transforms into a neutrino

$$\text{NC:}\quad \mathrm{e}^\pm\mathrm{p} \rightarrow \mathrm{e}^\pm\mathrm{X} \qquad\qquad \text{CC:}\quad \mathrm{e}^\pm\mathrm{p} \rightarrow \overset{(-)}{\nu}_{\mathrm{e}}\,\mathrm{X}. \tag{2.2}$$

The propagator of the weak interaction via the heavy Z^0 or $\mathrm{W}^\pm$ bosons is suppressed by a factor $\mathrm{Q}^2/(\mathrm{Q}^2 + \mathrm{M}^2_{\mathrm{W,Z}})$ with respect to the electromagnetic interaction via a photon. Due to the high mass of the gauge bosons of the weak interaction

$$\mathrm{M}_{\mathrm{W}^\pm} \approx 80.4\,\mathrm{GeV} \tag{2.3}$$
$$\mathrm{M}_{\mathrm{Z}^0} \approx 91.2\,\mathrm{GeV} \tag{2.4}$$

this process can be neglected in neutral current processes up to virtualities Q^2 of the order of $1000\,\mathrm{GeV}^2$.

At HERA the minimal resolvable distance at the largest possible values of Q^2 is $\delta \approx 10^{-18}\,\mathrm{m}$. This value can be estimated according to the uncertainty relation of Heisenberg ($\delta \cdot |\tilde{\mathrm{q}}| \approx 1$), which leads to $\delta \approx 2\mathrm{m_p x}/\mathrm{Q}^2$.

The photon virtuality Q^2 is used to separate the two kinematic regions of 'quasi' photoproduction (γp) and electroproduction (DIS). In photoproduction the exchanged

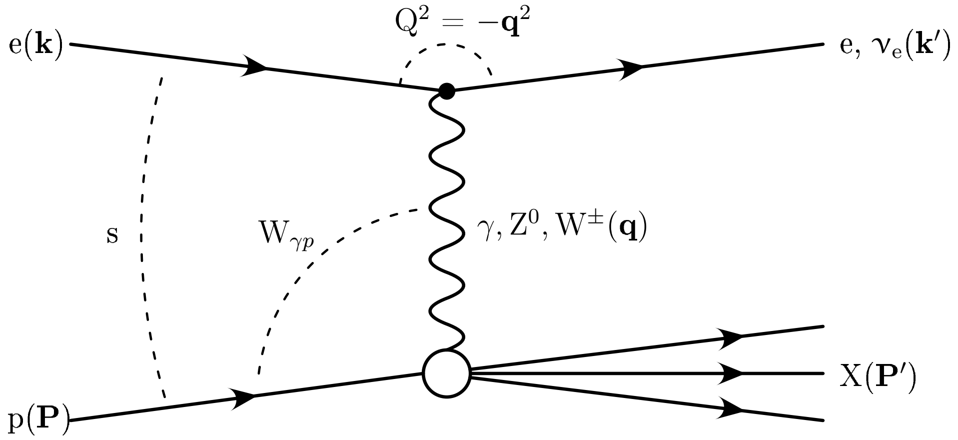

Figure 2.1: Generic feynman diagram for electron proton scattering. The bold letters indicate the four momentum vectors of the particles.

photon is quasi real with vanishing virtuality ($Q^2 \approx 0\,\mathrm{GeV}^2$) and the beam lepton leaves the detector through the beam pipe. Towards larger angles of the lepton, the virtuality of the photon increases. The electroproduction regime ($Q^2 \geqslant 3.6\,\mathrm{GeV}^2$) is defined by the presence of the scattered lepton in the main detector.

Two additional Lorentz invariant variables are defined in addition to the photon virtuality Q^2

$$x = \frac{Q^2}{2 \cdot \mathbf{P} \cdot \mathbf{q}} \qquad \text{and} \tag{2.5}$$

$$y = \frac{\mathbf{P} \cdot \mathbf{q}}{\mathbf{p} \cdot \mathbf{k}}. \tag{2.6}$$

In the QPM, x is interpreted as the fraction of the momentum of the proton which is carried by the struck quark. y denotes the fractional beam lepton energy carried by the (virtual) photon. Since this energy is absorbed in the hadronic final state, y is also called ‘inelasticity’ of the event.
It is common to define two more variables which can be approximated, by neglecting the masses of electron and proton, as

$$s = (\mathbf{k} + \mathbf{P})^2 \approx 4 \cdot E_e E_p \tag{2.7}$$

$$W_{\gamma p}^2 = (\mathbf{q} + \mathbf{P})^2 \approx -Q^2 + s \cdot y, \tag{2.8}$$

where $W_{\gamma p}$ is the center of mass energy in the photon proton rest frame (i.e. the invariant mass of X). The squared ep center of mass energy $s = (318\,\mathrm{GeV})^2$ relates the three kinematic variables Q^2, x and y as

$$Q^2 = s \cdot x \cdot y, \tag{2.9}$$

hence only two out of the three variables are independent at fixed beam energies.

Reconstruction of the Kinematics

At HERA both the scattered electron and the hadronic final state are measured, whereas only two out of these four quantities are necessary to calculate the kinematic variables x, y and Q^2. The kinematics of DIS at HERA are thus overconstrained by the measurements and it is possible to combine these measurements in different methods to reconstruct the kinematics.

Electron Method

In the electron method, all kinematic variables are calculated from the measured quantities of the scattered lepton

$$\mathrm{y_e} = 1 - \frac{\mathrm{E_{e'}}}{\mathrm{E_e}} \cdot \sin^2\left(\frac{\Theta_{\mathrm{e'}}}{2}\right), \tag{2.10}$$

$$\mathrm{Q_e^2} = 4\mathrm{E_e}\mathrm{E_{e'}} \cdot \cos^2\left(\frac{\Theta_{\mathrm{e'}}}{2}\right) \tag{2.11}$$

where $\mathrm{E_e}$ denotes the nominal energy of the lepton beam ($\mathrm{E_e} \approx 27.5\,\mathrm{GeV}$), $\mathrm{E_{e'}}$ the energy of the scattered lepton and $\Theta_{\mathrm{e'}}$ the angle relative to the beam axis. The energy and the angle of the scattered lepton can be measured very precisely. This method is sensitive to initial state photon radiation (ISR), which reduces the actual lepton beam energy.

Jacquet Blondel Method

The Jacquet Blondel method uses only the quantities of the hadronic final state (HFS) to determine the kinematic variables

$$\mathrm{y_{JB}} = \frac{1}{2 \cdot \mathrm{E_e}} \cdot \sum_{HFS} (\mathrm{E} - \mathrm{P_z}), \tag{2.12}$$

$$\mathrm{Q_{JB}^2} = \frac{1}{1 - \mathrm{y_{JB}}} \cdot \sum_{HFS} \mathrm{P_T^2}. \tag{2.13}$$

The sums run over all particles in the hadronic final state (excluding the scattered lepton if present). The method from Jacquet and Blondel is used in photoproduction and charged current analyses.

Σ Method

The Σ method is a modification of the JB method. Instead of the nominal lepton beam energy $\mathrm{E_e}$ a 'measured' lepton beam energy is used. This beam energy $\sum (\mathrm{E} - \mathrm{P_z})/2$ is calculated from the hadronic final state *and* the scattered lepton. The advantage of this method lies in the fact, that the beam energy can be reduced by initial state photon radiation. Without ISR the measured beam energy yields the nominal beam energy due to the conservation of energy and momentum ($\sum (\mathrm{E} - \mathrm{P_z}) \overset{\mathrm{no\ ISR}}{=} 2 \cdot \mathrm{E_e} \approx 55\,\mathrm{GeV}$). The sum over the squared transverse momenta of the particles in the HFS is replaced by the squared transverse momentum of the scattered lepton $p^2_{T,e}$

$$
\begin{aligned}
y_\Sigma &= \frac{\sum\limits_{HFS}(E-P_z)}{\sum(E-P_z)}, & (2.14)\\
Q^2_\Sigma &= \frac{1}{1-y_\Sigma}\cdot p^2_{T,e}. & (2.15)
\end{aligned}
$$

eΣ Method

The eΣ method is a combination of the electron and the Σ method. The four momentum transfer Q^2 is calculated from the scattered lepton only

$$Q^2_{e\Sigma} = 4E_eE_{e'}\cdot\cos^2\left(\frac{\Theta_{e'}}{2}\right), \tag{2.16}$$

while the inelasticity y is calculated according to the Σ method

$$y_{e\Sigma} = \frac{\sum\limits_{HFS}(E-P_z)}{\sum(E-P_z)}. \tag{2.17}$$

At the H1 experiment $\sum(E-P_z)$ is calculated using information from the calorimeters and the trackers. The information from tracks is generally preferred in this sum, and in order to avoid double counting calorimeter cells along the extrapolated track are not taken into account, except for very high energy deposits where the calorimeter is superior to the track measurement.
In the photoproduction part of this analysis, the Jacquet Blondel method is used for the calculation of the kinematics, while the eΣ method is used for the electroproduction sample.

In order to describe the kinematics of more exclusive measurements, more variables are necessary to model the kinematics of the process. In the analysis of J/Ψ mesons, the Lorentz invariant elasticity z is essential

$$z = \frac{\mathbf{P}_{J/\Psi}\cdot\mathbf{P}}{\mathbf{q}\cdot\mathbf{P}} = \frac{y_{J/\Psi}}{y} = \frac{\sum\limits_{J/\Psi}E-P_z}{\sum\limits_{HFS}E-P_z}. \tag{2.18}$$

In the proton rest frame, the elasticity z denotes the fractional energy of the virtual photon transferred to the J/Ψ meson $z = E_{J/\Psi}/E_{\gamma}*$. The elasticity z is a powerful observable as it allows to discriminate between inelastic and elastic production of J/Ψ mesons. As explained in section 2.8, the elastic processes are located at $z \lesssim 1$. The inelastic process takes place over the whole elasticity range with vanishing phase space towards very large elasticities.

2.2 Inclusive Cross Section

The differential neutral current cross section can be written as a function of x and Q^2 as

$$\frac{d^2\sigma_{ep}}{dxdQ^2} = \frac{4\pi\alpha^2}{xQ^4} \cdot \left[y^2 x \cdot F_1\left(x, Q^2\right) + (1-y) \cdot F_2\left(x, Q^2\right)\right], \tag{2.19}$$

where α denotes the electromagnetic coupling constant and $F_1(x, Q^2)$ and $F_2(x, Q^2)$ are structure functions. The parity violating contribution from the structure function F_3 is neglected in equation 2.19.

Introducing the structure function $F_L\left(x, Q^2\right) = F_2 - 2xF_1$, which is related to longitudinally polarised photons, equation 2.19 transforms to

$$\frac{d^2\sigma_{ep}}{dxdQ^2} = \frac{2\pi\alpha^2}{xQ^4} \cdot \left[\left(1 + (1-y)^2\right) \cdot F_2\left(x, Q^2\right) - y^2 \cdot F_L\left(x, Q^2\right)\right]. \tag{2.20}$$

The longitudinal structure function F_L is kinematically suppressed with respect to F_2, except for the kinematic region at high inelasticities y and high virtualities Q^2. In the limit of vanishing photon virtuality, all photons are transversely polarised. The leading order cross sections without radiative corrections in the equations 2.19 and 2.20 are called ‘Born cross section’.

For historical reasons, the measured ep cross sections in the photoproduction part of this analysis are transformed into γp cross sections. In the Weizsäcker Williams approximation (WWA, [BGMS74]), the incoming electron is seen as a source of photons. At small $x \ll 10^{-2}$, where the interaction time with the proton is much smaller compared to the lifetime of the virtual photon [Lev95], the process $e^{\pm}p \rightarrow e^{\pm}X$ can be factorised into the emission of a photon from the electron and the subsequent interaction of this photon with the proton. Splitting the photon flux Φ_γ into a longitudinal Φ_γ^L and a transverse Φ_γ^T (depending on the polarisation of the photons), the Born cross section can be expressed as

$$\frac{d\sigma_{ep}^2}{dydQ^2} = \Phi_\gamma^T(y, Q^2) \cdot \sigma_{\gamma p}^T(y, Q^2) + \Phi_\gamma^L(y, Q^2) \cdot \sigma_{\gamma p}^L(y, Q^2), \tag{2.21}$$

where $\sigma_{\gamma p}^T$ and $\sigma_{\gamma p}^L$ denote the cross sections for transversely or longitudinally polarised photons respectively. The flux of transversely polarised photons Φ_γ^T in the WWA is given by

$$\Phi_\gamma^T = \frac{\alpha}{\pi y Q^2} \cdot \left(1 - y + \frac{1}{2}y^2\right) \tag{2.22}$$

and the ratio of the two fluxes defines the polarisation factor ϵ

$$\epsilon(y) = \frac{\Phi_\gamma^L}{\Phi_\gamma^T} = \frac{1-y}{1-y+\frac{1}{2}y^2} \tag{2.23}$$

Using the polarisation factor, equation 2.21 can be transformed to

$$\frac{\mathrm{d}^2\sigma_{\mathrm{ep}}}{\mathrm{dxdQ}^2} = \Phi_\gamma^{\mathrm{T}} \cdot \underbrace{\left(\sigma_{\gamma\mathrm{p}}^T + \epsilon\sigma_{\gamma\mathrm{p}}^L\right)}_{\sigma_{\gamma\mathrm{p}}} = \Phi_\gamma^{\mathrm{T}} \cdot \sigma_{\gamma\mathrm{p}} \cdot \frac{1+\epsilon\mathcal{R}}{1+\mathcal{R}}, \tag{2.24}$$

where $\mathcal{R} = \sigma_{\gamma\mathrm{p}}^{\mathrm{L}}/\sigma_{\gamma\mathrm{p}}^{\mathrm{T}}$ denotes the ratio of the cross sections for longitudinal and for transverse polarisation. In the limit of small y, the polarisation factor ϵ is close to one ($\overline{\epsilon} \approx 0.99$) and the Born cross section is well approximated by

$$\frac{\mathrm{d}^2\sigma_{\mathrm{e}^\pm\mathrm{p}}}{\mathrm{dydQ}^2} \approx \Phi_\gamma^{\mathrm{T}}\sigma_{\gamma\mathrm{p}} \tag{2.25}$$

or, after integrating equation (2.25) over y and Q^2, as

$$\sigma_{\mathrm{e}^\pm\mathrm{p}} = \int\limits_{\mathrm{y_{min}}}^{\mathrm{y_{max}}} \mathrm{dy} \int\limits_{\mathrm{Q^2_{min}}}^{\mathrm{Q^2_{max}}} \mathrm{dQ}^2 \; \Phi_\gamma^{\mathrm{T}}\left(\mathrm{y},\mathrm{Q}^2\right) \cdot \sigma_{\gamma\mathrm{p}}\left(\mathrm{W}_{\gamma p}(\mathrm{y}),\mathrm{Q}^2\right) \tag{2.26}$$

where the limits for the four momentum transfer are given by the kinematic minimum $\mathrm{Q}^2_{\mathrm{min}} = \mathrm{m}_{\mathrm{e}}^2 \cdot \mathrm{y}^2(1-\mathrm{y})^{-1}$ and the upper Q^2 boundary of the photoproduction analysis $\mathrm{Q}^2_{\mathrm{max}} = 2\,\mathrm{GeV}^2$.

Since the cross section $\sigma_{\gamma\mathrm{p}}$ is completely independent from the photon flux Φ_γ^{T}, both can be integrated independently, leading to

$$\begin{aligned}\sigma_{\mathrm{e}^\pm\mathrm{p}} &= \sigma_{\gamma\mathrm{p}}\left(\langle\mathrm{W}_{\gamma p}\rangle\right) \cdot \int\limits_{\mathrm{y_{min}}}^{\mathrm{y_{max}}} \mathrm{dy} \int\limits_{\mathrm{Q^2_{min}}}^{\mathrm{Q^2_{max}}} \mathrm{dQ}^2 \; \Phi_\gamma^{\mathrm{T}}\left(\mathrm{y},\mathrm{Q}^2\right) &(2.27)\\ &= \sigma_{\gamma\mathrm{p}}\left(\langle\mathrm{W}_{\gamma p}\rangle\right) \cdot \Phi_\gamma, &(2.28)\end{aligned}$$

where Φ_γ denotes the integrated photon flux and $\sigma_{\gamma\mathrm{p}}\left(\langle\mathrm{W}_{\gamma p}\rangle\right)$ corresponds to the γp cross section at a certain mean energy of the photon proton system $\langle\mathrm{W}_{\gamma p}\rangle$. Using the integrated photon flux Φ_γ the γp cross section can be derived from the ep cross section via the relation

$$\sigma\left(\gamma\mathrm{p} \rightarrow \mathrm{J}/\Psi\ \mathrm{X}\right) = \frac{1}{\Phi_\gamma} \cdot \sigma\left(\mathrm{e}^\pm\mathrm{p} \rightarrow \mathrm{J}/\Psi\ \mathrm{X}\right). \tag{2.29}$$

In the kinematic range of this analysis the integrated photon flux Φ_γ for photoproduction was determined to be $\Phi_\gamma \approx 0.1012$. For the cross section as a function of $\mathrm{W}_{\gamma p}$, the photon flux factor has to be calculated for each cross section bin of the analysis and the differential ep cross section $\mathrm{d}\sigma(\mathrm{e}^\pm\mathrm{p} \rightarrow \mathrm{J}/\Psi\ \mathrm{X}/\mathrm{dW}_{\gamma p})$ transforms into a total γp cross section $\sigma(\gamma\mathrm{p} \rightarrow \mathrm{J}/\Psi\ \mathrm{X})(\mathrm{W}_{\gamma p})$ in bins of $\mathrm{W}_{\gamma p}$.
The factors for the bins in this analysis are listed in table 2.1.

$W_{\gamma p}$ [GeV]	$\langle W_{\gamma p}\rangle$ [GeV]	Φ_γ
60 – 240	116.12	0.1012
60 – 80	69.31	0.0267
80 – 100	89.44	0.0190
100 – 120	109.51	0.0143
120 – 140	129.56	0.0111
140 – 160	149.59	0.0088
160 – 180	169.62	0.0071
180 – 210	194.19	0.0082
210 – 240	224.24	0.0061

Table 2.1: Photon flux factors Φ_γ for the photoproduction analysis using an upper Q^2 boundary of $Q^2 \approx 2\,\mathrm{GeV}^2$. The first line corresponds to the integrated flux for the analysis range $60 \leqslant W_{\gamma p} \leqslant 240$, below the flux in the used analysis $W_{\gamma p}$ bins is given.

2.3 Factorisation and Parton Evolution

In the quark parton model (QPM), introduced by Richard P. Feynman in 1969 [Fey69], the proton consists of three point like partons with spin 1/2. Later James Bjorken and Emmanuel Paschos [BP69] identified these partons with the quarks, which were postulated by Murray Gell-Mann and George Zweig before [GM64, Zwe64a]. Deep inelastic scattering of electrons with protons at large Q^2 is viewed as an elastic interaction between the electron and a single free parton. Without interactions between the partons the structure function F_2 is expected to be scale invariant, i.e. it should be independent of Q^2 and only depend on the fraction of proton momentum carried by the struck quark [Bjo69]

$$F_2(x) = x \cdot \sum_i e_i^2 \cdot f_i(x). \tag{2.30}$$

Here the sum is built over all partons i, e_i denotes the (electrical) charge of the parton and $f_i(x)$ corresponds to the probability to find a parton with a certain momentum fraction x.

First measurements at $x \approx 0.25$ confirmed the assumption of scale invariance, because the scaling violation is very small in this kinematic range [FK72]. In the middle of the 70's first scaling violations were observed in μN [F$^+$74] and νN [dG$^+$79] scattering. Today, HERA measurements, in a much larger x range and at larger values of Q^2, prove the scaling violation of F_2 impressively (cf. figure 2.2). Towards low momentum fractions x the structure function F_2 rises strongly as a function of Q^2, while it falls off at large values of x.

Few years after the QPM, a new theory of strong interactions, the quantum chromodynamics (QCD), was introduced by Murray Gell-Mann with the aid of Harald

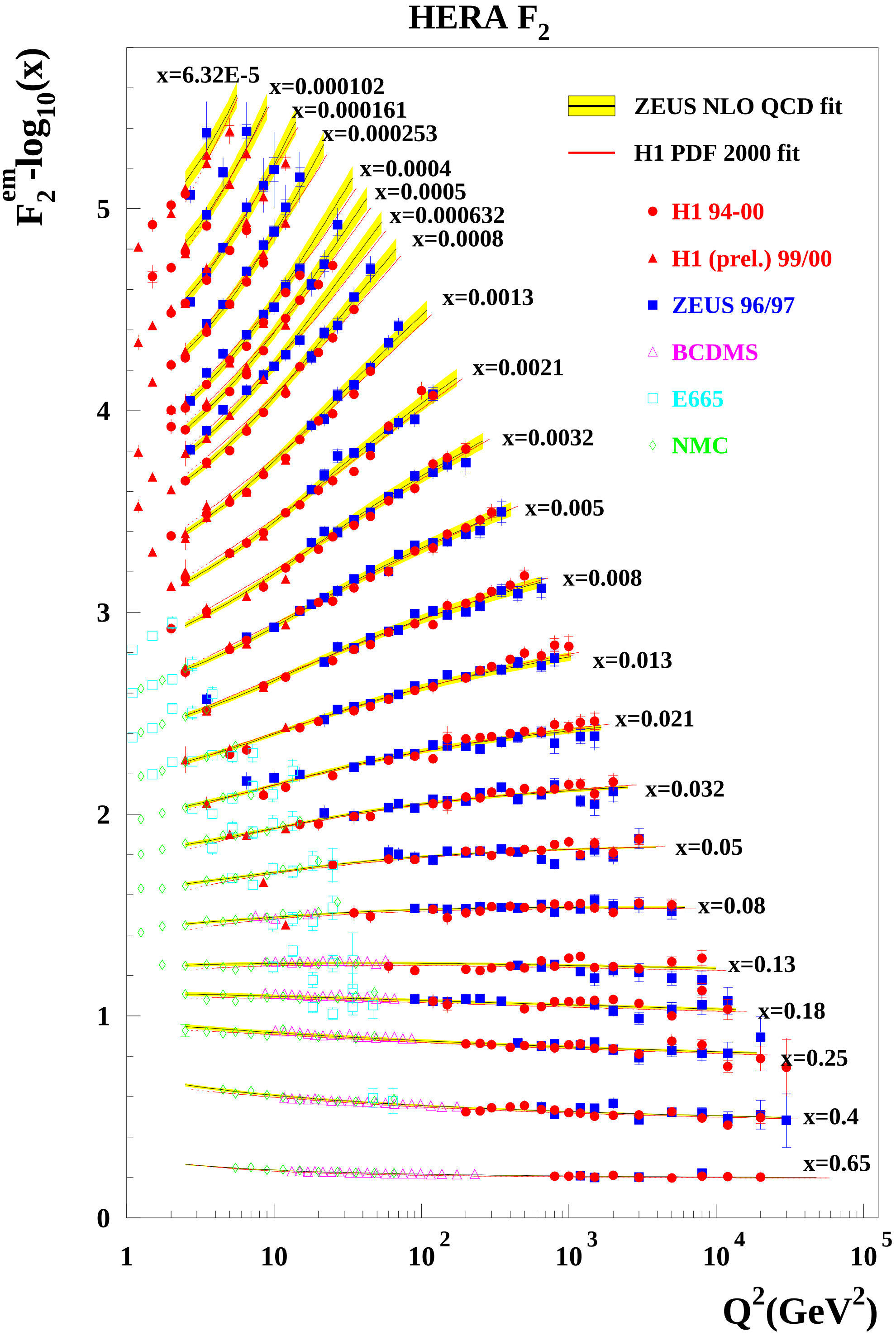

Figure 2.2: Structure function F_2 as measured in fixed target experiments and at HERA.

Fritzsch and Heinrich Leutwyler [FGML73]. In QCD a new quantum number, the color charge (red, green or blue), is assigned to all quarks. Accordingly, antiquarks are 'anti'-red, 'anti'-green or 'anti'-blue.

Due to the non abelian SU(3) nature of QCD, the gauge bosons of the strong interaction, i.e. the gluons, carry color charges and couple to each other. The color charge of gluons is made of a color and an anti-color.

The self coupling of the gluons in the QCD introduces gluon radiation from gluons ($g \rightarrow gg$), in addition to gluon splitting into a quark antiquark pair ($g \rightarrow q\bar{q}$) and gluon radiation from a quark ($q \rightarrow qg$). These processes lead to the steeply rising amount of quark pairs in the proton towards low values of x, which explains the observed scaling violation of F_2.

The calculation of these processes is difficult in pQCD, because the gluon radiation and gluon splitting are connected to divergent integrals. Parts of the divergences are moved into parton distribution functions $f_i(x, \mu_f^2)$ (PDF) by introducing a cut off at the 'factorisation scale' μ_f. Reliable calculations in perturbative QCD (pQCD) can only be achieved for large values of the factorisation scale ($\mu_f \gg \Lambda_{QCD} \approx 200\,\mathrm{MeV}$). The remaining ultra violet divergences are absorbed in the running coupling α_s (μ_r), which then depends on the 'renormalisation scale' (μ_r). The strong coupling diverges in the limit $\mu_r \rightarrow \Lambda_{QCD}$.

Due to the gluon self interaction, the running of the renormalised coupling is contrary to that of the electromagnetic coupling constant. At small distances (large Q^2) α_s is small, towards larger distances (lower Q^2) α_s increases. This leads to the two phenomenons 'asymptotic freedom' and 'confinement'. Asymptotic freedom means, that at high energies, i.e. at small distances, the quarks act as if they were free particles. Confinement means that particles with color charge are confined to color neutral hadrons, hence no free quarks or gluons can be observed.

The cross section factorises into a cross section for the hard subprocess $\hat{\sigma}_i$ which is calculable in perturbation theory and the parton distribution function $f_i(x, \mu_f^2)$

$$d\sigma(e^{\pm}p \rightarrow eX) = \sum_i \int_0^1 dx \cdot f_i(x, \mu_f^2) \cdot d\hat{\sigma}_i(\hat{s}, \alpha_s(\mu_r^2), \mu_r, \mu_f). \qquad (2.31)$$

$\hat{\sigma}_i$ can be calculated in perturbation theory, depending on the center of mass energy in the partonic system after the evolution $\sqrt{\hat{s}}$, the strong coupling being α_s, the factorisation scale being μ_f and the renormalisation scale being μ_r.

A common factorisation scale is $\mu_f = Q^2$. For $f_i(x, \mu_f^2) > 0$, the parton distribution function $f_i(x, \mu_f^2)$ gives the probability that a quark or gluon with momentum fraction x enters the hard scattering at a certain Q^2. The $f_i(x, \mu_f^2)$ is expected to be universal and independent of the hard subprocess. This means that a $f_i(x, \mu_f^2)$ determined in an inclusive measurement at HERA can be used in order to predict exclusive processes and to calculate predictions for other proton colliders like the LHC.

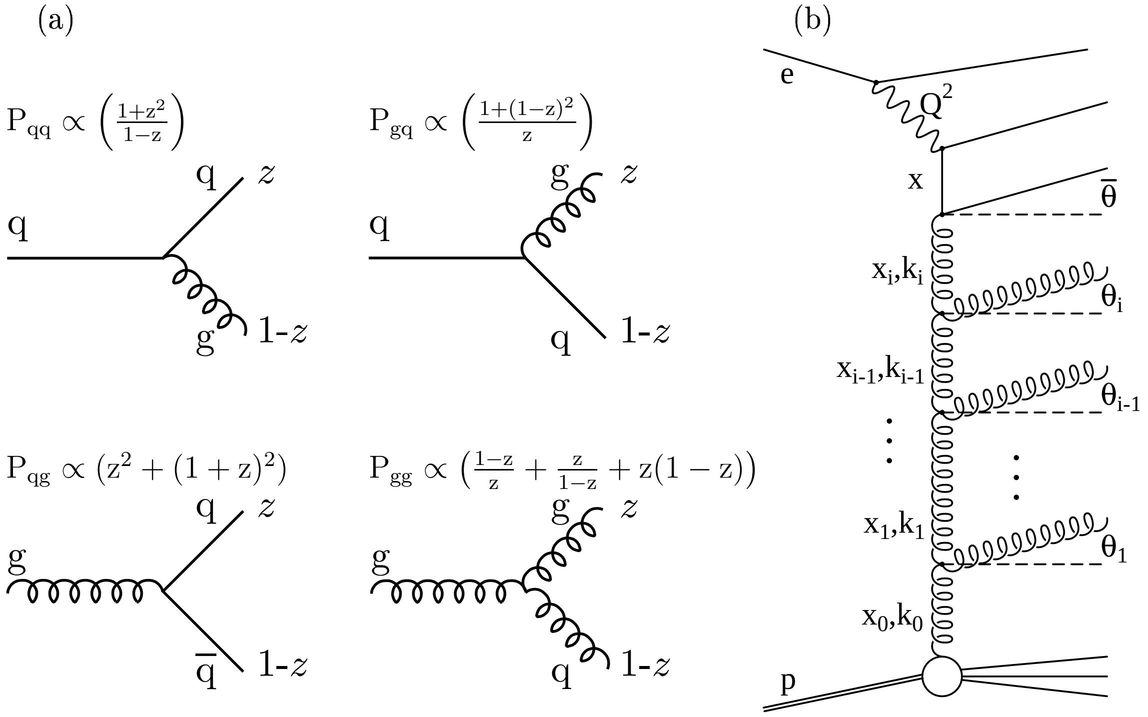

Figure 2.3: (a) Feynman diagrams and splitting functions considered in the evolution equations. (b) an exemplary parton ladder (only gluon radiation) which is calculated during the parton evolution.

The validity of the factorisation is not yet proven generally, but only for deep inelastic scattering (DIS) in the 'Bjorken limit' (increasing Q^2 for a constant value of x) [CS87] and a few other processes. The separation of hard and soft (i.e. non perturbative) processes is not unambiguous, but depends on the choice of the factorisation scheme. The calculation of the hard subprocess has to be adapted to the used scheme.

Different parton evolution equations have been developed in order to predict $f_i(x, \mu_f^2)$ at any scale μ_f, if the PDF is known at a starting scale μ_0 ($f_i(x, \mu_0^2)$). PDFs are obtained experimentally by fitting the structure function to the data at a given starting scale μ_0, so that after the evolution the structure function is able to describe the data at HERA and fixed target experiments at any scale $\mu_f = Q^2$.

The evolution equations consider four archetypes of parton splitting at leading order, which are shown in figure 2.3(a). A quark can split into a quark and a gluon or a gluon can split into a $q\bar{q}$ pair or into two gluons. These processes are parametrised in the splitting functions $P_{ij}(x)$ which give the probability, that the parton j emits a new parton i with the momentum fraction $z = x_i/x_{i-1}$. The analysis of J/Ψ mesons takes place at rather small values of x ($10^{-2}-10^{-4}$), where gluons and gluon splitting

dominate the proton. In the evolution equations several splittings are summed up, leading to a so called 'parton ladder' (cf. fig. 2.3(b)).
The different approaches for the parton evolution equations imply a different ordering of the radiated gluons and require different parton distribution functions as input. The partons can be either arranged according to their longitudinal momentum x_i (BFKL), to their transverse momentum $k_{T,i}$ (DGLAP) or to their pseudo rapidity η_i (i.e. their angle Θ_i) (CCFM). In the following the evolution equations DGLAP and CCFM, which are used in the Monte Carlo generators of this analysis, will be briefly introduced. The BFKL[1] evolution equation is described in [KLF77, BL78].

DGLAP

The DGLAP equations are the most widely used evolution equations, they were published in the 70's independently by Yuri **D**okshitzer, Vladimir **G**ribov and Lev **L**ipatov in the Soviet Union and by Guido **A**ltarelli and Giorgio **P**arisi in Italy [GL72, Lip75, AP77, Dok77].

At large values of Q^2, the leading contribution in the DGLAP equations are strongly ordered by their transverse momentum ($k_{T,i+1} \gg k_{T,i}$) and the transverse momentum of each parton is negligible compared to its longitudinal momentum x_i ('collinear approach').

The virtuality k_i^2 of the parton can be neglected compared to the factorisation scale μ_f and the virtuality of the subsequent parton k_{i+1}^2 and the calculation of the splitting functions and the hard subprocess can be done 'on shell'. The k_T dependence is integrated out of the parton distribution function $f_i(x, \mu_f^2)$ and the calculation starts without initial k_T.

At too small values of x the approximation of collinear factorisation does not hold and the DGLAP equations become invalid.

CCFM

In the early 90's another evolution equation was published by Stefano **C**atani, Marcello **C**iafaloni, Fausto **F**iorani and Guiseppe **M**archesini [Cia88, CFM90a, CFM90b, Mar95]. CCFM interpolates between DGLAP, which is valid at large values of x and BFKL, which is only appropriate at small values of x. During the evolution in CCFM, only gluons are taken into account. The order of the gluons in CCFM follows the angles Θ_i of the emitted gluon ($\Theta_i > \Theta_{i-1}$). In the limit of small angles and rather large x, the momentum fraction $z_i = x_i/x_{i-1}$ becomes $z_i \approx 1$ and the k_T ordering of the DGLAP evolution is recovered. While at small values of x, the CCFM evolution equations approximate the BFKL ordering according to the longitudinal momenta of the gluons. The CCFM evolution is based on a k_T unintegrated parton distribution function $\mathcal{A}_i(x_g, {k_T}^2, \mu_f^2)$, which also depends on k_T. The initial parton is allowed to be off shell ($k_T \neq 0$), the factorisation of the cross section still holds, but it has to take the k_T dependence into account (k_T factorisation).

---

[1] Balitskii-Fadin-Kuraev-Lipatov

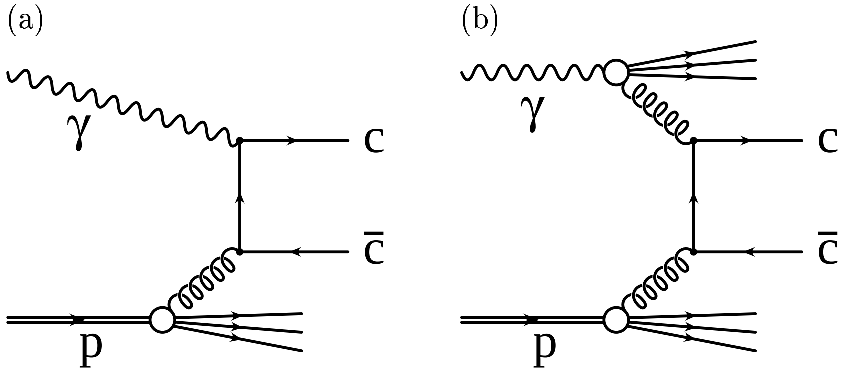

Figure 2.4: Production of a $c\bar{c}$ pair via (a) direct photon gluon fusion and (b) in gluon gluon fusion in a process with a resolved photon.

2.4 Heavy Quark Production

The dominant production process for heavy quark pairs at HERA is the boson gluon fusion (BGF). The generic feynman diagrams for BGF with a direct and a resolved photon are shown in figure 2.4. A gluon is emitted from the proton with a momentum fraction $\mathrm{x_g}$ and fuses with either a photon or gluon. The production of b quarks is suppressed by two orders of magnitude with respect to charm production, due to the larger mass of the b quark and the lower charge ($|\mathrm{q_c}| = 2/3, |\mathrm{q_b}| = 1/3$).
In direct BGF, the photon enters the hard subprocess with its full energy, whereby the production of heavy quark pairs starts already at rather low photon proton center of mass energies $\mathrm{W}_{\gamma p}$. In the case of resolved BGF, the photon fluctuates into a hadronic state and enters the hard subprocess with a gluon, which carrys a momentum fraction x_γ of the virtual photon, hence processes with resolved photons need to have larger $\mathrm{W}_{\gamma p}$ in order to produce a heavy quark pair.[2]

The production of heavy quarks can be used to study QCD processes. If an available scale is large enough, the running coupling α_s is small enough that perturbative expansions can be applied. For heavy quark pairs the large masses

$$\mathrm{m_c} \approx 1.5\,\mathrm{GeV} \tag{2.32}$$

$$\mathrm{m_b} \approx 4.75\,\mathrm{GeV} \tag{2.33}$$

provide a hard scale over the whole phase space on their own. The pQCD predictions should be able to describe the data down to lowest Q^2 (photoproduction) and to low transverse momenta. Unfortunately, this also yields problems at large values of Q^2 and $\mathrm{P_T}$, because the expansion is no longer straight forward, if different scales are present ('multi scale problem') [Beh05].

---

[2] In fact, the resolved photon could also enter the hard scattering with a quark ('charm excitation'), however excitation processes are neglected in this analysis since they cannot form a J/Ψ meson.

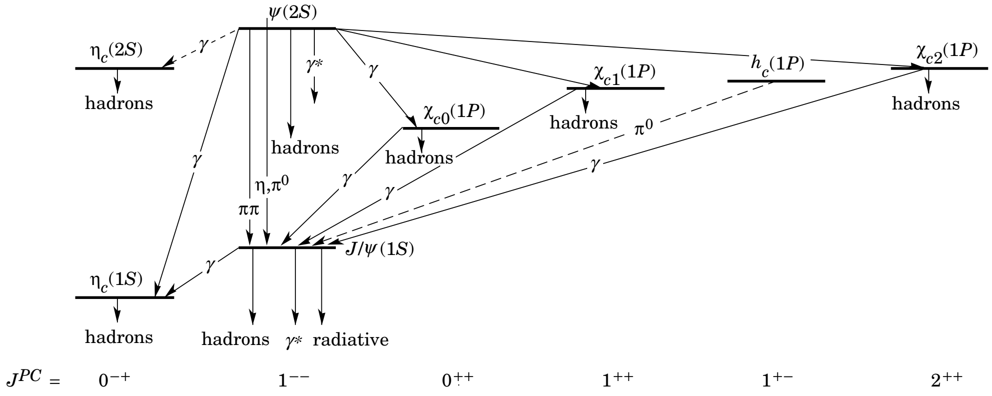

Figure 2.5: Members of the charmonium family and their transitions [PDG08].

The boson gluon fusion process is calculated in the 'fixed flavour numbering scheme' (FFNS), assuming that the heavy quarks are only produced in the hard scattering. This assumption is justified, because the fraction of heavy quarks in the proton is suppressed by a factor $1/m_q$. Therefore the charm content of the proton amounts to ~1 % in total, contributing mainly at $x > 0.3$ and $Q^2 > 100\,\mathrm{GeV}^2$ [BHPS80]. The FFNS is a massive calculation (i.e. the quark masses are taken into account), which allows to model the behaviour at the threshold of the charm quark mass correctly. At large values of Q^2, above the kinematic range of this analysis, logarithmic terms of Q^2 ($\ln(Q^2/m_c^2)$) disturb the convergence of the calculation.

2.5 Charmonium

Bound states of a quark and an antiquark of the same type are called 'quarkonia'. This analysis concentrates on quarkonia which consist of a $c\bar{c}$ pair ('charmonium'). The most prominent member of the charmonium family is the J/Ψ meson, the lightest vector meson in the charmonium system (cf. fig. 2.5). It was discovered in 1974 by two independent groups around Samuel C. C. Ting at AGS in Brookhaven ('J', [A+74a]) and Burton Richter at SPEAR in Stanford ('Ψ', [A+74b]). The first published mass plots of both experiments are shown in figure 2.6. The discovery of the J/Ψ meson proved the existence of the charm quark, which was predicted by Sheldon Lee Glashow, John Iliopoulos and Luciano Mainai some years before [GIM70]. The noble prize for Ting and Richter in 1976 emphasises the importance of this discovery which is often called 'November revolution of particle physics'.

The world average of the mass of the J/Ψ meson is $m_{J/\Psi} = 3096.916 \pm 0.011\,\mathrm{GeV}$ [PDG08]. Its quantum numbers, $J^{PC} = 1^{--}$, are the same as those of the photon. The conservation of energy forbids the strong decay of the J/Ψ meson into two charmed D mesons ($m_{D^0} \approx 1.86\,\mathrm{GeV} > M_{J/\Psi}/2$). The decay via one or two gluons

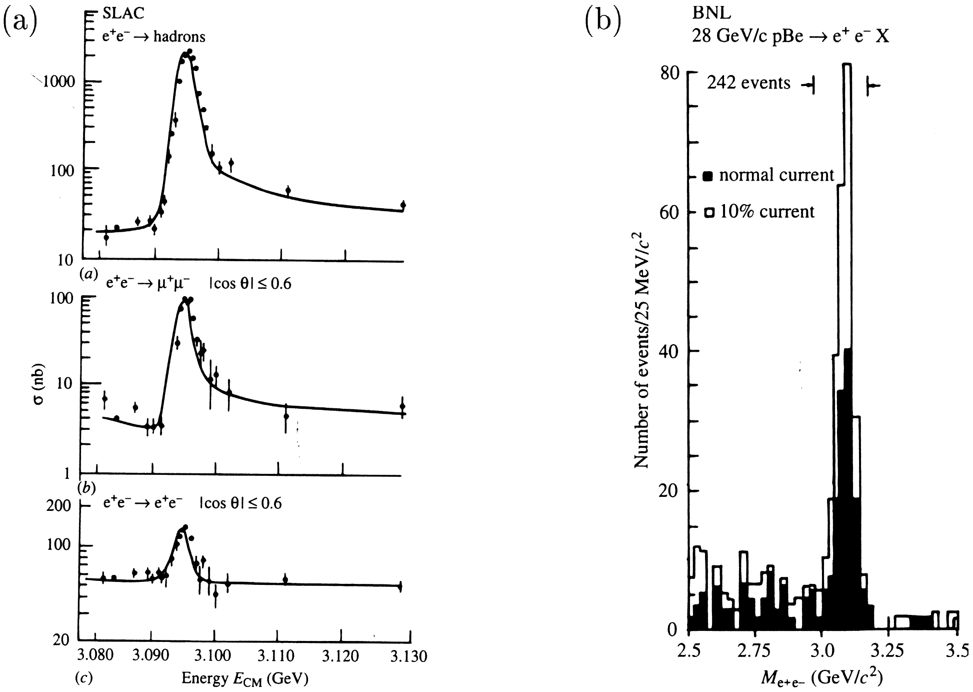

Figure 2.6: Mass plots of the J/Ψ meson, published by groups around (a) Burton Richter (SPEAR) and (b) Samuel Ting (AGS).

is forbidden by color and C parity conservation. The only possible hadronic decay occurs via three gluons, but this decay channel where the initial quarks are not present in the final state is strongly suppressed by the Zweig rule [Zwe64b]. Hence the J/Ψ meson has an extremely narrow decay width of

$$\Gamma_{\mathrm{J}/\Psi} = 93.2 \pm 2.1\,\mathrm{keV} \tag{2.34}$$

and correspondingly a relatively long lifetime around 10^{-20} s, which is three orders of magnitude above typical values for hadrons with a similar mass. The decay width is roughly three orders of magnitude less than expected for hadrons at this mass, and allows a very large electromagnetic branching ratio into two leptons of

$$\mathcal{BR}_{\mathrm{J}/\Psi\to\mu\mu} = 5.93 \pm 0.06\,\% \tag{2.35}$$

$$\mathcal{BR}_{\mathrm{J}/\Psi\to\mathrm{ee}} = 5.94 \pm 0.06\,\%. \tag{2.36}$$

The Ψ(2S) meson is the first radial excitation of the J/Ψ meson. Its mass

$$\mathrm{m}_{\Psi(2\mathrm{S})} = 3.6861 \pm 0.034\,\mathrm{GeV} \tag{2.37}$$

is still below the threshold of two charmed mesons, hence its decay width is also very small ($\Gamma_{\Psi(2\mathrm{S})} = 284 \pm 21\,\mathrm{keV}$). A large fraction of the decay channels of the Ψ(2S) meson involves J/Ψ mesons ($\Psi(2\mathrm{S}) \to \mathrm{J}/\Psi + \mathrm{X}$), while the leptonic decay width is about one eighth of that of the J/Ψ mesons

$$\mathcal{BR}_{\Psi(2S)\to J/\Psi X} = 57.4 \pm 0.9\,\% \tag{2.38}$$
$$\mathcal{BR}_{\Psi(2S)\to \mu\mu} = 0.75 \pm 0.08\,\% \tag{2.39}$$
$$\mathcal{BR}_{\Psi(2S)\to ee} = 0.752 \pm 0.017\,\%. \tag{2.40}$$

So, in the measurement of direct J/Ψ production, sizeable contributions from the decay of Ψ(2S) mesons are expected.
Charmonium states above the Ψ(2S) (not shown in figure 2.5) can decay into D mesons, leading to a much larger decay width.

2.6 Models for Inelastic J/Ψ Meson Production

Two different J/Ψ production processes have to be separated at HERA, namely the inelastic and the diffractive production of J/Ψ mesons. In the case of diffractive production (cf. section 2.8), only the J/Ψ meson is produced. The inelastic production involves the radiation of gluons during the production process, which leads to a hadronic final state in addition to the J/Ψ meson.

Many models in perturbative QCD have been published in order to describe the inelastic production of charmonia. Up to now the production of heavy quarkonia in the context of QCD is an ambitious task and it remains difficult to relate the properties of the multi scale system at high energies with the non perturbative effects at low energies. The analysis of J/Ψ mesons helps to understand the necessary relations between various summation approaches and to study the interplay between perturbative and non perturbative effects.

In the following two models, assuming a factorisation into a hard scattering process (building the $c\bar{c}$ pair) and a long distance transition into a physical J/Ψ, will be briefly introduced, the color singlet model and factorisation ansatz in NRQCD. A detailed report on heavy quarkonia can be found in [QWG04].

Color Singlet Model (CSM)

The color singlet model (CSM) was the first model, which provided quantitative predictions for the production of inelastic J/Ψ mesons in hadron collisions, photoproduction and e^+e^- collisions. It was developed in the early 1980s, with strong contributions from Cha-Hsi Chang [Cha80], Edmond Berger [BJ81] and Rudolf Baier [BR81]. An overview of the application of the CSM was written by Gerhard Schuler [Sch94].

The CSM considers only $c\bar{c}$ pairs which are produced in a color singlet state with the same quantum numbers (i.e. spin, angular momentum and C parity) as the resulting

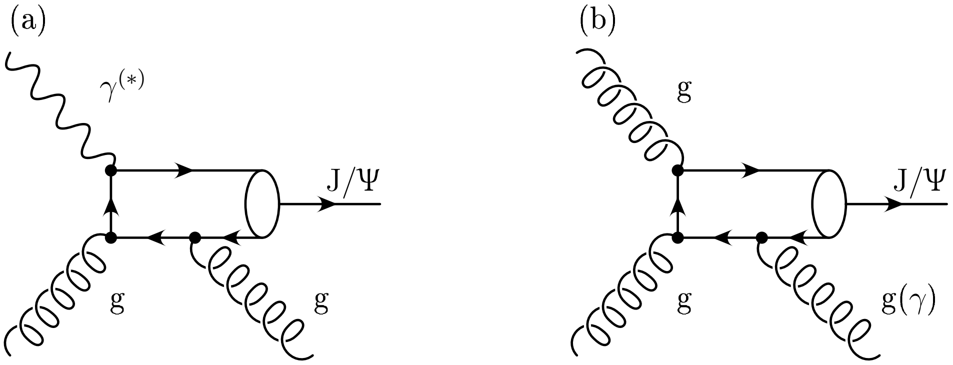

Figure 2.7: Feynman illustrating the color singlet model in leading order in (a) photon gluon fusion (direct) and (b) gluon gluon fusion (resolved, hadroproduction).

charmonium state. The relative momentum of the $c\bar{c}$ pair in the $c\bar{c}$ rest frame must be small with respect to the charm quark mass in order to achieve a noticeable probability for the binding of the quark pair. The generic feynman diagrams for the production of J/Ψ mesons in the CSM are illustrated in figure 2.7. Figure 2.7(a) shows the direct photon gluon fusion ($\mathcal{O}(\alpha, \alpha_s^2)$) in which the photon itself takes part in the hard scattering process, figure 2.7(b) shows the production via gluon gluon fusion ($\mathcal{O}(\alpha_s^3)$). Gluon gluon fusion occurs in processes with a resolved photon[3] at HERA and in collisions at hadron colliders (e.g. TEVATRON, LHC).

In order to achieve a color neutral final state, at least one gluon has to be emitted in the case of direct photon gluon fusion. In the case of gluon gluon fusion the $c\bar{c}$ pair can be produced in a color neutral state, nevertheless a gluon or a photon has to be radiated in order to conserve the angular momentum and the parity of the J/Ψ meson.

The CSM assumes that the cross section factorises into a short distance part $d\hat{\sigma}$ in which the $c\bar{c}$ pair is produced and a long distance part which describes the transition to a bound state

$$d\sigma\left(\gamma + p \rightarrow J/\Psi + X\right) \propto d\hat{\sigma}\left(c\bar{c}\left[\underline{1}, {}^3S_1\right] + X\right) \times \left|R_{J/\Psi}(0)\right|^2, \qquad (2.41)$$

where $\underline{1}$ indicates, that the $c\bar{c}$ is produced in a color singlet state (in contrast to the color octet states $\underline{8}$). ${}^3S_1$ denotes the spectroscopic notation of spin, orbital angular momentum and total angular momentum. The short distance part contains all internal lines which are off shell by $\mathcal{O}(m_c)$ and can be calculated using perturbation theory in $\alpha_s(2m_c)$. To make sure that a perturbative expansion is applicable for the scattering process, the additionally emitted gluon has to be 'hard'. This restricts reliable predictions in the CSM to an elasticity range below $z \approx 0.9$.

The coupling of the charmonium to the $c\bar{c}$ pair in the long distance part depends only on one single non perturbative parameter, hence the predictive power of the

---

[3] In processes with 'resolved photons' the photon fluctuates into a hadronic state, before it takes part in the hard scattering process.

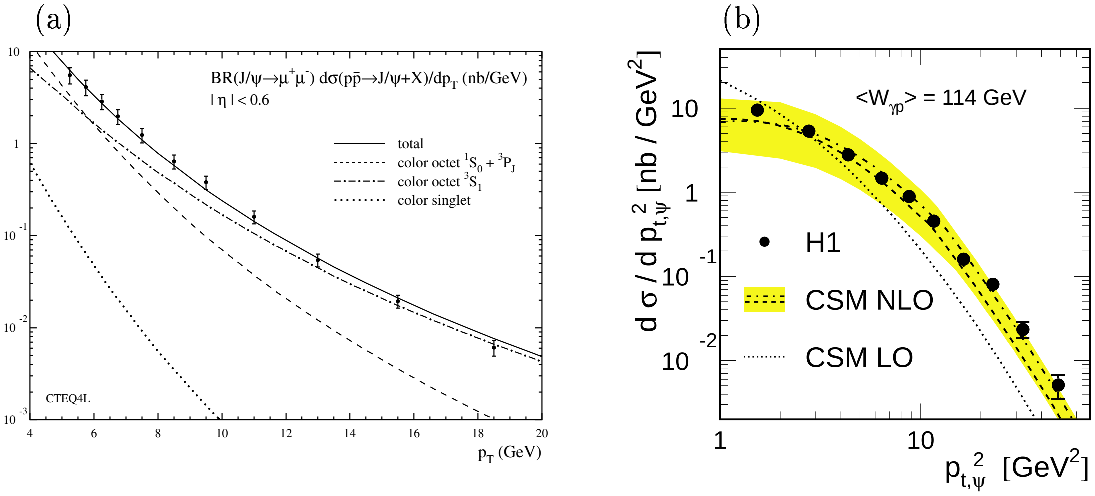

Figure 2.8: Cross section as a function of the (squared) transverse momentum of the J/Ψ meson as measured from (a) the CDF experiment and (b) HERA.

CSM is very good. In case of the s-wave states (Ψ and η) this is the wave function at the origin $|R_\Psi(0)|$, for the p-wave states ($\chi_{c0}, \chi_{c1}, \chi_{c2}, h_c$) it is the first derivative of this wave function $|R'_\chi(0)|$. Furthermore, this parameter can be calculated from the measurable leptonic decay width $\Gamma_{\ell\ell}$ (in leading order)

$$\Gamma_{\ell\ell} = \frac{4\alpha^2}{9{m_c}^2} \cdot \left|R_{J/\Psi}(0)\right|^2 \tag{2.42}$$

Nevertheless, the CSM is 'only' a model and incomplete in some points. There is no theorem which proves the validity of the factorisation in equation 2.41 and it is not clear whether this factorisation will hold for higher order corrections. Relativistic corrections, taking the relative velocities of the quark antiquark into account, are neglected but can be included [FKS98, JKGW93]. The CSM does not account for color octet states of the produced $c\bar{c}$ pair during the formation of a charmonium state, although they might contribute due to non perturbative radiation of soft gluons. Finally, the cross section for p-wave state charmonia (e.g. χ_c) shows infrared divergences. Large normalisation uncertainties on predictions in the CSM arise from the dependence on the charm quark mass and α_s.

Experimentally, the predictions of the CSM in leading order (LO) fail to describe the measured cross sections in several analyses.

The most prominent measurement in this scope was published in 1997 from the CDF collaboration at the TEVATRON ($\sqrt{s} \approx 1.96\,\text{TeV}$). In figure 2.8(a) the published differential cross sections as a function of the transverse momentum of the J/Ψ are shown [BK97]. CDF data are compared to predictions calculated in CSM (LO) drawn as dotted line. 'Color octet' predictions in the figure are subject of the next section of this thesis. The predicted P_T spectrum of the J/Ψ meson is too soft, i.e. it falls off steeper with respect to the data and the absolute normalisation is found to be more than one order of magnitude below the data. In fixed target experiments, a difference in the absolute normalisation of up to two orders of magnitudes is observed (e.g. E789 at FERMILAB [E78997]).

The slope of the $P_{T,\Psi}$ spectrum in measurements at HERA [H102b] confirms the CDF results. The CSM LO (dotted line in fig. 2.8(b)) prediction overshoots the data at low values of the transverse momentum and is almost one order of magnitude below the data at large values of $P_{T,\Psi}$.

Next to Leading Order (NLO)

It was expected, that contributions from next to leading order diagrams (NLO, $\mathcal{O}(\alpha, \alpha_s^3)$) should change the absolute normalisation in the calculation by a factor of two. The photoproduction of inelastic J/Ψ mesons in direct photon gluon fusion was calculated in NLO by Michael Krämer and Peter Zerwas in 1995 [Kra96]. The biggest uncertainty on the calculation arises from the variation of the renormalisation scale, in particular in the case of charm production with the rather small mass compared to beauty quarks. It was surprising, that the NLO terms increase the absolute normalisation of the cross section by roughly one order of magnitude and that the P_T spectrum of the J/Ψ meson becomes much harder with respect to the calculation in leading order. The NLO corrections to the color singlet model are dominated by strong negative contributions at $z \rightarrow 1$ and $P_{T,\Psi} \rightarrow 0\,\mathrm{GeV}$.

In figure 2.8(b) the NLO prediction (dashed line with error band) is compared to a published H1 measurement, the data are very well described. The error band is obtained by a variation of the running coupling ($\alpha_s = 0.1200 \pm 0.0025$) and the charm mass ($m_c = 1.4 \pm 0.1\,\mathrm{GeV}$). The results do not allow for large contributions from different processes.

A recent calculation by Fabio Maltoni et al. [Mal07, ACL+08] shows the importance of higher order corrections for the description of J/Ψ and Υ meson production in $p\bar{p}$ collisions at the TEVATRON. Figure 2.9 shows the calculated cross section as a function of the transverse momentum of the J/Ψ meson and the Υ ($b\bar{b}$) meson respectively. CDF measurements are compared to CSM calculations at leading order (LO) and next to leading order (NLO). In addition shown are predictions which estimate the influence of next to next to leading order (NNLO) terms. The NLO calculations reduce the discrepancy by one order of magnitude compared to the LO calculation, but are still not able to describe the CDF data. However, also the estimated NNLO contributions have a significant effect on the calculated cross sections which was not expected. They are capable of modelling the data in the case of the Υ meson. The predicted J/Ψ cross section at NNLO is slightly too low, though already very close to the data in shape and normalisation.

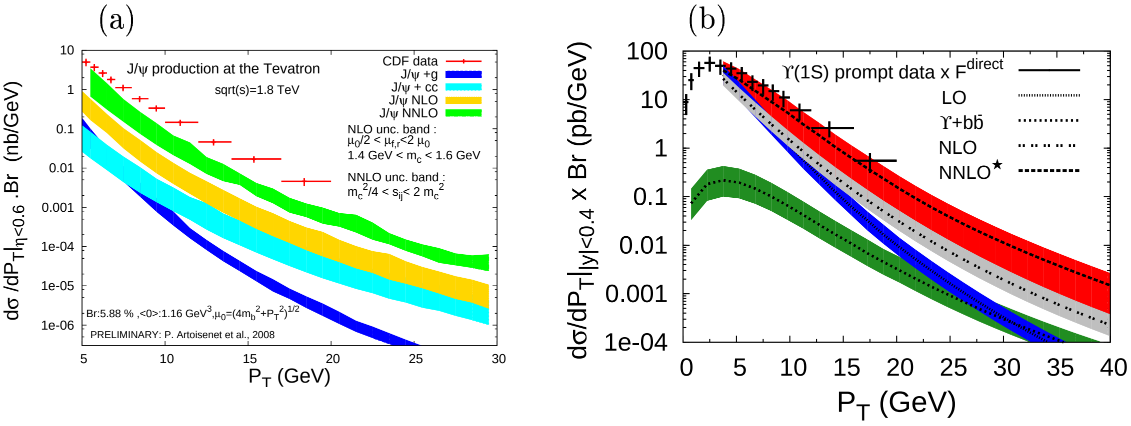

Figure 2.9: Cross sections as a function of the transverse momentum of (a) the J/Ψ meson and (b) the Υ meson. The CDF data are compared to theoretical calculations up to NNLO in the color singlet model.

k_T Factorisation

A different approach to account for higher order corrections is the k_T factorisation approach, where the cross section factorises into the calculation of an off shell matrix element convoluted with an unintegrated (i.e. k_T dependent) gluon density [CCH91, CE91]. In k_T factorisation 'small x' logarithms ($[\ln(\mu^2/\Lambda^2)\alpha_s]^n$, $[\ln(\mu^2/\Lambda^2)\ln(1/x)\alpha_s]^n$, $[\ln(1/x)\alpha_s]^n$) are resummed to all orders in n, taking into account the effects of finite transverse momenta of the partons. This resummation leads to an 'unintegrated' gluon density $\mathcal{A}(x, {k_T}^2, \bar{q}^2)$, which depends on the k_T of the parton and allows the initial partons to be off shell in the parton evolution using the CCFM evolution equation.

Figure 2.10 shows the feynman diagrams for the collinear approach (DGLAP) in leading and next to leading order, for a process with a resolved photon and for the k_T factorisation approach in leading order. In the collinear approach the initial parton is emitted parallel to the direction of the proton (collinear) and always treated as massless. In leading order the parton enters the hard subprocess with $k_T = 0$ and a transverse momentum of the J/Ψ meson can only originate from the hard gluon emitted according to the CSM. In next to leading order a gluon in the parton evolution can be emitted, resulting in $k_T > 0$ in the hard subprocess. In the case of a resolved process, the k_T in the hard interaction arises from the photon. All three processes are already included in the k_T factorisation approach at leading order to leading logarithmic accuracy, because the incoming parton is allowed to be off shell and its virtuality is only restricted by the kinematics.

Therefore the k_T factorisation approach includes naturally NLO diagrams and processes with resolved photons. It will turn out, that calculations using a k_T factorisation approach achieve the best description of the measured cross sections and polarisations.

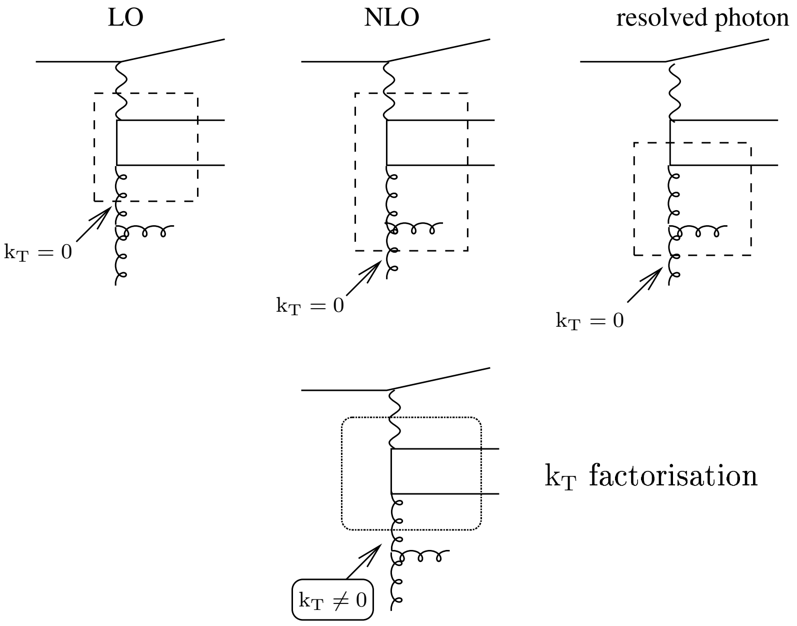

Figure 2.10: Feynman diagrams for boson gluon fusion in leading and next to leading order, for BGF with a resolved photon and in k_T factorisation.

Factorisation Ansatz in NRQCD

Originally the factorisation ansatz in non relativistic QCD (NRQCD)[4] was introduced by Geoffrey Bodwin, Eric Braaten and Peter Lepage for the prediction of decay rates of p-wave charmonium states ($\chi_{c_{0,1,2}}, \mathrm{h_c}$) [BBL92]. In the middle of the 90's they expanded it in order to be able to describe the production rates of heavy quarkonia at high P_T in the CDF data [BBL95].
The NRQCD ansatz caught the attention of the physicists, because it is able to describe the CDF cross section in leading order over the whole P_T range (cf. solid line in figure 2.8). In contrast to the CSM, color octet states with soft gluon radiation contribute to the cross section in the NRQCD ansatz, and the $c\bar{c}$ pair in NRQCD does not have to be produced in a color singlet state. Due to the additional color octet contributions, the factorisation ansatz in NRQCD is often referred to as 'color octet model' (COM).
The charmonium production cross section in NRQCD can be written as the sum of all n possible contributions

$$\sigma\left(\mathrm{A}+\mathrm{B}\rightarrow \mathrm{J}/\Psi+\mathrm{X}\right)=\sum_{n} c_n\left(\mathrm{A}+\mathrm{B}\rightarrow \mathrm{c\bar{c}[n]}+\mathrm{X}\right)\times\left\langle \mathcal{O}_n^{\mathrm{J}/\Psi}\right\rangle , \tag{2.43}$$

where $c\bar{c}\,[n]$ denotes a quark pair in a distinct color, spin and angular momentum state. Each summand in this cross section factorises into a short distance part c_n,

---

[4] Non relativistic QCD is an effective field theory in which the charm and anticharm quark in the charmonium are treated non relativistically.

where a $c\bar{c}$ pair with vanishing relative momentum is produced, and long distance matrix elements (LDME) $\left\langle \mathcal{O}_n^{J/\Psi} \right\rangle$ for the non perturbative transition into a physical quarkonium state.

The short distance part is calculable in perturbation theory in $\alpha_s(2m_c)$, including all lines in the feynman diagram which are off shell by at least m_c. The non perturbative LDMEs can be determined experimentally or calculated in lattice QCD. They are expected to be 'universal' (provided that the factorisation holds) and predictions for an experiment can be calculated using LDMEs determined at another experiment.

In the first place, equation 2.43 contains an infinite number of LDMEs $\left\langle \mathcal{O}_n^{J/\Psi} \right\rangle$. Using the velocity scaling rules introduced with the non relativistic QCD, the cross section can be translated to an expansion in powers of the relative momentum v of the two quarks in the charmonium and truncated at a certain power of v. Typical velocities in the case of charmonium are small ($v^2 \approx 0.3$), hence the cross section can be calculated as a double expansion in α_s and v.
At HERA the leading order term in α_s is the color singlet state $[\underline{1}, {}^3S_1]$, which scales with v^3. Contributions from color octet states at the next order ($\propto v^7$, $[\underline{8}, {}^1S_0]$,$[\underline{8}, {}^3S_1]$,$[\underline{8}, {}^3P_{0,1,2}]$) are already suppressed by a factor v^4. This has two consequences, the NRQCD contains the CSM in the limits of small relative velocities ($v \rightarrow 0$) and contributions from color octet states can only become significant, if the corresponding short distance coefficient c_n is large. The $[\underline{8}, {}^3S_1]$ terms result in the same kinematics as the color singlet term and can be neglected due to the suppression by v^4. The other color octet terms contain additional diagrams with gluon exchange via the t-channel, hence they have a different behaviour as a function of P_T and z. They are expected to contribute strongly at large values of the elasticity ($z \gtrsim 0.9$), where it is unfortunately impossible to measure cross sections for inelastic charmonium production at HERA, because the selected events are dominated by diffractively produced J/Ψ mesons, which have a much higher production cross section in this elasticity range.

The necessary LDMEs to calculate predictions for the HERA experiments have to be extracted in the very low transverse momentum range of the TEVATRON. Therefore uncertainties on the determined values are very large. In particular the electroproduction measurement from H1 [H102a] yields deviations from the NRQCD predictions at large values of the elasticity z and in the description of the slope of the Q^2 and $P_{T,\Psi}$ spectrum.

2.7 Polarisation Variables

A measurement of the polarisation of the J/Ψ meson provides a tool to check the validity of the different models for the production of inelastic J/Ψ mesons in addition

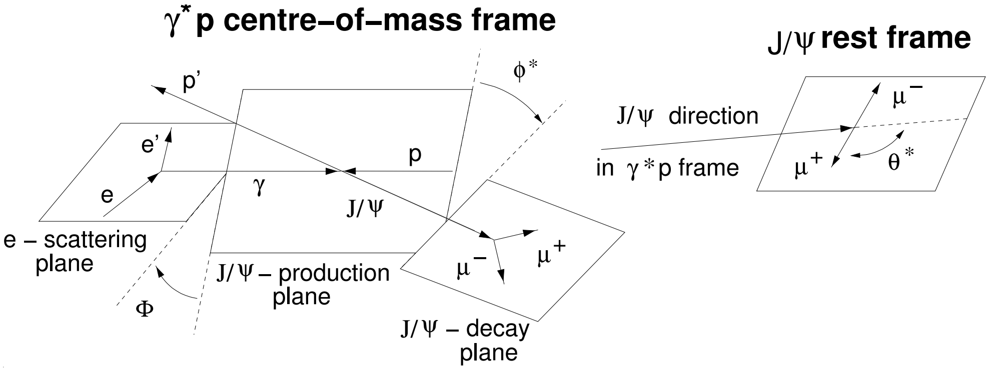

Figure 2.11: Illustration of the production and decay angles used for the determination of the polarisation of the J/Ψ meson.

to the cross section measurement. In particular contributions from color octet states are expected to become apparent in the measured polarisation of the J/Ψ meson.

It is not possible to measure the polarisation of the J/Ψ meson directly, but its helicity structure can be obtained from the angular distributions of the J/Ψ decay leptons.
The measurement of the decay angles is performed in the (s-channel) helicity frame, in which the z axis is defined by the direction of flight of the J/Ψ meson in the γp center of mass frame. For this purpose, three decay angles, which are illustrated in figure 2.11, are defined:

Θ^*: The polar angle of the beam sign decay lepton in the J/Ψ rest frame, where $\Theta^* = 0\,^\circ$ denotes the flight direction of the J/Ψ meson in the γp center of mass system.

ϕ^*: The angle between the production and the decay planes of the J/Ψ meson.

Φ: The angle between the scattering plane of the beam lepton and the production plane of the J/Ψ meson.

At values of $\cos(\Theta^*) \approx \pm 1$, one of the decay leptons is emitted almost oppositely to the direction of flight of the J/Ψ meson in the γp center of mass frame. That causes a small momentum of this decay lepton in the laboratory frame and most of these leptons do not pass the track cuts. As a consequence, the acceptance for extreme values of $\cos(\Theta^*)$ collapses.
The acceptance drops also, if the production and decay plane of the J/Ψ meson become coplanar ($\phi^* \approx 0\,^\circ \vee \phi^* \approx \pm 180\,^\circ$). In this case, the transverse momentum of one of the decay leptons is opposite to the incoming proton and its transverse momentum becomes small in the laboratory frame.
To calculate the last angle, Φ, the detected scattered beam lepton is needed. It is only accessible in electroproduction and is not taken into account in the scope of this analysis.

The three decay angles can be written in terms of the momentum vectors of the particles

$$\begin{aligned}
\cos(\Theta^*) &= \frac{\vec{\mathrm{P}}_{\mathrm{J}/\Psi} \cdot \vec{\mathrm{P}}_{\mu^*}}{|\vec{\mathrm{P}}_{\mathrm{J}/\Psi}| \cdot |\vec{\mathrm{P}}_{\mu^*}|}, && (2.44)\\
\cos(\phi^*) &= \frac{\left(\vec{\mathrm{q}} \times \vec{\mathrm{P}}_{\mathrm{J}/\Psi}\right) \cdot \left(\vec{\mathrm{P}}_{\mathrm{J}/\Psi} \times \vec{\mathrm{P}}_{\mu}\right)}{\left|\vec{\mathrm{q}} \times \vec{\mathrm{P}}_{\mathrm{J}/\Psi}\right| \cdot \left|\vec{\mathrm{P}}_{\mathrm{J}/\Psi} \times \vec{\mathrm{P}}_{\mu}\right|}, && (2.45)\\
\cos(\Phi) &= \frac{\left(\vec{\mathrm{q}} \times \vec{\mathrm{P}}_{\mathrm{J}/\Psi}\right) \cdot \left(\vec{\mathrm{k}} \times \vec{\mathrm{k}}'\right)}{\left|\vec{\mathrm{q}} \times \vec{\mathrm{P}}_{\mathrm{J}/\Psi}\right| \cdot \left|\vec{\mathrm{k}} \times \vec{\mathrm{k}}'\right|}. && (2.46)
\end{aligned}$$

The used momentum vectors were introduced in section 2.1, $\tilde{\mathrm{P}}_{\mathrm{J}/\Psi}$ is the momentum vector of the J/Ψ meson in the photon proton rest frame, $\vec{\mathrm{P}}_{\mu^*}$ denotes the momentum of the muon in the rest frame of the J/Ψ meson.
The decay angular distribution of the J/Ψ meson can be expressed in terms of the three decay angles as

$$\begin{aligned}
\frac{\mathrm{d}\sigma}{\mathrm{d}\Omega\mathrm{dy}} \propto 1 \quad &+ \quad \alpha(y) \cdot \cos^2(\Theta^*) + \mu(y) \cdot \sin(2\Theta^*) \cos(\phi^*) \\
&+ \quad \frac{\nu(y)}{2} \cdot \sin^2(\Theta^*) \cos(2\phi^*) \,. && (2.47)
\end{aligned}$$

Each of the decay angles can be parametrised separately after integrating equation 2.47

$$\begin{aligned}
\frac{\mathrm{d}\sigma}{\mathrm{dcos}(\Theta^*)\mathrm{dy}} &\propto 1 + \alpha(y) \cdot \cos^2(\Theta^*) && (2.48)\\
\frac{\mathrm{d}\sigma}{\mathrm{d}\phi^*\mathrm{dy}} &\propto 1 + \frac{\alpha(y)}{3} + \frac{\nu(y)}{3} \cdot \cos(2\phi^*) \,. && (2.49)
\end{aligned}$$

Using these equations, the polarisation variables α and ν are obtained by a simultaneous fit to the measured cross sections as a function of $\cos(\Theta^*)$ and ϕ^*. The J/Ψ meson is transversely polarised for $\alpha = +1$, longitudinally polarised for $\alpha = -1$ and unpolarised for $\alpha = 0$.

Since the decay angular distribution parameters are extracted from the shape of the cross sections, the dependence of theoretical predictions on parameters that affect the absolute normalisation of cross sections (e.g. $\mathrm{m_c}, \alpha_\mathrm{s}, \mu_r, \mu_f$, PDFs) cancels to a large extent, hence the uncertainty of the predictions is reduced significantly. However a data sample with huge statistics is needed in order to be able to determine the polarisation variables precisely.

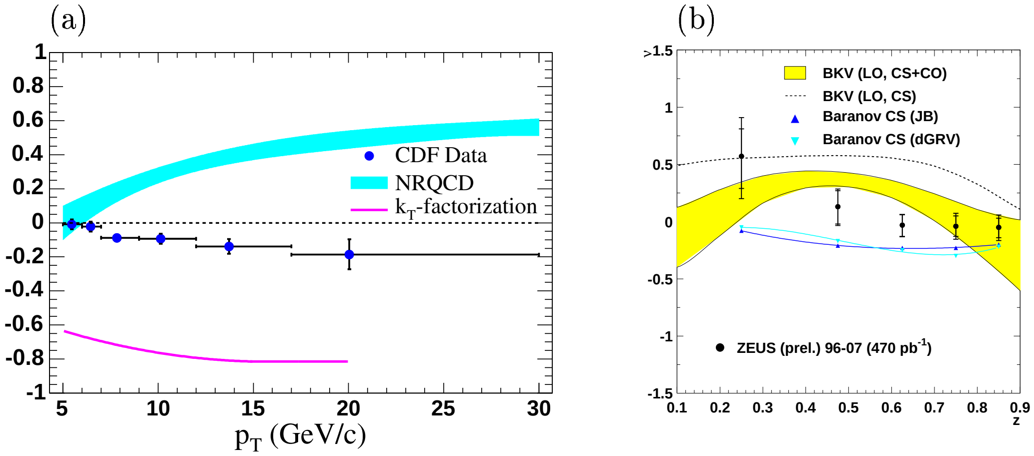

Figure 2.12: (a) Polarisation variable α measured at CDF and (b) a preliminary ZEUS measurement of ν.

In the factorisation ansatz in NRQCD, the production of inelastic J/Ψ mesons at large transverse momenta is dominated by gluon splitting ($g \longrightarrow c\bar{c}$). These J/Ψ mesons should inherit the transverse polarisation ($\alpha = +1$) from the gluon. Figure 2.12(a) shows, that the continuous rise of the NRQCD prediction towards larger $P_{T,\Psi}$ conflicts with the CDF measurement (run II) [CDF07]. The CDF data are unpolarised at low transverse momentum and become slightly longitudinally polarised towards larger $P_{T,\Psi}$. Neither the CSM nor NRQCD predict a longitudinal polarisation of the J/Ψ meson ($\alpha < 0$). Only calculations using k_T factorisation are able to predict longitudinally polarised J/Ψ mesons up to now. While the k_T factorisation predictions plotted in the CDF result are far below the data, a ZEUS measurement of α is well modelled by a calculation using unintegrated parton densities done by Sergey Baranov [ZEUS03]. The polarisation measurements at ZEUS and H1 are consistent with an unpolarised J/Ψ meson (within large errors), the predictions in the CSM LO cannot describe the measurements at large values of z. The data favour predictions obtained in NRQCD or CSM using k_T factorisation.

Up to now, no calculation in next to leading order of the polarisation variables is available. Since only the shape of cross sections is relevant for the measurement, it is not expected that the NLO calculations change the predictions significantly. Nevertheless, an NLO calculation is necessary to quantify theoretical uncertainties and to exclude surprises as seen in the calculation of the P_T spectrum in the color singlet model.

2.8 Diffraction

In addition to the inelastic production described in the sections before, J/Ψ mesons can be produced in diffraction. In diffractive processes, particles scatter as a whole

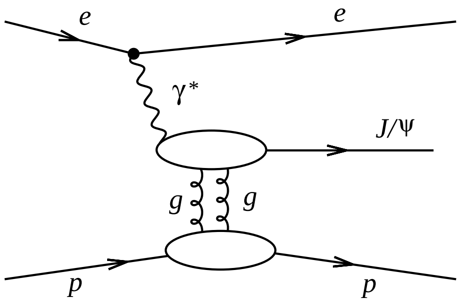

Figure 2.13: Feynman diagram of the diffractive J/Ψ production via the exchange of a two gluon system. In the Regge theory, the gluon system is replaced by a pomeron trajectory.

without the exchange of quantum numbers, just with momentum transfer. In the case of diffractive processes with protons, the dissociation of the proton is allowed. If the proton leaves the detector intact, the events are called 'elastic'. The elasticity of the J/Ψ mesons in proton dissociation events is $z \geqslant 0.95$ and $z \approx 1$ in the case of elastic events.

The diffractive production of J/Ψ mesons is possible, because the J/Ψ has the same quantum numbers as the photon, $J^{PC} = 1^{--}$, $Q = S = C = B = 0$, where Q denotes the charge, S the strangeness, C the charmness and B the bottomness. Figure 2.13 shows the feynman diagram for the diffractive J/Ψ production. The incoming photon fluctuates into a virtual J/Ψ meson. Afterwards the virtual J/Ψ interacts with the proton and finally the virtual J/Ψ meson transforms into a real J/Ψ. It is assumed, that the time between the three processes is 'long' and the processes can be treated independently. In the interaction with the proton a color neutral object is exchanged. Depending on the kinematics, this can be either a pomeron trajectory (Regge theory) or a system of two gluons in pQCD.

The experimental signature of diffractive events is a very clean hadronic final state, which contains only the decay particles of the J/Ψ meson and a large rapidity gap between the J/Ψ and the remaining hadronic final state (coming from the dissociated proton). A detailed description of diffractive J/Ψ production can be found for instance in [Fle04].

The diffractive cross section is much larger compared to the inelastic production, hence sizeable contributions from diffractively produced Ψ(2S) mesons with a subsequent decay into J/Ψ + X are expected in this analysis.

2.9 Monte Carlo Generators and Detector Simulation

Monte Carlo generators are used to model the interaction of high energetic particles as correctly as possible from the initial particles to the hadronic final state. The process is split up into two parts, the event generation and the detector simulation. The first step during the generation of events is the evolution of the initial state particles, as calculated in parton showers and parton evolution equations. The resulting particles serve as input for the calculation of the hard matrix element in leading order perturbation theory. Finally, the measurable hadronic final state is formed. Random number generators are used to generate events based on model dependent probability distributions. The event generation leads to a set of four momentum vectors, which should be as close to the real physics as possible. In the generated final state, only particles with a lifetime of at least 10^{-8} s are taken into account, which may decay within the detector simulation afterwards.
The set of four vectors is handed over to the GEANT based H1 detector simulation H1SIM. The purpose of H1SIM is to simulate a detector response, which corresponds to the raw data from ep collisions. In order to achieve a good agreement between raw data and simulation, geometry and (dead) material of the detector have to be modelled precisely in GEANT and the resolution and hit efficiency of the various detector components need to be simulated correctly.
From this point onwards, data and simulation are treated equally. The (simulated) raw data is fully reconstructed in the H1 reconstruction software H1REC and used as starting point for data analyses.

The two Monte Carlo generators CASCADE and EPJPSI, used in the context of this analysis, are explained briefly in the following. CASCADE Monte Carlo samples with inelastic J/Ψ mesons decaying into muons or electrons respectively are used to determine acceptance and efficiencies in order to correct the number of signal events in this analysis. The samples are generated using the unintegrated gluon density 'CCFM J2003 set 3'. Control plots comparing data and CASCADE Monte Carlo distributions are shown in the chapters 7 and 8.

CASCADE

The full hadron level event generator CASCADE contains an implementation of the k_T factorisation approach using CCFM unintegrated gluon distribution and off shell matrix elements for ep, γp and p$\bar{\text{p}}$ collisions. The J/Ψ meson production via (virtual) photons in boson gluon fusion ($\gamma^{(*)} + \text{g} \rightarrow J/\Psi + g$) is modelled in the color singlet model in leading order. In ep collisions at HERA, the process is treated as photon exchange in the Weizsäcker Williams approximation (WWA). The WWA considers the electromagnetic interaction of particles as an interaction of a particle with a photon flux corresponding to the field of another particle.

The hard subprocess is calculated using off shell matrix elements [LZ03,BZ03,Bar02] convoluted with the unintegrated gluon density $\mathrm{x}\mathcal{A}(\mathrm{x}, \mathrm{k_T}^2, \bar{q}^2)$. The initial cascade is generated in a backward evolution approach from the hard scattering process towards the proton. This approach is necessary to achieve a reasonable efficiency for the event generation. For the CCFM evolution equation it is proven, that backward and the forward evolution yield the same result. For a backward evolution, however, the unintegrated gluon density must be determined beforehand. This is done by a fit of a solution of the CCFM equation to the structure function $\mathrm{F_2}(\mathrm{x}, \mathrm{Q}^2)$.
The hadronisation is done in the Lund string fragmentation as implemented in JETSET and PYTHIA [Sjo94].

EPJPSI

In the event generator EPJPSI [Jun92], the direct and resolved production of J/Ψ mesons in γp, ep, μp, p$\bar{\mathrm{p}}$ and pp is simulated according to the color singlet model in leading order in the Weizsäcker Williams approximation.
During the event generation, relativistic corrections for the relative velocity of the quarks can be taken into account [JKGW93]. These corrections lead to a strong rise of the cross section towards large values of the elasticity, while the cross section is expected to break down towards $\mathrm{z} = 1$ without these corrections due to the end of the phase space [BJ81].
As in CASCADE, the hadronisation is done using the Lund string model.

CHAPTER 3

The H1 Detector at HERA

This chapter gives a brief review of the HERA accelerator and the H1 experiment. The description concentrates on the detector components which are relevant for this analysis. A detailed description of the H1 detector can be found in [H197a, H197b].

3.1 The Hadron Electron Ring Accelerator (HERA)

HERA was an unique collider to study the proton structure in $e^{\pm}p$ collisions. An overview of HERA and the preaccelerator chain is plotted in figure 3.1. The HERA tunnel has a circumference of approximately 6.3 km composed of four 360 m long straight sections connected with four segments of a circle with a radius of 797 m. The tunnel contains a beam pipe with normal conductive magnets for the electrons

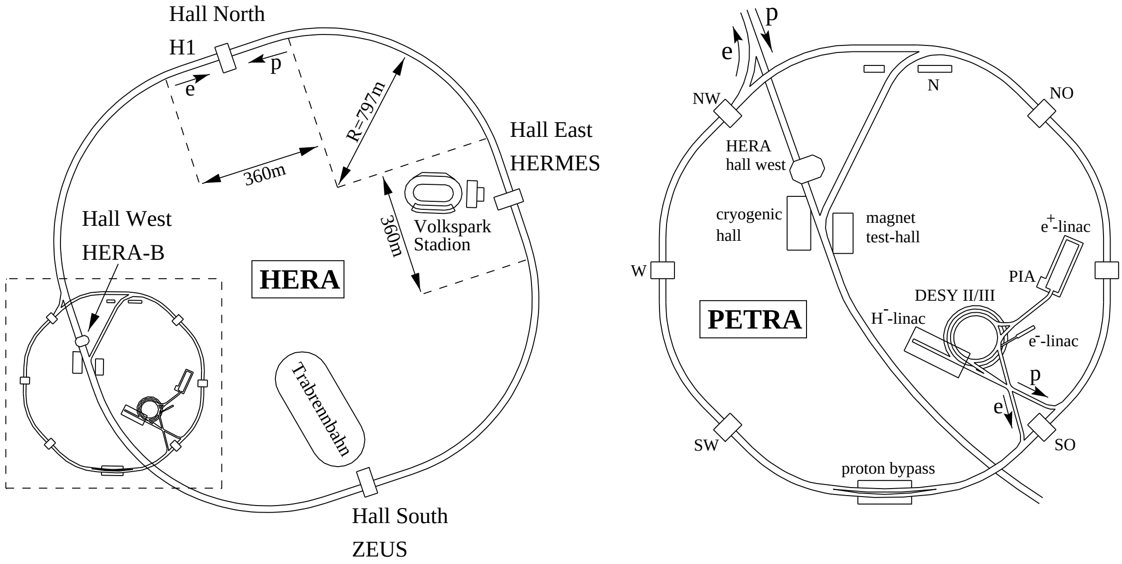

Figure 3.1: Overview of the HERA ring, the four experiment halls and the preaccelerator chain.

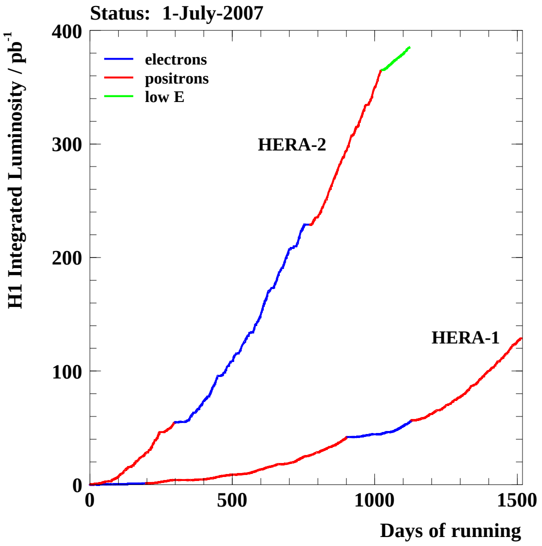

Figure 3.2: Integrated luminosity collected with the H1 experiment as a function of time for both HERA running periods.

and a superconducting proton ring. The collision rate amounted to 10.4 MHz (i.e. 96 ns gap between possible collisions) at a centre of mass energy of $\sqrt{s} \approx 320\,\text{GeV}$, calculated from beam energies of $E_p = 920\,\text{GeV}$ for the protons and $E_e = 27.6\,\text{GeV}$ for the electrons.

During the HERA I running period (1992–2000) an integrated luminosity of $\mathcal{L} \approx 130\ \text{pb}^{-1}$ was collected (cf. fig. 3.2). In the years 2000–2003 new focussing magnets were installed close to the interaction regions in order to achieve a higher luminosity. The installation of these magnets made modifications to the detector necessary which will be addressed in the following section. In 2004 the HERA II data taking period started. After some problems with beam induced backgrounds in the beginning, an integrated luminosity of almost $400\,\text{pb}^{-1}$ was collected until the end of HERA data taking in June 2007.

In the middle of each straight tunnel section one experiment was operated. The experiments H1 (hall north) and ZEUS (hall south) studied the proton structure in collisions of electrons and protons. HERMES (hall east) analysed the spin structure of the nucleons in collisions of the electron beam with a polarised gas target. HERA-B (hall west) was primarily designed to observe CP violation in the mixing of B mesons produced in collisions of the proton beam with different wire targets. In autumn 2004 the HERA-B experiment was taken out of the beam and dismantled.

The analysis presented in this thesis was carried out using the data taken with the H1 experiment, which will be introduced in the next section.

3.2 The H1 Detector

The H1 experiment was a multi purpose detector with an angular coverage of almost 4π. Figure 3.3 shows a schematic overview of H1 and its subdetectors.

The right handed coordinate system of H1 defines the z axis in the flight direction of the protons, the x axis points towards the centre of HERA and the y axis points upwards. The nominal interaction point in the middle of the detector is defined as origin of the coordinate system. Often a cylindrical coordinate system (r, Θ, Φ) is used, where r denotes the radial length, Θ is the polar angle measured with respect to the positive z axis and Φ is the azimuthal angle relative to the positive x axis. The region of positive z values is also called ‘forward’ region, while negative z values are in the ‘backward’ region. In order to account for a boost due to the different beam energies, H1 was designed asymmetrically with more instrumentation in the forward region.

The detector was built from several subdetector components, which are arranged cylindrically around the beam pipe. The tracking system ($\boxed{1}$ – $\boxed{5}$ in fig. 3.3) was installed as closely as possible to the beam pipe. It was surrounded by the backward calorimeter SpaCal ($\boxed{6}$) and the liquid Argon calorimeter ($\boxed{7}$,$\boxed{8}$). Trackers and calorimeters were covered by the superconducting coil which generated a homogeneous magnetic field of B=1.16 T ($\boxed{9}$) and the iron return yoke ($\boxed{10}$). The iron return yoke was instrumented with limited streamer tubes and acted as central muon detector. In the forward direction a toroid magnet (B=1.6 T) allowed an independent momentum measurement of muons in the forward muon detector (FMD).

The subdetectors used in this analysis are briefly described in the following sections.

Central Tracking Detector

The purpose of the Central Tracking Detector (CTD) was the measurement of track and vertex information for charged particles in the central region of the detector ($20° \leqslant \Theta \leqslant 160°$). Due to the magnetic field of B=1.16 T, the measured tracks were curved with a radius depending on the transverse momentum of the particle. The CTD consisted of five radial subdetectors around the beam pipe which are relevant for this analysis. An overview of the subdetectors of the CTD in the r-Φ plane is given in figure 3.4.

$\boxed{1}$ Central Silicon Tracker (CST)

The CST provided very accurate track hits in r-Φ and z and precise vertex information in order to identify secondary vertices of long lived particles. The two silicon layers at 5 cm and 10 cm around the beam pipe do not allow an independent track reconstruction, but the CST information improves the accuracy of the CJC hits.

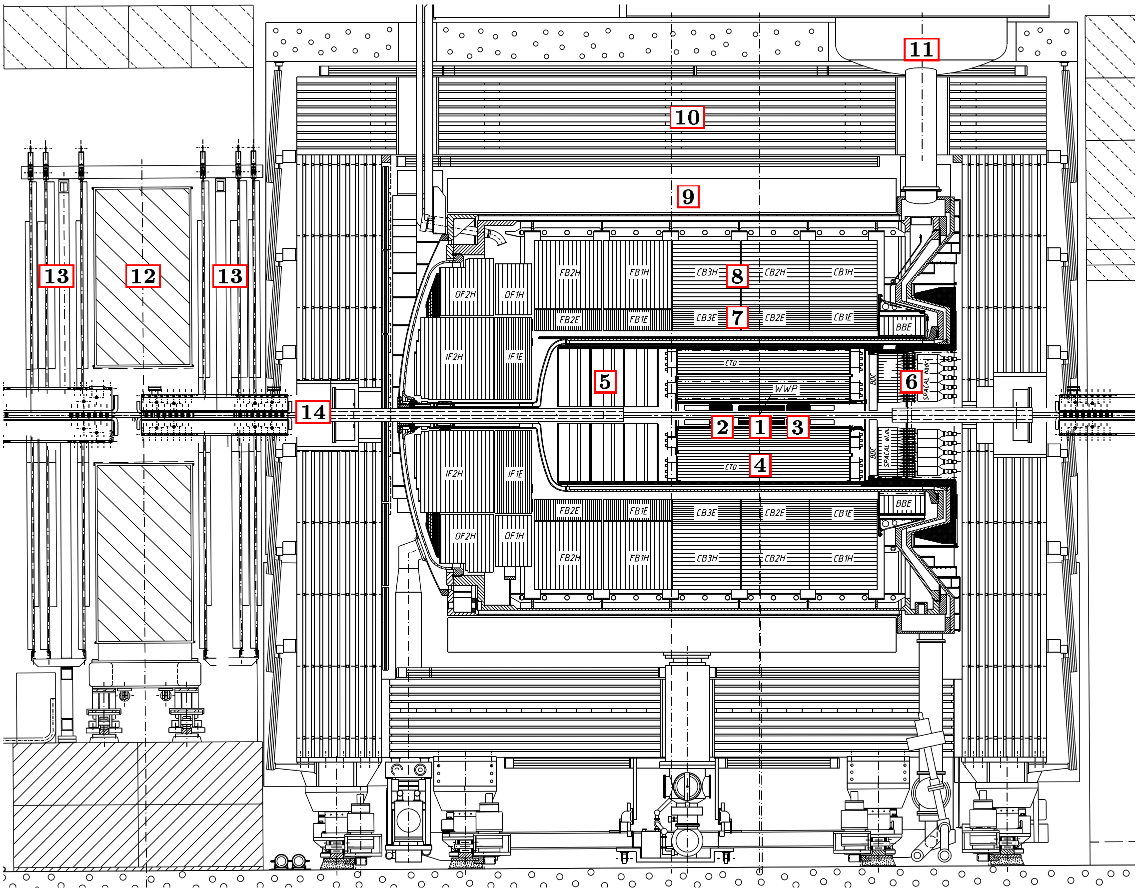

No.	Detector Component	No.	Detector Component
1	Central Silicon Tracker (CST)	8	Hadronic Calorimeter (LAr)
2	Forward Silicon Tracker (FST)	9	Superconducting Coil
3	Backward Silicon Tracker (BST)	10	Instrumented Iron (CMD)
4	Central Tracking Detector (CTD)	11	Liquid Argon Cryostat
5	Forward Tracking Detector (FTD)	12	Muon Toroid Magnet
6	Spaghetti Calorimeter (SpaCal)	13	Forward Muon Detector (FMD)
7	Electromagnetic Calorimeter (LAr)	14	Beam Pipe

Figure 3.3: Schematic view of the H1 detector in the y-z plane. The protons enter the detector in the middle of the detector from the right side, the electrons from the left.

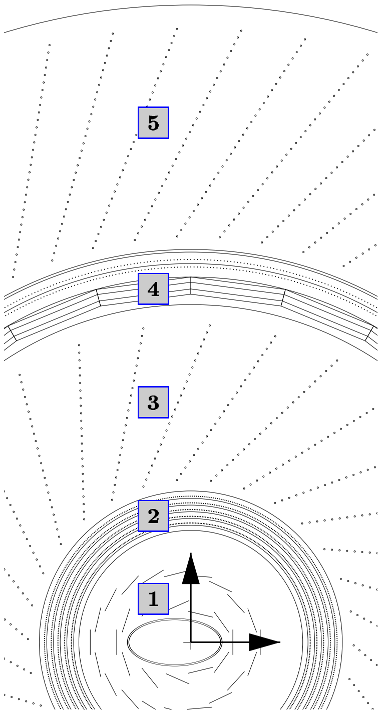

No.	Detector Component
1	Central Silicon Tracker (CST)
2	Central Inner Proportional Chamber (CIP)
3	Inner Central Jet Chamber (CJC1)
4	Central Outer z Chamber (COZ)
5	Outer Central Jet Chamber (CJC2)

Figure 3.4: Radial layout of the central tracking detector in the r-Φ plane.

2 Central Inner Proportional Chamber (CIP)

The CIP was a multi wire proportional chamber with five layers. Nevertheless the CIP provided important trigger signals depending on the z position of the event vertex for the online event selection (cf. chapter 5).

3 + 5 Central Jet Chambers (CJC1, CJC2)

The two central jet chambers were the most important tracking detectors of the H1 experiment. The CJCs covered an angular range of $20^\circ \leqslant \Theta \leqslant 160^\circ$ within a radius of approximately 20 cm to 85 cm. They were built from 30(60) drift cells with 24(32) sensor wires each. The sense wires ran parallel to the beam axis tilted by 30° in the radial direction. This ensured that the curved tracks could be measured in at least two cells in order to improve the track resolution and to avoid ambiguities due to mirror hits.

The CJCs provided a very good resolution in r-Φ ($\sigma_{r-\Phi} \approx 170\ \mu\mathrm{m}$), with an expected worse resolution in z ($\sigma_z \approx 22\,\mathrm{mm}$). The possible resolution for the momentum measurement is $\frac{\sigma_{\mathrm{P_T}}}{\mathrm{P_T}^2} = 0.005\,\mathrm{GeV}^{-1} \oplus 0.015$ [H107a].

Secondary to the momentum measurement, a part of the tracking information of the CJCS is important for the calculation of trigger elements (cf. chapter 5).

4 Central Outer z Chamber (COZ)

In between the two CJCs the central outer z chamber COZ was installed to provide an accurate measurement of the z position as input to track reconstruction. The COZ was segmented into 24 rings with a length of 9 cm ($L_{COZ} = 2.16$ m) and covers polar angles from 25° to 155°. Each of the 24 rings was split into 24 individual drift cells in Φ. The COZ achieved a good z resolution ($\sigma_z \approx 350$ µm) because the sense wires were strung perpendicular to the z axis.

Overall the central tracking system provided a track resolution at the vertex of $\sigma_{r-\Phi} \approx 40$ µm in the $r - \Phi$ plane and $\sigma_z \approx 70$ µm in the z direction.

Calorimeters

The H1 experiment had two main calorimeters, the spaghetti calorimeter (SpaCal) in the backward region of the detector and the liquid argon calorimeter (LAr) in the forward and central region. The main purpose of the SpaCal was the identification of scattered beam leptons up to photon virtualities of $Q^2 \approx 100\,\mathrm{GeV}^2$. The LAr was used for the measurement of the hadronic final state and scattered leptons with large virtualities Q^2. The high granularity of the LAr allowed the identification of electrons and muons down to very low transverse momenta using their specific energy deposition (cf. chapter 4).

Spaghetti Calorimeter (SpaCal)

The SpaCal Calorimeter [H197c, Rey98] started at $z = -1.6$ m and covered the backward angular range ($153° \leqslant \Theta \leqslant 174.5°$) with a diameter of 1.6 m.

The SpaCal had an electromagnetic and a hadronic part. Both were built as sampling calorimeters with lead as absorber and scintillating fibres as detector material. The electromagnetic part was built from 1150 cells with an edge length of 4 cm and a depth of 25 cm, corresponding to approximately 27.5 radiation lengths X_0. The hadronic part was designed similarly to the electromagnetic part with roughly four times larger edge lengths. The depth of 25 cm of the hadronic SpaCal lead to only one hadronic interaction length λ_0. Therefore almost all electrons were stopped in the electromagnetic part of the SpaCal, while the hadronic part acted mainly as veto against hadrons faking a scattered lepton.

During the luminosity upgrade 2000–2003 the inner region of the SpaCal had to be modified in order to install the superconducting GG focussing magnet close to the interaction point. A schematic overview of the inner region of the electromagnetic SpaCal for HERA I and HERA II in the $r - \Phi$ plane is shown in figure 3.5. The innermost layer of the HERA I SpaCal (cf. fig. 3.5(a)) was called 'veto wall'. It was used to ensure that the cluster of the scattered lepton was fully contained in the detector, hence it was possible in HERA I to detect scattered leptons down to $\Theta \approx 178°$ (i.e. $Q^2 \approx 1\,\mathrm{GeV}^2$).

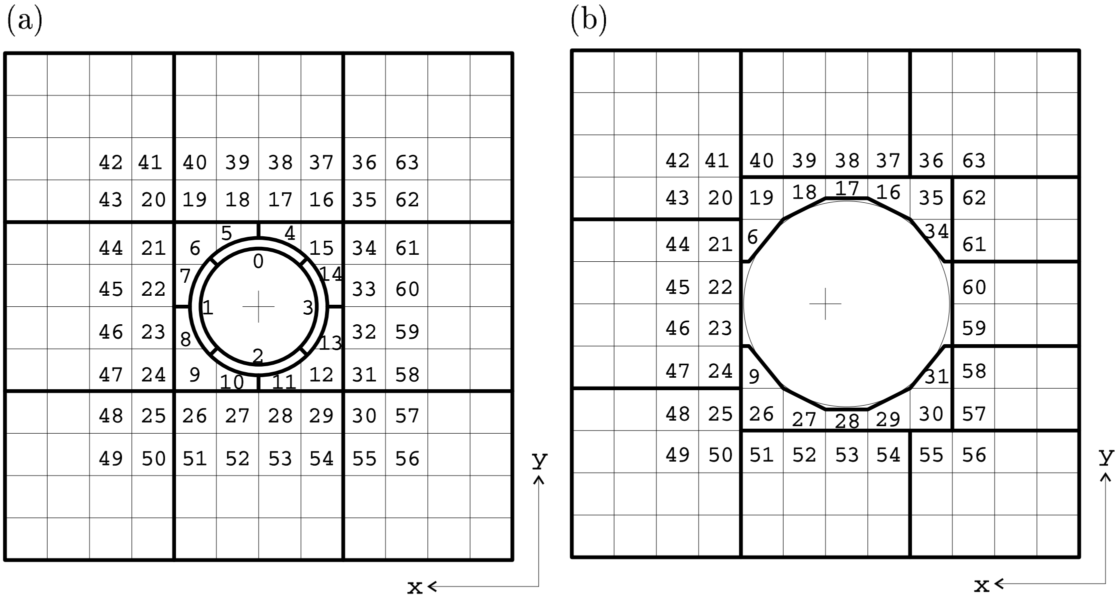

Figure 3.5: The inner region of the spaghetti calorimeter (SpaCal) for (a) HERA I and (b) HERA II (after the modifications during the luminosity upgrade).

The modifications made it necessary to remove some cells in the hadronic part and to rebuild the so called ‘insert’ in the electromagnetic part, the region close to the beam pipe. The new insert was built without veto wall and with a larger radius compared to the HERA I insert. This restricted the angular acceptance of the SpaCal to $\Theta \leqslant 174.5°$ and limits HERA II analyses in electroproduction to $Q^2 \gtrsim 3.5\,\mathrm{GeV}^2$. The center of the SpaCal in HERA II did not coincide with the x-y origin, hence the acceptance in Q^2 was asymmetric as a function of Φ.

Liquid Argon Calorimeter (LAr)

The LAr calorimeter was the main calorimeter of the H1 experiment covering the forward and central region of the detector ($4° \leqslant \Theta \leqslant 153°$). A detailed description can be found in [H193b]. The LAr was built as non compensating sampling calorimeter, separated into an inner electromagnetic and an outer hadronic part. Along the z axis the LAr was segmented into 8 wheels with eight octants in Φ. The detector and absorber layers in the central region of the detector were installed parallel to the beam axis (cf. fig. 3.6(a)) and perpendicular to the beam axis in the forward direction. This design ensured that the impact angle of the particles was larger than 45° in order to avoid that the particles travelled long distances only through absorber or detector material.

In a sampling calorimeter different materials for absorption and detection are used. In the whole LAr calorimeter, scintillating liquid argon was used as

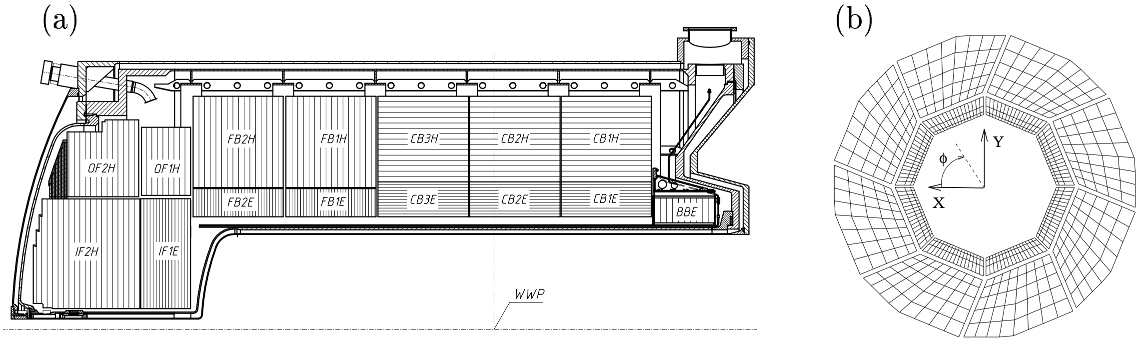

Figure 3.6: (a) Lateral view of the upper half of the LAr calorimeter and (b) cross section of a wheel (in the barrel) in the r-Φ plane.

detector material. The absorber in the electromagnetic part was lead, while in the hadronic part stainless steel was used.

Depending on the polar angle Θ the LAr calorimeter had five to eight hadronic interaction lengths λ_0. The electromagnetic part had 20–30 radiation lengths X_0, i.e. approximately one interaction length λ_0.

The calorimeter was non compensating, meaning that the measured energy response for a hadronic shower was roughly 30 % smaller compared to an electromagnetic shower. The fine granularity of the LAr ($\sim$ 45.000 cells) allowed to distinguish between hadronic and electromagnetic showers based on the shape of the shower. Afterwards it was possible to compensate the energy response software based during the reconstruction. The energy resolution of the LAr calorimeter was determined to be [H193a]

$$\frac{\sigma(\mathrm{E_e})}{\mathrm{E_e}} \approx \frac{0.1}{\sqrt{\mathrm{E_e[GeV]}}} \oplus 1\% \qquad \text{for electrons and} \tag{3.1}$$

$$\frac{\sigma(\mathrm{E_\pi})}{\mathrm{E_\pi}} \approx \frac{0.55}{\sqrt{\mathrm{E_\pi[GeV]}}} \oplus 2\% \qquad \text{for hadrons.} \tag{3.2}$$

Muon System

The muon system of the H1 experiment consisted of two detectors, the central muon detector (CMD) and the forward muon spectrometer (FMD). The FMD ($3^\circ \leqslant \Theta \leqslant 17^\circ$) is not used in this analysis, a detailed description can be found in [B$^+$94].
The central muon detector (CMD) is integrated in the iron return yoke of the superconducting coil. Figure 3.7(a) shows the arrangement of the 64 modules, which are grouped in the forward endcap (FEC, $5^\circ \leqslant \Theta \leqslant 35^\circ$), the forward and backward barrel (BAR, $35^\circ \leqslant \Theta \leqslant 130^\circ$) and the backward endcap (BEC, $130^\circ \leqslant \Theta \leqslant 175^\circ$). The end caps were split into an ‘inner’ region (modules 6–11 and 54–59 respectively) and an ‘outer’ region.

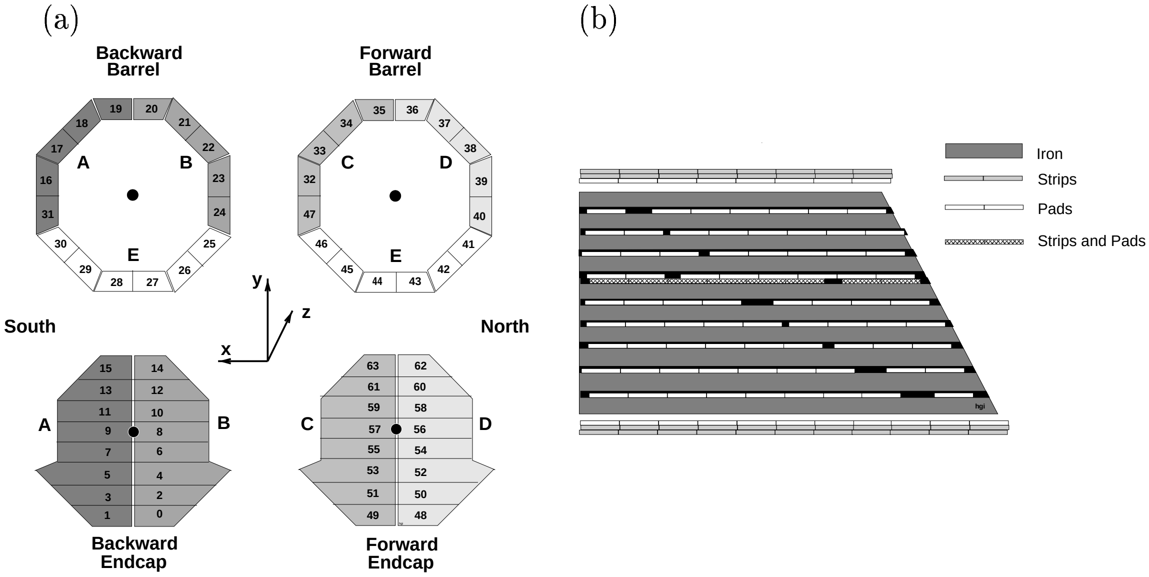

Figure 3.7: (a) Overview of the 64 modules of the central muon detector (CMD) and (b) cross section through a CMD module to illustrate the layer configuration.

The modules (cf. fig. 3.7(b)) were built with ten iron layers (each 7 cm thick). The nine resulting gaps were instrumented with limited streamer tubes. In the gap between the fourth and fifth iron layer a double layer of streamer tubes was installed. In addition to these ten layers, on both sides of the iron return yoke three layers of streamer tubes ('muon boxes') were mounted, hence the CMD had 16 layers in total.

The limited streamer tubes in the layers had a cross section of $9 \times 9\,\mathrm{mm}^2$ and the insides, coated with graphite, acted as cathode. In the middle of each tube a copper beryllium wire (100 µm) was strung. The sense wires ran parallel to the beam axis in the barrel region and parallel to the x axis in the endcaps.

In order to improve the spatial resolution, the outer two layers of the muon boxes and one of the double layers in the middle of the CMD were read out via strip electrodes, which were installed perpendicular to the sense wires. These layers achieved a resolution of $\sigma_\perp \approx 4\,\mathrm{mm}$ perpendicular to the sense wires and $\sigma_{||} \approx 12\,\mathrm{mm}$ parallel to them. The track reconstruction in the CMD is performed in a local coordinate system. Track segments in the end caps and the barrel are not linked, which means that the reconstruction efficiency drops in the transition regions. The purpose of a track reconstruction in the CMD is to probe the geometrical coincidence with a track in the inner tracking detector as described in section 4.2. However the CMD provides a momentum measurement with a rather poor resolution of $\mathrm{dP/P} \gg 30\%$ [Kle92, Kle07].

CHAPTER 4

Lepton Identification

The J/Ψ mesons in this analysis are identified via their leptonic decay into electrons or muons. A good understanding of the identification efficiency of the decay lepton tracks is crucial. The identification and measurement of leptons is composed of two parts. For a good resolution, tracks with the best possible momentum and angular measurement are needed. For a high purity of the signal a good lepton identification is required. Both, the track reconstruction and the lepton identification, are implemented in the H1 reconstruction software H1REC. The description in the following concentrates on the main points, detailed descriptions can be found in [NSS97, Sch97, Sch96].

First the track selection and the muon identification in the muon detectors and the LAr calorimeter, as well as the quality scheme of the KALEP algorithm, are briefly introduced. Afterwards the muon identification efficiency is compared to Monte Carlo simulations using the decay muons of elastic J/Ψ events. Based on the comparisons the simulated events are corrected in order to achieve a good description of the data. In the second part of this chapter a similar study is presented for decay electrons.

4.1 Track Selection

The reconstruction of tracks is based on the hit information of the central (CTD) and forward (FTD) tracking detectors. These tracks are called 'inner tracks'. The reconstruction software distinguishes between three types of tracks: 'central tracks' are reconstructed with hits in the CTD only, 'forward tracks' with hits in the FTD only, and 'combined tracks' use the information of both tracking detectors. The tracks have to fulfil selection cuts in order to guarantee the necessary reliability. Only tracks that are reconstructed to originate from the primary or a secondary vertex are taken into account. A minimum transverse momentum of the track is required and the length of the track in the tracking detector has to be long enough

central tracks (CTD)	
transverse momentum	$P_\perp > 70\,\text{MeV}$
distance to vertex	$\text{dca}' \cdot \sin(\Theta_{\text{Trk}}) < 2\,\text{cm}$
radius of start hit	$R_0 < 50\,\text{cm}$
radial length of track	$\begin{cases} > 10\,\text{cm}, & \text{for } \Theta_{\text{Trk}} < 150^\circ \\ > 5\,\text{cm}, & \text{for } \Theta_{\text{Trk}} > 150^\circ \end{cases}$
combined tracks (CTD + FTD)	
momentum	$P > 0.5\,\text{GeV}$
polar angle of track	$6^\circ < \Theta_{\text{Trk}} < 25^\circ$
radius of start hit	$R_0 < 10\,\text{cm}$
number of modules	$N_{\text{plan}} \geqslant 2$
forward tracks (FTD)	
transverse momentum	$P_\perp > 120\,\text{MeV}$
polar angle	$0^\circ < \Theta_{\text{Trk}} < 40^\circ$
distance to vertex	$\text{dca}' < 5\,\text{cm}$
radius of start hit	$R_0 < 50\,\text{cm}$

Table 4.1: Selection cuts for tracks in the H1OO analysis framework (H1PartSelTracks, release 3.0.13).

in order to perform an accurate track fit. The selection cuts for the different tracks are listed in table 4.1.
In the H1OO analysis framework these tracks are called H1PARTSELTRACKS [H107b].

4.2 Muon Identification

Muons (up to energies of a few hundred GeV) lose energy predominantly through ionisation and are minimum ionising particles (MIP). The average energy loss amounts $dE/dx \approx 0.01\,\text{GeV/cm}$ in the calorimeter and 90 MeV per layer of the muon detector (each 7.5 cm of iron). The energy loss via Bremsstrahlung is heavily suppressed with respect to electrons, because the cross section for Bremsstrahlung drops with the square of the particle mass

$$\sigma \sim 1/m^2 \Rightarrow \sigma_\mu/\sigma_e \approx 0.23 \cdot 10^{-4}. \tag{4.1}$$

The information to identify muons in H1 is gathered from three different subsystems of the detector: the tracking system, the main calorimeter (LAr) and the muon detectors.
Muons in the H1 detector are identified primarily by reconstructed tracks in the central muon detector (CMD). The purity of the muon identification in the muon

detector is very good, since only few hadrons are able to reach the CMD and are thus wrongly identified as muons. The main drawback of the identification in the instrumented iron is that muons need to have a rather large momentum of $P_\mu \sim 1.5\,\mathrm{GeV}$ to reach the muon detector in order to reconstruct an track in the CMD. The majority of muons coming from the decay of J/Ψ mesons have lower momenta. An additional identification algorithm, based on information closer to the interaction point is desirable.

Due to the high granularity of the LAr calorimeter MIPs can be identified via their uniform energy deposition within a narrow cone. To reach the LAr calorimeter the tracks need to have a minimal transverse momentum of only 800 MeV. Combining both methods the muon identification efficiency reaches 85–90% in the central region of the detector for a track momentum of 1 GeV. Above $P_{\mathrm{Trk}} = 2\,\mathrm{GeV}$ the efficiency is well above 90 %.

In the following the identification and the assignment of qualities will be described, and the lepton identification efficiencies are determined.

Muons in the Instrumented Iron

The iron return yoke of the superconducting coil is instrumented with limited streamer tubes in order to act as central muon detector (CMD). Depending on the polar angle Θ, up to nine hadronic interaction lengths λ_0 are installed in front of the CMD. A large fraction of these hadronic interaction lengths is located in the LAr calorimeter $(5 - 8\,\lambda_0)$, but also the super conducting coil and the cryostats contribute significantly to this number $(0.5 - 1\,\lambda_0)$.

Hence the purity of the muon identification is expected to be quite high in the muon detector. However, for three reasons some hadrons can be wrongly identified as muons:

- **'sail through':** Hadrons have a certain probability to pass matter as minimum ionising particles. The probability depends on the hadronic interaction length λ_0 and the distance d

  $$P \propto \exp\left(-\frac{d}{\lambda_0}\right). \tag{4.2}$$

  Perpendicular to the beam axis ~1 % of the hadrons pass the calorimeter without strong interactions.

- **'punch through':** Some high energetic hadrons cannot be stopped within the length of the calorimeter, although they produce a shower. These hadrons deposit energy in the limited streamer tubes of the muon system, which might be wrongly identified as muon tracks.

- **'inflight decay':** Some frequently produced hadrons have decay channels involving muons, e.g.

$$\pi^{\pm} \rightarrow \mu^{\pm} \overset{(-)}{\nu}_{\mu} \quad (\mathcal{BR} \sim 100\%,\ c\tau \approx 7.8\,\mathrm{m}) \text{ or} \tag{4.3}$$

$$K^{\pm} \rightarrow \mu^{\pm} \overset{(-)}{\nu}_{\mu} \quad (\mathcal{BR} \sim 64\%,\ c\tau \approx 3.7\,\mathrm{m}). \tag{4.4}$$

  If one of these hadron decays inside the detector, the decay muon might be misidentified as muon originating from the interaction point.

The fraction of wrongly identified hadrons due to these processes amounts to a few percent in total. At the backward end of the LAr calorimeter ($140^\circ < \Theta < 160^\circ$) this fraction increases to 10 %. In this angular range the calorimeter (BBE) is instrumented with less than two hadronic interaction lengths λ_0 in front of the muon detector.

In order to identify iron muon candidates in the CMD, a track fit to all hits in the CMD is performed by the H1 reconstruction software H1Rec. The resulting CMD tracks are subsequently used to search for geometrical coincidences with an inner track in the tracking detector, provided that the CMD tracks fulfil certain quality criteria, which are summarised in table 4.2.
The CMD track needs to have hits in at least three out of the 16 layers of the muon detector. The first hit has to be in one of the innermost five layers. The distance of the extrapolated CMD track to the event vertex at the point of closest approach (dca′) has to be less than one meter in cylindrical coordinates (ρ_0, z_0). This cut is very loose, since the accuracy, in particular for the Θ measurement, is very poor in the muon detector.
In order to reduce the rate of wrongly identified hadrons, this analysis requires a cut on the distance between the first and the last of the hit layers (D_{Lay}). All CMD tracks need to have a distance of at least four layers between the first and the last layer. In the backward endcap of the muon detector (BEC, $130^\circ\Theta < 175^\circ$) the required distance between the first and the last layer is increased to five layers. Increasing the distance between the layers D_{Lay}, instead of the number of layers itself increases the purity, but keeps the impact of the single iron layer efficiency constant.

To probe the geometrical coincidence, H1Rec performs track links between preselected inner tracks and the CMD tracks.
To ensure that the inner tracks can reach the central muon detector, the curvature κ of the tracks is restricted to

$$|\kappa| \leqslant \frac{0.003\,\mathrm{cm}^{-1}}{\sin(\Theta_{\mathrm{Trk}})}, \tag{4.5}$$

where Θ_{Trk} denotes the polar angle of the inner track. This corresponds to a cut on the transverse momentum of the track of $P_{T,\mathrm{Trk}} > \sin(\Theta_{\mathrm{Trk}}) \cdot 1.16\,\mathrm{GeV}$.

H1 Iron Tracks	
cylindrical coordinates at dca′	$z_0 \leqslant 100\,\mathrm{cm}$ $\rho_0 \leqslant 100\,\mathrm{cm}$
number of layers	$N \geqslant 3$
number of first layer	$N_{\mathrm{Lay0}} \leqslant 5$
number of last layer	$N_{\mathrm{Lay1}} \geqslant 2$
link probability	$P_{\mathrm{link}} \geqslant 10^{-4}$
Selected Iron Tracks	
distance between layers	$D_{\mathrm{Lay}} \geqslant 4$ ($\geqslant 5$ BEC)
link probability	$P_{\mathrm{link}} > 5 \cdot 10^{-3}$

Table 4.2: Selection cuts for iron muon tracks in the CMD of the H1 analysis software (top) and additional cuts used in this analysis (bottom). Stronger cuts for muons in the backward endcap (BEC) are applied.

In addition, inner tracks and CMD tracks have to match roughly in the polar angle Θ and the azimuthal angle Φ. The angular matching is checked by a comparison of the angles of the track measured in the tracking detector (Θ_{Trk}, Φ_{Trk}) and the angles obtained by a straight line from the event vertex to the first hit in the muon detector ($\Theta_{\mathrm{CMD}}, \Phi_{\mathrm{CMD}}$). The angular ranges of the preselected inner tracks are limited to

$$|\Theta_{\mathrm{Trk}} - \Theta_{\mathrm{CMD}}| < 0.25\,\mathrm{rad} \tag{4.6}$$

$$-\frac{\pi}{2} < q \cdot \sin\left(\Phi_{\mathrm{CMD}} - \Phi_{\mathrm{Trk}}\right) < 0.2, \tag{4.7}$$

where q denotes the charge of the inner track. The allowed azimuthal angular range is asymmetric in order to account for curved tracks in the Φ plane due to the magnetic field.

All preselected inner tracks are extrapolated from the tracking system to the muon detector taking into account multiple scattering and energy losses on its way through the detector (assuming the particle to be a muon). Afterwards the compatibility of each inner and outer track pair is tested by calculating a χ^2 value depending on the momentum of the tracks, the polar angles Θ, the azimuthal angles Φ and the first derivatives of these two angles, Θ' and Φ'. The azimuthal slope of the track Φ' is the most decisive quantity in this calculation. Integrating χ^2 yields the linking probability $P(\chi^2)$, which is asked to be at least $P(\chi^2) \geqslant 5 \cdot 10^{-3}$ for iron muon candidates in this analysis.

Muons in the Liquid Argon Calorimeter

As mentioned before muons are minimum ionising particles (MIP) and do not produce showers in the calorimeter. MIPs have a very distinct signature of energy

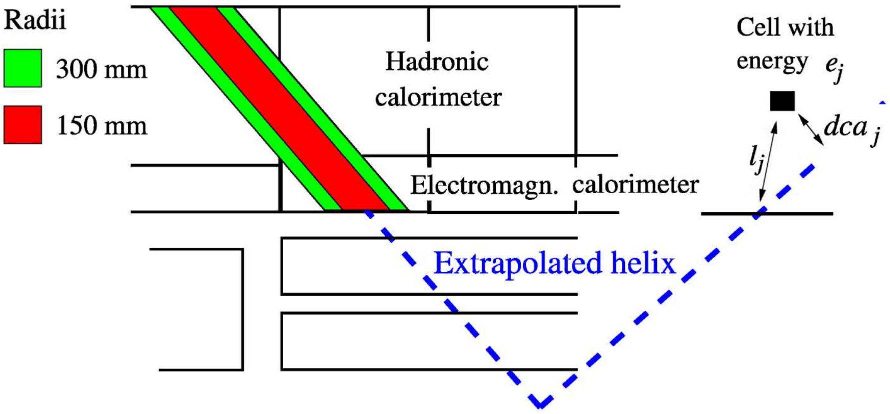

Figure 4.1: Illustration of the cylinders around the extrapolated track, used for the definition of discriminators in the lepton identification.

deposition in the calorimeter. They lose a part of their energy steadily in a long and narrow cone around the particles trajectory, while electrons or hadrons produce broad showers and lose all their energy in the calorimeter. The high granularity of the LAr calorimeter (~45.000 cells) makes it possible to use this signature to identify muons. The identification starts at quite low momenta ($P_{T,\mathrm{Trk}} > 0.8\,\mathrm{GeV}$) and complements the identification in the muon detectors.

During the H1 event reconstruction, the algorithm KALEP looks for signatures of minimum ionising particles in the LAr calorimeter. The KALEP algorithm always starts with a track in the tracking detectors. This track is extrapolated as a helix into the calorimeter, where four discriminators are calculated. As illustrated in figure 4.1, calorimeter cells in two cylinders with axis centered on the extrapolated track are taken into account for this calculation. The inner cylinder has a radius of $\mathrm{r_a} = 15\,\mathrm{cm}$. Usually the whole energy deposition of minimum ionising particles is contained in this volume. A second cylinder is defined with a radius of $\mathrm{r_b} = 30\,\mathrm{cm}$, corresponding to a volume which contains 90 % of the energy of a hadronic shower. In order to suppress noise, only those calorimeter cells with an energy of at least 10 MeV are used to calculate the four discriminator variables [Kas07]:

- $\mathbf{E_{em}(r_a)}$**:** The summed energy of the cells in the electromagnetic part of the calorimeter inside the inner cylinder around the extrapolated track with radius $\mathrm{r_a} = 15\,\mathrm{cm}$.

- $\mathbf{E_{tot}(r_b)}$**:** The total energy of all cells in the calorimeter inside the outer cylinder around the extrapolated track with radius $\mathrm{r_b} = 30\,\mathrm{cm}$.

- $\mathbf{L_{max}(r_a)}$**:** Distance from the beginning of the calorimeter to the very last assigned cell (l_j in figure 4.1) inside the inner cylinder with radius $\mathrm{r_a} = 15\,\mathrm{cm}$.

- **$\mathbf{L_{had}(r_a)}$:** Summed distances l_j to all assigned cells in the hadronic part of the calorimeter inside the inner cylinder with radius $\mathrm{r_a} = 15\,\mathrm{cm}$.

The cell energies used here are taken at the electromagnetic scale, with corrections for dead material in front of the calorimeter, but without corrections for the lower energy response of hadronic showers. The radii $\mathrm{r_a}$ and $\mathrm{r_b}$ are not sharp but smeared out with a sigmoidal function.

After calculating the discriminators, a muon quality is assigned to each track. The calorimeter muon quality goes from $\mathrm{Qual}_\mu = 0$ (no calorimeter muon) to $\mathrm{Qual}_\mu = 3$ (good calorimeter muon). It depends on the distinctness of the muon signature with respect to that of the hadrons.
For each of the four discriminators expected boundaries for muon signatures were determined [NSS97]. These boundaries depend strongly on the polar angle Θ_{Trk} and the transverse momentum $\mathrm{P_{T,Trk}}$ of the track. In order to be insensitive to errors in the track reconstruction, no cut on a particular discriminator is applied. Instead a combined quantity D is calculated, which corresponds to the sum of the deviations from the boundaries

$$D = \min\left(\sum_i \left(\frac{\mathrm{d_i^{low}}}{\mathrm{N_i}}\right)^2 + \sum_i \frac{\mathrm{d_i^{up}}}{\mathrm{N_i}}, 1\right), \tag{4.8}$$

where $\mathrm{d_i^{up}}$ and $\mathrm{d_i^{low}}$ denote the deviation of a discriminator from the upper or lower boundary respectively. The deviations from the lower boundary enter this sum quadratically. The relevance of each discriminator is taken into account by the weighting factors $\mathrm{N_i}$. The muon quality is derived by a cut on this combined quantity D. The probability to wrongly identify hadrons as muons is of the order of $5\,\%$ for $\mathrm{Qual}_\mu = 2$ and decreases to $2\,\%$ for $\mathrm{Qual}_\mu = 3$ [Ste05].

If a track link (as described in section 4.2) between an inner track and an outer muon track exists, an iron quality of 10 is added to the calorimeter muon quality.

Muon Reconstruction Efficiency

To obtain a production cross section the measured number of signal events is normalized to the integrated luminosity and corrected for the efficiency of the event selection. Monte Carlo samples are used to describe the efficiencies and to extrapolate into regions with small or no acceptance. A good agreement between the data and the Monte Carlo simulation is essential.
In the following the muon reconstruction efficiency is determined using a sample of elastic J/Ψ mesons, which is available with large statistics. The results from this large data sample with high purity are used to tune the Monte Carlo simulation and the tuned Monte Carlo simulation is then used for the extraction of efficiencies.

elastic J/Ψ selection cuts
$\|Z_{\mathrm{Vtx}}\| < 35\,\mathrm{cm}$
$N_{\mathrm{Trk}} = 2$ (3, if $Q^2 \geqslant 0\,\mathrm{GeV}^2$)
$P_{\perp,\mathrm{Trk}} \geqslant 0.8\,\mathrm{GeV}$
$20^\circ < \Theta_\mu < 160^\circ \quad \vee \quad 20^\circ < \Theta_e < 150^\circ$
one identified lepton: $\mathrm{Qual}_\mu \geqslant 2 \quad \vee \quad \mathrm{Qual}_e = 3$
no cosmic track candidate

Table 4.3: Selection cuts for the elastic J/Ψ mesons.

The selected elastic J/Ψ meson events are required to have exactly two (vertex fitted) tracks with opposite charge. In case of electroproduction, a third track, coming from the scattered beam lepton is allowed. The transverse momenta $P_{T,\mathrm{Trk}}$ of both tracks has to be larger than 0.8 GeV. One of the two decay tracks needs to have a good or medium calorimeter quality ($\mathrm{Qual}_\mu \geqslant 2$) or has to pass the selection cuts for CMD tracks in the muon detector (cf. tab. 4.2). After these cuts, the remaining non resonant background is dominated by cosmic ray muons ('cosmics'). To reduce contributions from cosmics, three cuts are introduced:

- **back-to-back topology:** Cosmic ray muons which pass the tracking detector produce two tracks with apparently opposite charge. Since these tracks originate from the same particle they have a back-to-back topology. A straight line fit to both tracks is performed and the event is discarded if the χ^2 value of this fit is below 10.

- **distance to vertex:** In contrast to ep interactions, tracks from cosmics generally do not point to the interaction region. This leads to rather large distances of closest approach (dca) with respect to the vertex for these tracks. If both decay tracks of the J/Ψ meson have a dca of more than $0.1\,\mathrm{cm}$ the event is rejected.

- **track timing:** The CJCs provide timing information for each track in an event. Tracks coming from ep collisions have a similar track timing t_0 and the difference $|\Delta t_0|$ should be close to zero. In the case of cosmic ray muons the first track (in the upper hemisphere) is produced before the second track (in the lower hemisphere). Events are not selected, if the timing difference between the two decay tracks is larger than 12 ticks ($|\Delta t_0| \geqslant 12\,\mathrm{ticks} \overset{\triangle}{=} 2.3\,\mathrm{ns}$).

The selection cuts to select events with elastically produced J/Ψ mesons are summarized in table 4.3. In Figure 4.2(a) the invariant mass distribution of the elastic J/Ψ candidates decaying into muons is shown. To further reduce contributions from the non resonant background, only events in the mass window $2.95 < m_{J/\Psi} < 3.25\,\mathrm{GeV}$

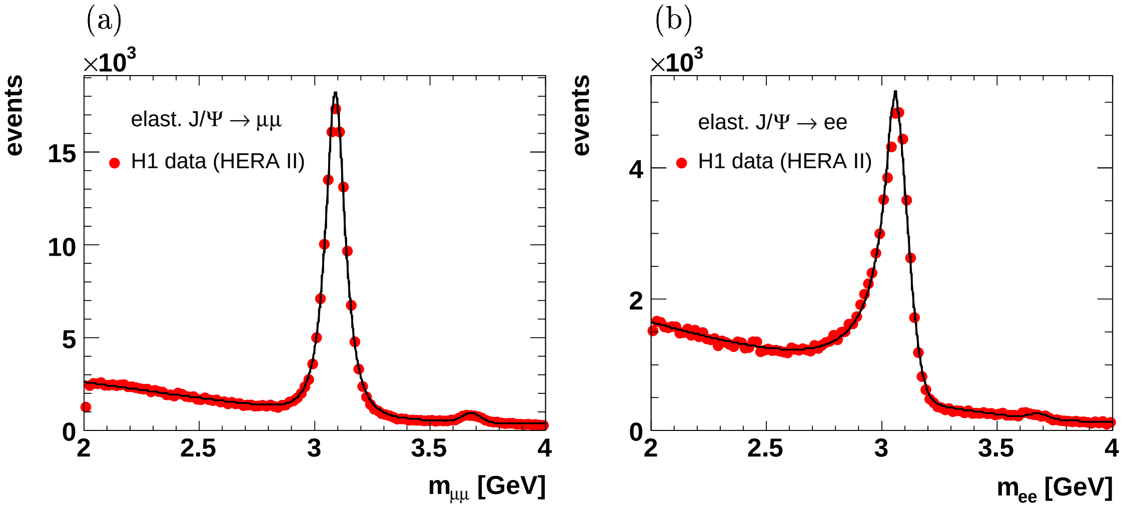

Figure 4.2: Invariant mass distributions of two oppositely charged (a) muons and (b) electrons after applying the selection cuts listed in table 4.3.

are used in the following.

In order to suppress background, events are used in which at least one muon is identified. The muon reconstruction efficiency is then determined by probing the other track from the J/Ψ meson for its lepton signature in the detector. The reconstruction efficiency is given the fraction of events, in which the second track is identified as muon as well. This method is applicable for both, data and Monte Carlo simulation, in the same way.
As the analysis shows, the efficiency is not constant over the whole HERA II running, but changes with the different running periods. In figure 4.3(a) the efficiency to reconstruct muons in the LAr calorimeter is plotted as function of the polar angle of the muon Θ_μ for the years 2004,2005,2006 and 2007. In particular in the 2004 e^+ data sample (dashed line) the calorimeter reconstruction efficiency in the backward region is lower with respect to the samples from subsequent running periods (e.g. 2006/2007 e^+, solid line). In the context of this thesis, the muon reconstruction efficiency was studied in detail for the different running periods and the efficiencies were determined separately for the identification in the calorimeter and in the central muon detector. Here, the running period 2006/2007 e^+ is presented in detail.

The reconstruction efficiency of muons in the H1 detector varies as a function of the momentum P_{Trk} and the polar angle Θ_{Trk} of the track. These variables are used to correct the muon reconstruction efficiency in the Monte Carlo simulation. Reweighting factors are obtained by fitting the efficiency distributions of the data (solid line in fig. 4.3(b)) and of the Monte Carlo simulation (dashed line in fig. 4.3(b)) in each bin and dividing the two resulting functions. This way, the impact of statistical fluctuations in the data is minimized.

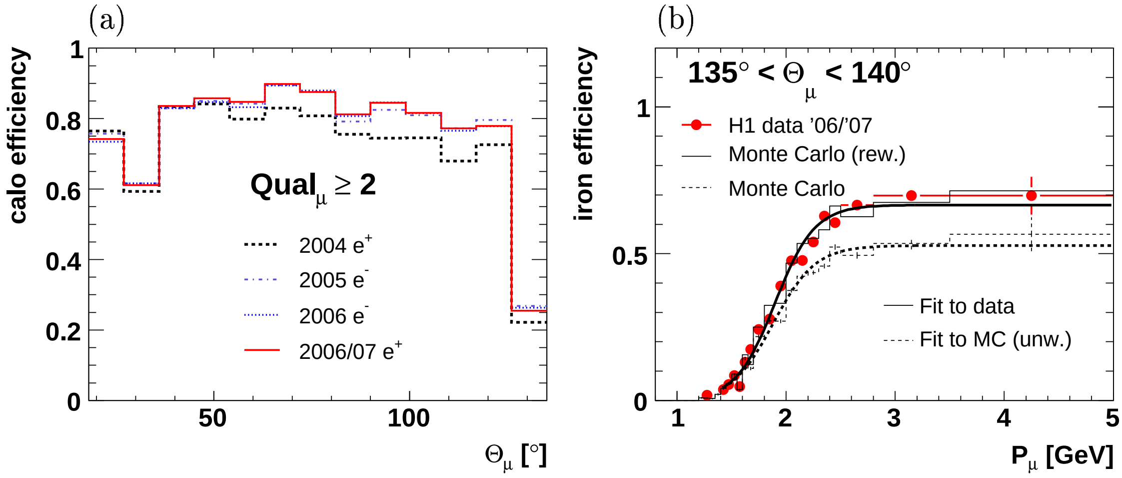

Figure 4.3: (a) Reconstruction efficiency for muons in the LAr calorimeter for the different running periods of HERA II as a function of the polar angle Θ_μ. (b) Exemplary fit for the determination of reweighting factors.

In figure 4.4 the efficiency to identify muons in the central muon detector is shown as a function of the momentum of the track P_{Trk} in four bins of the polar angle Θ_{Trk}. The efficiency in the data is plotted as bullets, the reweighted Monte Carlo simulation is shown as solid line. For comparison the unweighted Monte Carlo simulation is shown as dashed-dotted line. The efficiency in the unweighted Monte Carlo simulation is already close to the efficiency in the data. It is slightly too low in the forward region of the detector (cf. fig. 4.4(a),(b)) and somewhat too high in the backward region (cf. fig. 4.4(c),(d)). Around $P_{\mathrm{Trk}} \approx 2\,\mathrm{GeV}$ the iron muon efficiency shows a steep rise, as the momentum exceeds the threshold necessary to reach the instrumented iron. In the forward region of the detector the LAr calorimeter has more material in front of the instrumented iron and the identification starts at $P_{\mathrm{Trk}} \approx 2.5 - 3\,\mathrm{GeV}$. At 3–3.5 GeV the iron muon reconstruction efficiency levels off at 80 % in the central and backward region of the detector. In front of the backward endcap (BEC) of the central muon detector, only few interaction lengths are installed [H193b]. The efficiency to identify muons in the BEC starts at rather low momenta and reaches the 80 % level already at $P_{\mathrm{Trk}} = 2.5\,\mathrm{GeV}$. At the same time the thinner calorimeter increases the amount of fake muons, because hadrons can reach the BEC. Therefore harder cuts on the iron muon selection are applied in this angular region.

In figure 4.5, the efficiency to identify muons in the LAr calorimeter (with medium or good quality) is shown. It starts at a level of 80 % in the central region). With increasing momentum (fig. 4.5(a) → fig. 4.5(d)) the calorimeter muon efficiency in the barrel reaches ~90 %. The efficiency falls off at $\Theta_{\mathrm{Trk}} \approx 140°$ where the

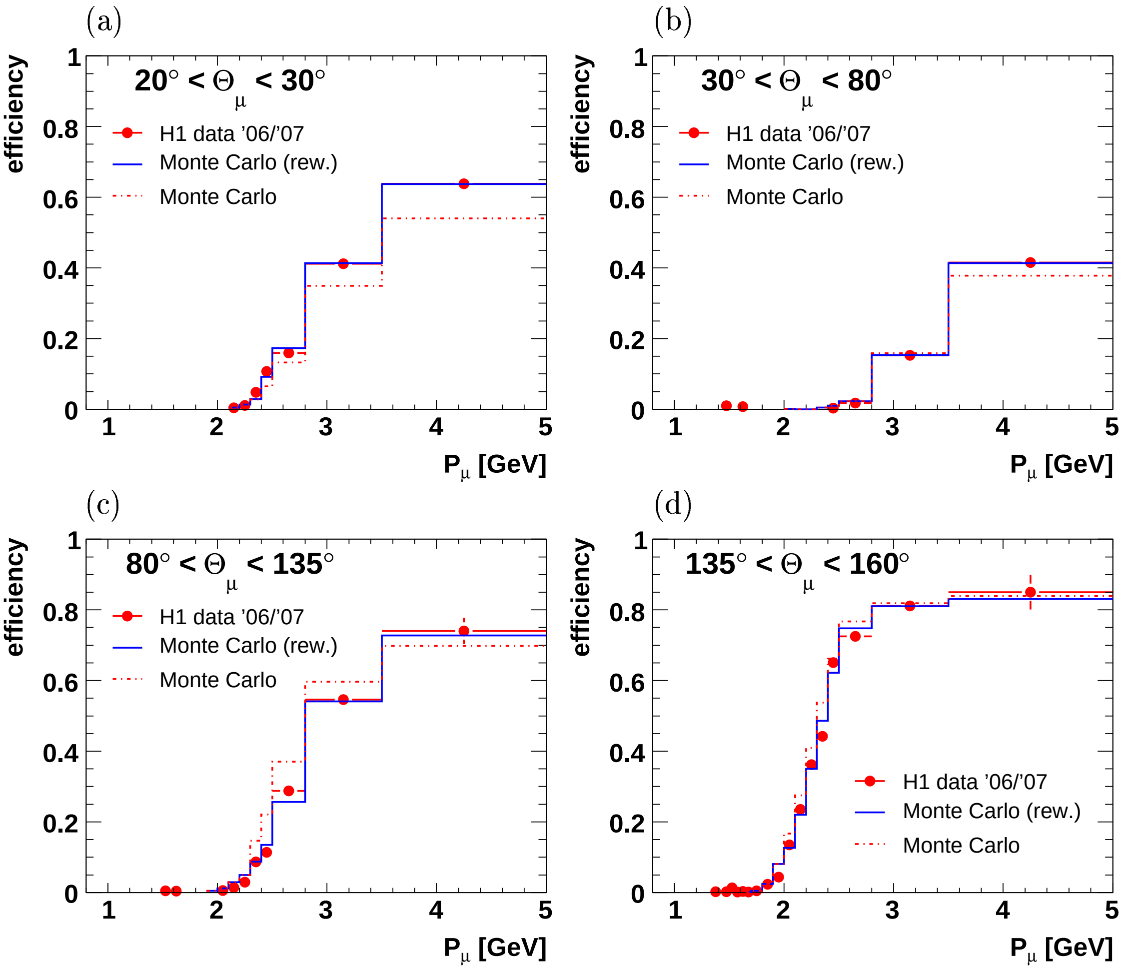

Figure 4.4: Iron muon reconstruction efficiency for the year 2006/2007 (e^+) as a function of the momentum of the tracks P_{Trk} in bins of the polar angle Θ_μ. The efficiency of the data (bullets) is shown in comparison with the reweighted (solid line) and the unweighted Monte Carlo simulation (dashed-dotted line).

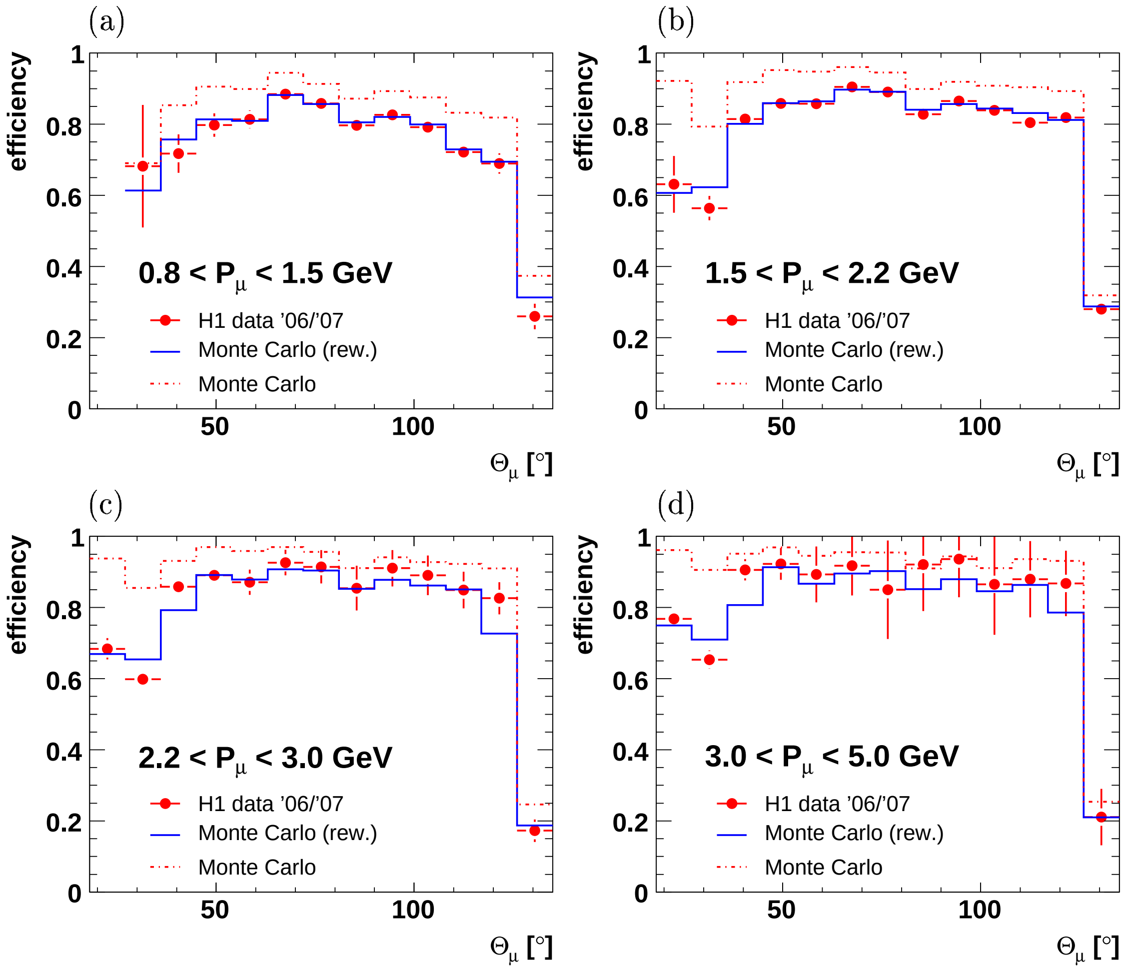

Figure 4.5: Calorimeter muon reconstruction efficiency for the year 2006/2007 (e^+) as a function of the polar angle of the tracks Θ_{Trk} in different momentum bins. The efficiency of the data (bullets) is shown in comparison with the reweighted (solid line) and the unweighted Monte Carlo simulation (dashed-dotted line).

angular range of the LAr calorimeter comes to an end. In this angular range of the calorimeter (BBE) only electromagnetic layers are installed. The radial length of the BBE is not sufficient to identify muons.
The Monte Carlo simulation overestimates the efficiency to identify muons in the calorimeter by 5–10 % in all bins. At large values of the momentum of the track P_{Trk}, the efficiency in the data rises and the difference becomes smaller.
In the forward region of the calorimeter ($20^\circ < \Theta_{Trk} < 40^\circ$) the simulation stays at the same level of efficiency as in the barrel region, while the data points go down by ∼30 %. This discrepancy grows towards larger P_{Trk}.
The Monte Carlo simulation is reweighted in bins of Θ_{Trk} and P_{Trk} as described above. As the figures indicate, the reweighted distribution of the simulation describes that of the data well.

4.3 Electron Identification

In the dense material of the calorimeter electrons deposit their energy in a cascade of electron positron pairs and photons created through bremsstrahlung and pair production processes.
Usually 95 % of an electromagnetic shower are contained in a cylinder with a radius of two times the Moliere radius [PDG08].

The identification of electrons works similar to that of the muons in the calorimeter. The identification starts with tracks in the inner tracking detector. These tracks are extrapolated into the calorimeter and four discriminators are calculated using the cells within two cylinders with radii of $r_a = 15\,\mathrm{cm}$ and $r_b = 30\,\mathrm{cm}$. For the calculations the energy is taken at the electromagnetic energy scale, with corrections for dead material in front of the calorimeter, but without corrections for the lower energy response of hadronic showers. To analyse the reconstruction efficiency of electrons, an elastic J/Ψ meson sample is used. The mass plot of these elastic J/Ψ mesons is shown in figure 4.2(b).

The most powerful discriminator for the electron identification is the ratio E_{em}/P_{Trk}. Here, E_{em} denotes the energy deposition of the particle in the electromagnetic part of the calorimeter. P_{Trk} is the momentum of the particle as measured in the tracking detector. Electrons have a ratio of $E_{em}/P_{Trk} \approx 1$. They deposit their full energy in a compact cluster in the first layers of the calorimeter. Hadrons have lower expected values for E_{em}/P_{Trk}. On the one hand, the energy response hadronic showers in the calorimeter is only ∼70% relative to electromagnetic showers. On the other hand, the hadrons penetrate the calorimeter much deeper and deposit only a fraction of their energy in the electromagnetic part of the calorimeter.
In addition to the E_{em}/P_{Trk} ratio three more discriminators are used:

- **$\mathbf{E_{em}(r_a)}$:** The summed energy of the cells in the electromagnetic part of the calorimeter inside the inner cylinder around the extrapolated track with radius $\mathrm{r_a} = 15\,\mathrm{cm}$.

- $\mathbf{E_{had}(r_b)}$**:** The total energy of all cells in the hadronic part of the calorimeter inside the outer cylinder around the extrapolated track with radius $\mathrm{r_b} = 30\,\mathrm{cm}$.

- $\sum \mathbf{E_{em}} \cdot \mathbf{L_{em}(r_a)}$**:** Sum of the track lengths l_j of the extrapolated track from the beginning of the calorimeter to all assigned cells in the electromagnetic part inside the inner cylinder with radius $\mathrm{r_a} = 15\,\mathrm{cm}$.

Using these discriminators electron qualities from $\mathrm{Qual_e} = 0$ (no electron) to $\mathrm{Qual_e} = 3$ (good electron) are assigned to all tracks in a similar way as described for the muons above.

Electron Reconstruction Efficiency

The reconstruction efficiency for electrons in the LAr calorimeter is determined by a method analogous to that used for the muons. The same two dimensional bins as functions of the momentum of the track $\mathrm{P_{Trk}}$ and the polar angle Θ_{Trk} are used to determine the electron reconstruction efficiency separately for each year. In contrast to the analysis with muons, the quality of the electron tracks is asked to be good ($\mathrm{Qual_e} = 3$) in order to minimizes contributions from misidentified electrons.
The overall electron identification efficiency for the running period 2006/2007 e^+ as a function of the track momentum $\mathrm{P_{Trk}}$ and the polar angle Θ_{Trk} is shown in figure 4.6. The reconstruction efficiency in the uncorrected Monte Carlo simulation is 5–10 % higher with respect to the efficiency in the data. After the two dimensional reweighting as a function of $\mathrm{P_{Trk}}$ and Θ_{Trk}, the efficiency in the data is well modelled by the simulation. In the very backward region of the LAr calorimeter (BBE, $140\,^\circ \lesssim \Theta_{\mathrm{Trk}} \lesssim 154\,^\circ$), only electromagnetic layers are installed. Therefore electrons can be identified up to $\Theta_{\mathrm{Trk}} \approx 150\,^\circ$, while the calorimeter reconstruction efficiency for muons falls off at $\Theta_{\mathrm{Trk}} \approx 140\,^\circ$.

4.4 Systematic Uncertainty

The iron muon reconstruction efficiency and the efficiency to identify muons and electrons in the barrel region of the calorimeter is somewhat overestimated by a few percent in the simulation. The description of the calorimeter muons in the barrel region becomes better at larger values of the track momentum.
As shown in figure 4.5, the uncorrected simulated reconstruction efficiency overshoots that of the data by $\sim$30 % in the forward region ($\Theta_{\mathrm{Trk}} < 40\,^\circ$) for a track momentum of $\mathrm{P_{Trk}} \geqslant 1.5\,\mathrm{GeV}$.

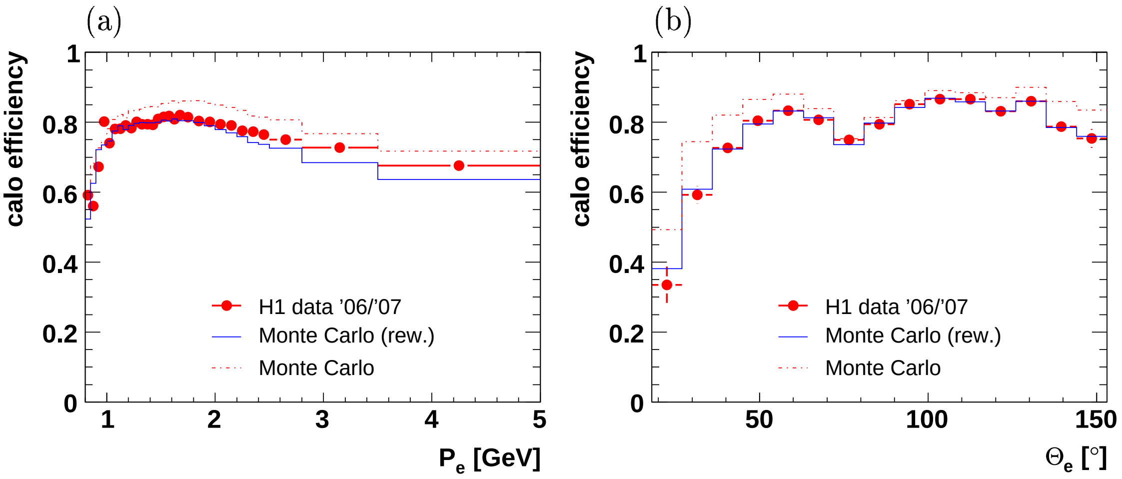

Figure 4.6: Overall electron reconstruction efficiency as a function of (a) the momentum of the track P_{Trk} and (b) the polar angle Θ_{Trk} of the track.

After a two dimensional reweighting, the efficiency in the data is well described by the simulation. Nevertheless, some deviations $\mathcal{O}(5\,\%)$ in the forward and backward region of the calorimeter and at large values of the track momentum P_{Trk} remain. These differences are taken into account as a $5\,\%$ systematic uncertainty on the lepton identification efficiency in the analysis.

CHAPTER 5

Trigger

The main task of the trigger system in the H1 experiment is to select genuine ep events and to separate them from background events. The background mainly arises from interactions of the proton beam with the beam pipe or residual gas and from cosmic ray muons. In H1, a trigger system with four levels (L1–L4) is used in order to reduce the collision rate of 10.4 MHz (96 ns) to an read out rate of the order of $\mathcal{O}(50\,\mathrm{Hz})$. The trigger has to select the interesting events efficiently and with the least deadtime possible.

In the following, the four trigger levels are briefly described and the subtriggers used in this analysis are explained. In the last two sections of this chapter the event yields and trigger efficiencies are presented.

First Trigger Level (L1)

Several subdetectors provide trigger elements at level 1. From combinations of these trigger elements, the central trigger logic builds 128 L1 subtriggers. The first trigger level works without producing deadtime. The data of every bunch crossing is kept available in a pipeline in each subdetector for 2.3 µs ($\hat{=}$ 24 bc), until the L1 trigger decision is worked out. The time for the L1 decision takes into account cable delays of a few hundred nanoseconds and drift times in the CJCs of up to 1 µs.

The typical L1 trigger element rate can be as high as 100 kHz. By combination of trigger elements this rate is reduced by two orders of magnitude to a maximum L2 input rate of about 1 kHz.

If an event is triggered by one of the L1 subtrigger, a L1KEEP signal stops the pipelines and the deadtime of the detector starts.

Second Trigger Level (L2)

The L2 decision is available after 20 µs. Within this time it is possible to analyse the information, which was gathered from the different subsystems, in more detail. Based on tracking chamber information a rough track reconstruction is done. In

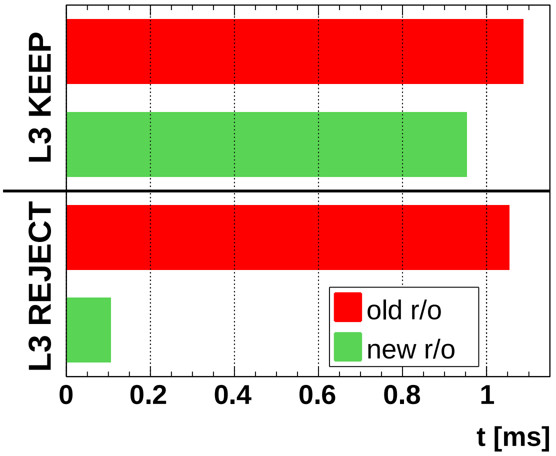

	L3Keep	L3Reject
old r/o	1087 µs	1053 µs
new r/o	953 µs	106 µs

Figure 5.1: Comparison of the 'read out' times for L3Keep and L3Reject decisions for the central muon detector (CMD) using the new and old read out software respectively.

the calorimeter hardware neural networks (L2NN) and topological triggers (L2TT) are used to get 32 L2 conditions. The L2 subtriggers are mainly used to tighten L1 subtriggers that have very large output rates. On L2 the trigger rate is reduced by roughly one order of magnitude in order to reach the maximum input rate for the following trigger level. In Hera I and the beginning of Hera II the third trigger level was inactive and the information was directly delivered to L4. In 2006 the trigger level L3 is activated.

In the case of a L2Keep decision, the read out of the front end electronics starts. A L2Reject decision aborts the detector read out, waits for a front end ready signal (FER) from every subsystem and finally enables the pipelines again.

Third Trigger Level (L3)

A third trigger level (L3) had been foreseen since the first days of H1. It was finally activated in the beginning of 2006 after the shutdown. The L3 trigger is able to handle input rates of up to 200 Hz. The L3 output rate is tuned to about 50 Hz. The L3 trigger decision (L3Keep or L3Reject) is forwarded after 100 µs. During the time available for the L3 decision, FTT tracks and information from other subsystems are used to search for exclusive final states and to verify the L1 and L2 trigger decisions.

In the case of a L3Reject the subdetector read out is aborted immediately. Before 2006 the central muon detector did not comply with the requirements to activate the third trigger level. In the case of a L3Reject decision, the cluster read out continued, but the event data was not copied into the global memory. Thus the readout time in the old readout software in case of a L3Reject decision was only $\sim$30 µs less compared to the read out time after a L3Keep signal (cf. fig./tab. 5.1). In the context of this analysis, the readout software of the CMD was modified such that it fulfilled the time requirements. After the modifications the front end ready signal in case of an L3REJECT was confirmed after only 106 µs. The read out time in the case of an L3KEEP was considerably reduced by ∼130 µs with respect to the former read out time. Since 2006 the CMD was the subsystem in the H1 experiment with the fastest response in case of an L3REJECT and did not produce any exclusive deadtime.

Fourth Trigger Level (L4)

All subsystems deliver their data to the event builder within 1.5 ms, where the components of a particular event are assembled, and the pipelines are again enabled. Afterwards the event is treated offline in an asynchronous event buffer on L4 where it is fully reconstructed. Hence the fourth trigger level does not contribute to the deadtime.

The fourth trigger level works as a filter in order to reduce the amount of data which has to be written to tape. In a first step the trigger decisions of the former levels are confirmed and background events coming from cosmic ray muons or residual gas/beam pipe events are rejected by background filters. For monitoring reasons 10 % of these events are kept. All verified events are fully reconstructed and have to pass a physics selection. During this selection the events are classified by ‘hard scale finders’ (class 4–10) and ‘physics finders’ (class 11–18).

The hard scale finders search for indicators of interesting ep physics. Indicators include tracks or muons with large transverse momentum, missing transverse energy $\mathrm{E}_{\mathrm{T,miss}}$ or a candidate for the scattered beam lepton. The physics finders look for exclusive final states: multi jet events, diffractive events or events involving heavy quarks for example. The relevant class for the analysis of J/Ψ mesons is class 16 (‘hidden heavy flavour’). Events that are neither classified by a hard scale nor a physics finder are classified as class 3 (‘soft physics’). The soft physics events are downscaled by factors of 20 (‘inclusive electron tag’), 40 (‘photoproduction, $\mathrm{y}_{\mathrm{JB}} > 0.9$’) or 60 (‘photoproduction, $\mathrm{y}_{\mathrm{JB}} < 0.9$’).

The L4 selection reduces the rate of events written to tape to roughly 10 Hz. Finally the events are written to POT files (**p**hysics **o**utput **t**ape) and DST files (**d**ata **s**ummary **t**ape). A POT file contains the whole event information (150 kB/evt), a DST file contains a subset of this information (20 kB/evt) which is usually sufficient for physics analysis.

L4 Software Malfunction

The operation of the L4 filter for class 16 (‘hidden heavy flavour’) divides into three phases.

During HERA I and in the beginning of 2004 a physics finder based on tracks that were improved by hits in the silicon tracker (`CSKR`) was used. Phase two started in summer 2004[1] as a new algorithm was installed. It was based on inner tracks

---

[1] run number 387288

reconstructed only with hits in the CJC (`CJKR`). Unfortunately the new algorithm was put into operation in the L4 trigger system in an incomplete way leading to a malfunctioning. This malfunction was unnoticed until easter 2006[2].

Without the `CJKR` tracks, the efficiency of the finder for inelastic J/Ψ meson events was drastically reduced. Due to this malfunction all inelastic J/Ψ mesons in photoproduction were downscaled as 'soft physics' and irrecoverably lost, except for those events with high track momentum muons which were kept by a 'hard scale' finder. J/Ψ mesons in electroproduction are not affected by this malfunction as the electroproduction events were usually classified as 'high Q^2' (class 4) and kept.

Prescale Factors

For some L1 subtriggers, the trigger conditions are not able to reduce the trigger rate to a level that can be tolerated within the available band width. The rate of these subtriggers is thus downscaled by applying so called 'prescale factors'. A prescale factor of n means, that only every n^{th} event of the particular subtrigger is accepted and delivered to L2. The way the prescaling is done, it does not have any impact on the shape of physical quantities.

As explained before, events which are classified as 'soft physics' on L4 are also scaled down. This is done in the same way as the prescaling on trigger level L1. The prescale factors on L4 are called 'L4 weights'.

5.1 Trigger Strategies

The occurrence of J/Ψ mesons in electroproduction events are triggered by a combination of signals in the backward calorimeter (SpaCal) and the central drift chamber using the subtrigger s61

$$\text{L1(s61)} \quad : \quad (\texttt{SPCLe\_IET} > 2 \vee \texttt{SPCLe\_IET\_Cen\_3}) \wedge \texttt{FTT\_mul\_Td} > 0.$$

This trigger is based on the scattered electron signature in the SpaCal. It is independent of the flavour of the leptons from the J/Ψ decay and thus allows to analyse both the muon and the electron decay of the J/Ψ. The veto conditions of the subtriggers are not stated here and can be found in [H198].

In photoproduction the events are triggered by a combination of signals from the central muon detector (CMD) and the central tracking detector (CTD). The two

---

[2] run number 456785

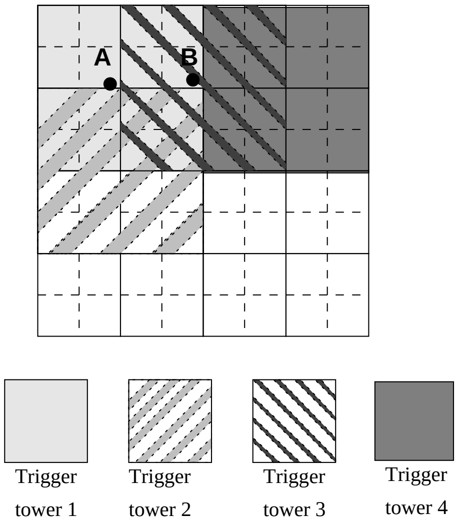

Figure 5.2: Illustration of the 'sliding windows' with 4×4 cells each used in the inclusive electron trigger (`IET`).

complementary muon triggers s19 (CMD barrel) and s23 (CMD endcaps)

$$\begin{aligned}
\mathrm{L1(s19)} &: \texttt{Mu\_Bar} \wedge \texttt{FTT\_mul\_Tc} > \texttt{1} \wedge \texttt{FTT\_mul\_Td} > \texttt{0} \wedge \texttt{CIP\_Sig} > \texttt{1} \\
\mathrm{L1(s23)} &: \texttt{Mu\_ECQ} \wedge \texttt{FTT\_mul\_Tc} > \texttt{2} \wedge \texttt{CIP\_Sig} > \texttt{1}
\end{aligned}$$

$$\begin{aligned}
\mathrm{L2} &: \texttt{FTT\_Tc\_gt\_0} \quad \text{(since 16.11.2006, run number 487167)} \\
\mathrm{L3} &: \texttt{L3\_V17}[\texttt{3}] \qquad \text{(since 08.12.2006, run number 490162)}
\end{aligned}$$

are used to study the photoproduction of J/Ψ mesons. The L2 and L3 conditions are the same for both photoproduction triggers. Since the subtriggers s19 and s23 do not trigger on electrons of a J/Ψ meson, the photoproduction analysis is limited to the muon decay channel.

Trigger Elements

In this section the trigger elements of the electroproduction and photoproduction triggers are briefly explained. The description focuses on the trigger elements used in the analysis. More detailed information can be found in the given references.

Inclusive Electron Trigger (IET)

In the SpaCal trigger [Mey97] the trigger elements can be either 'in time' (ToF) or 'out of time' (AToF). The ToF branch is defined by a time window of about 10 ns width, centered around an expected ep collision. This tight condition makes the ToF branch of the SpaCal trigger insensitive to proton beam induced background signals. The AToF branch is only used for calibration and veto conditions and will not be discussed here.

The SpaCal IET is segmented in arrays of 4×4 cells each in which energies are summed up for the trigger. As illustrated in figure 5.2, these arrays overlap ('sliding windows') to achieve a high efficiency and a localisation in space of the scattered electron already on the first trigger level. In order to obtain the trigger elements (`SPCLe_IET` $>$ 0,1,2), this energy sum is compared to three different thresholds (adjustable from $\sim 100\,\mathrm{MeV}$ to $\sim 20\,\mathrm{GeV}$). In addition, separate L1 trigger elements are calculated for the radius close to the beam pipe ($\mathrm{R} \leqslant 16\,\mathrm{cm}$). These trigger elements are labelled with an additional '`Cen`' in their name.

Muon Trigger Elements

The trigger decision of the muon system is based on five out of the sixteen layers (No. 3,4,5,8 and 12, cf. fig. 3.7 on page 39). The efficiency of the central muon trigger is limited for two reasons. The single layer efficiency of the limited streamer tubes is at most $\epsilon_{\mathrm{lay}} \approx 85\,\%$ and depends mainly on the possible applied high voltage for a module[3]. The second reason is an inefficiency due to the trigger timing. To account for cable delays and drift times of up to 100 ns in the limited streamer tubes, the hits of four bunch crossings are used to reconstruct a track in the CMD.

If the CMD trigger decision were also be based on signals of these four bc, the resulting muon trigger rates would be much too large. Therefore only two bunch crossings are taken into account in the trigger decision. In addition an elaborated system of signal stretching and delay is used in order to set the trigger bit only for the bc which is determined to be the first bc of the muon signal [IKKS95].

The trigger conditions in the CMD depend on the position of a module. For the muon barrel trigger element (`Mu_Bar`) hits in two out of the four innermost trigger layers are required. In the backward inner or outer end cap (`Mu_BIEC, Mu_BOEC`) and in the forward outer end cap (`Mu_FOEC`) three out of the five trigger layers have to provide a hit. In order to reduce the amount of fake signals from high energetic hadrons coming from the proton remnant, four out of the five trigger layers are required in the forward inner end cap (`Mu_FIEC`). In addition to these trigger elements, the coincidence of two trigger signals in

---

[3] During the HERA II running, the high voltage of the central muon detector was raised two times by $+50\,\mathrm{V}$, leading to an increased event yield in the photoproduction analysis.

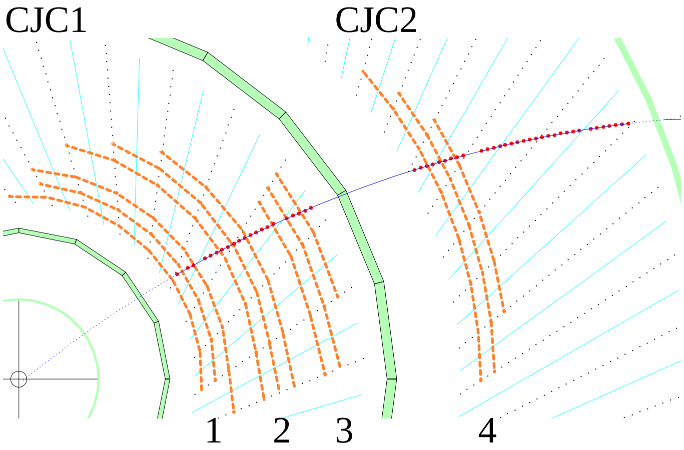

Figure 5.3: Profile of the 4×3 layers (1–4) of CJC1 and CJC2 used for the fast track trigger (FTT).

the forward or backward endcap (`Mu_2_BIoOEC`, `Mu_2_FIoOEC`) results in a positive trigger signal.

The trigger elements for the end caps are summarised in the trigger definition `Mu_ECQ = Mu_BOEC` $\vee$ `Mu_2_BIoOEC` $\vee$ `Mu_FOEC` .

DCrϕ Trigger Elements

In HERA I and up to the year 2004 of HERA II, the ‘drift chamber r-Φ’ (DCrϕ) trigger element was used as track trigger. The DCrϕ trigger uses 10 out of the 56 wire layers of the two CJCs. The information from these wires is digitised in the r-Φ plane. If the distance of closest approach (dca) of the track to the z axis is less than 2 cm, the obtained pattern is compared to 10^4 precalculated masks. The DCrϕ trigger counts positive and negative (`DCRPh_TPos`, `DCRPh_TNeg`) tracks. The tracks are separated into tracks with a transverse momentum $P_{T,Trk}$ of $400 < P_{T,Trk} < 800\,\mathrm{MeV}$ (`DCRPh_TLow`) and with $P_{T,Trk} > 800\,\mathrm{MeV}$ (`DCRPh_THig`).

Fast Track Trigger Elements

In January 2005 the fast track trigger (FTT) replaced the former DCrϕ trigger. The FTT is used on all levels of online trigger decisions (L1-L3). The FTT is based on the hit information of twelve wire layers (4×3) of the central jet chambers (cf. fig. 5.3). Three out of the four FTT layers (1-3) are part of the CJC1, one FTT layer (4) is located in the CJC2. In the following the FTT trigger levels are briefly described. A more detailed description of the FTT and its algorithms can be found in [Ber07, Wis03].

FTT L1: The necessity to reach a L1 trigger decision within 2.3 µs allows only a rather coarse determination of the track curvature ($\kappa \propto 1/\mathrm{P}_{\mathrm{T,Trk}}$) and the azimuthal angle Φ_{Trk}. The track parameters κ and Φ_{Trk} are obtained by a comparison of the measured hit patterns in the FTT layers with precalculated patterns. The trigger decision is based on the number of FTT tracks above a certain $\mathrm{P}_{\mathrm{T,Trk}}$ threshold x (`FTT_mul_T`x). Five thresholds are implemented on L1 (`a` = 100 MeV, `b` = 160 MeV, `c` = 400 MeV, `d` = 900 MeV, `e` = 1800 MeV).

FTT L2: In the case of a L1KEEP decision, a similar (but more accurate) pattern recognition is performed on L2. The resolutions of the resulting track parameters are much better, compared to that of L1. Algorithms in the FTT fitter cards are then used to perform a circular fit to the spatial coordinates of the FTT track segments to determine the vertex position in the r-Φ plane and to do a linear fit in the r-z plane. The results of these fit significantly improve the resolution of the tracks reconstructed on L2.

The momentum and angular information of the FTT L2 tracks is already quite similar to that of the tracks in the final reconstruction ($\sigma(\frac{\Delta_\kappa}{\kappa}) \sim 4\%$, with $\Delta_\kappa = \kappa_{\mathrm{FTT}} - \kappa_{\mathrm{offline}}$, $\sigma_\Phi \sim 3.5\,\mathrm{mrad}$ and $\sigma_\Theta \sim 70\,\mathrm{mrad}$ [Ben07]). The poor resolution in the angle Θ corresponds to a rather large uncertainty on the z position ($\sigma_{\mathrm{z}} \sim 6\,\mathrm{cm}$) of the hits.

Since November 2006 the L2 information is used to validate the L1 decision for the muon triggers s19 and s23. A FTT L2 track with a transverse momentum of more than 417 GeV is required (`FTT_Tc_gt_0`).

FTT L3: The input for the L3 decision of the FTT comes from the FTT L2 tracks and information from other subsystems (e.g. CMD, jet trigger,...). For the subtriggers which are used in this analysis, the third level of the FTT validates the L1 decision of the muon trigger. The L3 trigger element checks whether at least one track points to a triggering module in the central muon detector. Events with more than seven FTT L2 tracks are always kept on L3 and the condition becomes transparent. This muon matching algorithm has an efficiency of almost 100%.

The main effect of the FTT L3 condition on the subtriggers s19 and s23 is a reduction of the average prescales with respect to the period without this condition.

z Vertex Trigger Elements

To reject background events originating far away from the nominal interaction point, a trigger condition that constrains the z position of the vertex is implemented. These events usually come from collisions of the proton beam with residual gas or with the beam pipe. The vertex trigger uses the information of

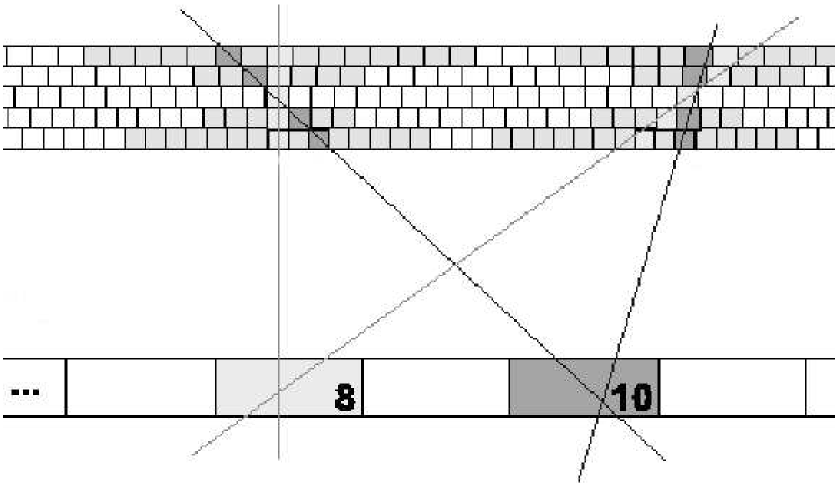

Figure 5.4: Illustration of the CIP to illustrate the principle of the z vertex trigger.

the central inner proportional chamber (CIP) [Urb04]. The CIP is built from five layers of multi wire proportional chambers (MWPC) with ∼8500 readout pads. The signal patterns are used to reconstruct tracks of charged particles within a very large acceptance along the z axis. Extrapolating these tracks to the z axis yields a z vertex distribution (cf. fig. 5.4). The significance $\mathcal{S}$ for the z vertex distribution is calculated using the number of entries in the central ($\mathrm{N}_{\mathrm{cent}}$), the forward ($\mathrm{N}_{\mathrm{fwd}}$) and the backward region ($\mathrm{N}_{\mathrm{bwd}}$) of the z axis according to

$$\mathcal{S} = \frac{\mathrm{N}_{\mathrm{cent}}}{\mathrm{N}_{\mathrm{bwd}} + \mathrm{N}_{\mathrm{fwd}}} \tag{5.1}$$

The z vertex trigger decision (`CIP_Sig`) is based on this significance $\mathcal{S}$. A significance of $\mathcal{S} > 1$ indicates more tracks in the central region than background tracks in the forward or backward region.

5.2 Identification of the Scattered Lepton

The kinematic range of the measurement of electroproduction is restricted to $3.6 \leqslant \mathrm{Q}^2 \leqslant 100\,\mathrm{GeV}^2$ In this range the scattered lepton lies within the angular acceptance of the SpaCal. In the following a description of the selection of scattered leptons in the SpaCal is presented.

A candidate for the scattered lepton in the SpaCal is required to have an energy of at least 8 GeV within a cluster radius of less than 4 cm[4]. If there are several clusters fulfilling these criteria, the cluster with the highest energy deposition in the

---

[4] For trigger reasons, the energy of the scattered lepton in the electroproduction part of this analysis has to be at least 10 GeV (cf. sec. 5.4).

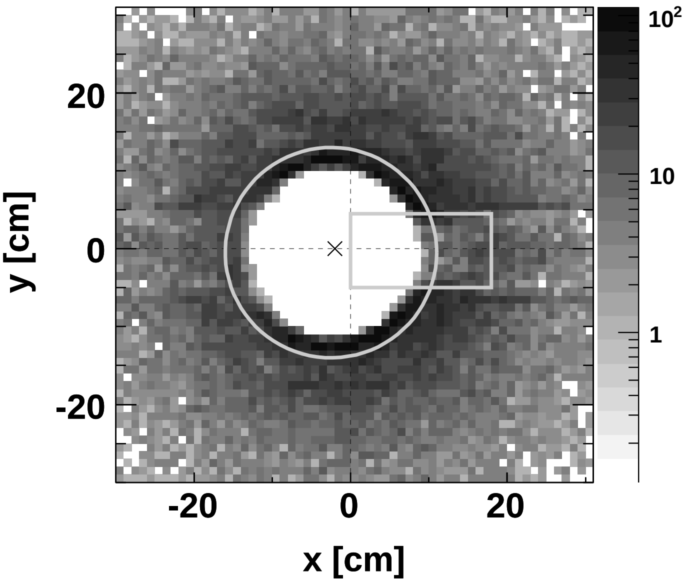

Figure 5.5: Data distribution of the impact position of scattered leptons in the x-y plane of the SpaCal. The radial and box selection cuts applied in the analysis are shown.

event is identified as the scattered lepton. Angular information from the backward proportional chamber (BPC) is used for the reconstruction of the event kinematics if an BPC track exists which matches the SpaCal cluster within a distance of less than 4 cm from its center.

In general the electron beam has a small angle with respect to the z axis of the experiment coordinate system ('beam tilt'). The actual kinematics depend on the angle of the scattered lepton relative to the beam axis (and not the z axis) and the values for the polar and azimuthal angles need to be corrected for the beam tilt.

Towards the inner edge of the SpaCal the energy measurement becomes unreliable. The radial cluster position is required to be larger than 13.5 cm. With this cut clusters close to the edge of the SpaCal are removed in order to ensure that they are fully contained in the SpaCal volume. In figure 5.5 the radial cut is illustrated as grey circle. The box cut in the middle right part of this figure corresponds to a region in which the trigger was inactive. These cells were removed from the trigger in order to reduce background due to synchrotron radiation. Apart from the fiducial cuts in the innermost region some cells in the outer region, which were dead (broken photomultiplier) or which have a very low trigger efficiency (electronics problems), are removed. A detailed analysis of the cells was performed in [Boe07].

Figure 5.6 shows the distributions of the negative four momentum transfer squared Q^2 and the radius of the cluster in the SpaCal. The data are compared to the Cascade Monte Carlo simulation which is used for the cross section determination. After the application of the selection cuts described above, the data seem to be well

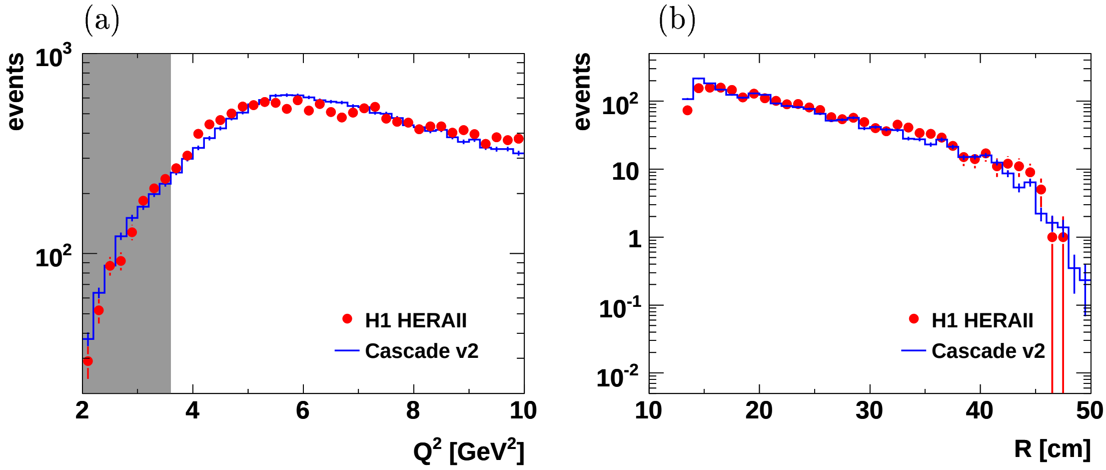

Figure 5.6: Distributions for (a) the four momentum transfer squared Q^2 and (b) the radius of the cluster in the SpaCal. The data (bullets) are compared to the CASCADE Monte Carlo simulation. The grey area in the Q^2 plot is rejected in the selection of the electroproduction analysis.

modelled by the CASCADE simulation.

5.3 Event Yields

During the HERA II running period an integrated luminosity of roughly $\mathcal{L} \sim 365\,\mathrm{pb}^{-1}$ was collected at a center of mass energy of $\sqrt{s} \approx 320\,\mathrm{GeV}$. Figure 5.7 shows the event yields (events/pb^{-1}) for the electroproduction and photoproduction of inelastic J/Ψ mesons after applying all selection cuts which are introduced in chapter 6 of this thesis. The event yield for electroproduction in figure 5.7(a) is flat over the whole HERA II run range with average values of

$$J/\Psi \rightarrow \mu\mu \quad : \quad 2.1\ \mathrm{evt/\,pb}^{-1} \tag{5.2}$$

$$J/\Psi \rightarrow ee \quad : \quad 1.3\ \mathrm{evt/\,pb}^{-1}. \tag{5.3}$$

In contrast, the photoproduction event yield shows four regions (I - IV in figure 5.7(b)) with different average values. These changes are due to a number of problems and modifications in the muon trigger.

From the start of the HERA II data taking until the summer of 2004 (phase I) the event yield in photoproduction was 8.4 events/pb^{-1}. Afterwards it went down to an average yield of 1.3 events/pb^{-1} (phase II) and subsequently increased to an average yield of 3.7 events/pb^{-1} in May 2005 (phase III). Finally on easter 2006 (run number 456785) the average yield increased to 15.1 events/pb^{-1} (phase IV).

At the end of phase I[5] a malfunction in the L4 software occurred as explained

---

[5] run number 387288

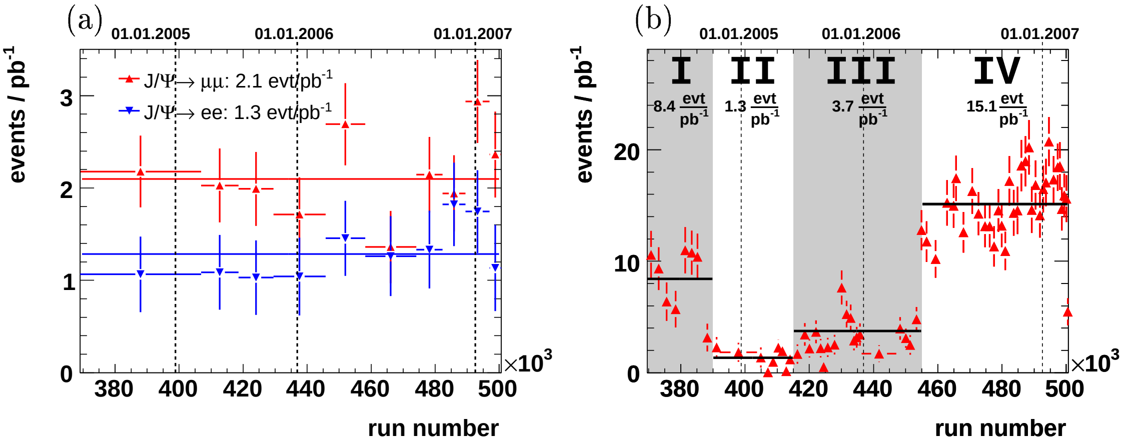

Figure 5.7: Event yields (events/pb^{-1}) for inelastic J/Ψ mesons in (a) electroproduction (s61) and (b) photoproduction (s19 $\vee$ s23).

in section 5. As a result almost all inelastic J/Ψ mesons in photoproduction were rejected during phase II and III. The malfunctioning was spotted around easter 2006[6] and immediately fixed. The rise of the event yield between phase II and III comes from the exchange of a faulty low voltage power supplies in May 2005. The event yield before the L4 malfunction (phase I) is somewhat lower with respect to phase IV. The main reason for this change is that the high voltage of the muon system was raised between phases I and IV, leading to an increase of the hit efficiency, and thus the trigger and muon finding efficiency.
The data of the run range before easter 2006 (phase I–III) cannot be recovered for the photoproduction analysis of inelastic J/Ψ mesons. A rather small possible gain in statistics by including the phases I to III would be disadvantaged by a large systematical uncertainty in the determination of the efficiency of the level 4 trigger.

The electroproduction analysis is not affected by this trigger problem. The selected electroproduction events were classified by a hard scale finder as 'high Q^2' (class 4) on trigger level 4 and were not discarded.

5.4 Trigger Efficiency

For the measurement of the cross sections the trigger efficiency $\epsilon_{\mathrm{Trigger}}$ is determined from data. Independent subtriggers are used to determine the trigger efficiency. The trigger efficiency is defined as the fraction of the monitor sample triggered by the analysis trigger ($\mathrm{T}_{\mathrm{Ana}}$)

$$\epsilon_{\mathrm{Trigger}} = \frac{\mathrm{N}\left(\mathrm{T}_{\mathrm{Mon}} \wedge \mathrm{T}_{\mathrm{Ana}}\right)}{\mathrm{N}\left(\mathrm{T}_{\mathrm{Mon}}\right)}. \tag{5.4}$$

---

[6] run number 456785

J/Ψ mesons in electroproduction with a subsequent decay into muons can be triggered by triggers based on the scattered lepton as well as by muon triggers (s18, s19, s23) or by track triggers (s59, s60). This redundancy is used to determine the trigger efficiencies separately for each trigger element. The efficiency of the SpaCal trigger elements is determined using a combination of these five triggers as monitor. Similarly, the FTT/DCrϕ and muon trigger elements were monitored using subtriggers with only SpaCal trigger elements (s0, s1, s3, s9).

The trigger efficiency for the electroproduction analysis can be determined using the large statistics of the photoproduction data sample.

The DIS sample is used to determine the efficiency of the muon and track trigger elements. These trigger element efficiencies are used to correct the Monte Carlo simulation where necessary. The corrected Monte Carlo is subsequently used to determine the subtrigger efficiency for the photoproduction sample.

Electroproduction

The trigger efficiencies for the electroproduction of J/Ψ mesons are shown in figure 5.8. Overall, the SpaCal `IET` trigger elements are found to be very efficient.

The efficiency of the SpaCal trigger as a function of the energy of the scattered lepton is shown in figure 5.8(a). The efficiency decreases to 75 % at low energies of the scattered lepton ($E_{e'} \leqslant 10\,\mathrm{GeV}$). In addition, the error becomes large at low energies of the scattered lepton since the angular acceptance drops towards low energies of the scattered lepton for lowest values of Q^2. In order to ensure a good trigger efficiency, the energy of the scattered lepton is restricted to be at least 10 GeV in this analysis.

The efficiency of the SpaCal trigger elements as a function of Q^2 is shown in fig. 5.8(b). In the largest bin of the four momentum transfer, the efficiency goes down by three percent, since the angular acceptance of the SpaCal ends at $Q^2 \approx 100\,\mathrm{GeV}^2$.

The tracking conditions in the electroproduction trigger were changed over time. In 2004 the DCrϕ trigger was used and was replaced by the FTT in January 2005. In figure 5.8(c) the trigger efficiency of the tracking conditions is shown separately for both track triggers (FTT: bullets, DCrϕ: triangles). The overall efficiency of the FTT is about 99 %. The efficiency of the DCrϕ trigger is about 5 % lower. At low values of Q^2 the FTT trigger efficiency goes slightly down to 98 %. The trigger efficiency used in the electroproduction analysis is determined by a luminosity weighted combination of the trigger efficiencies of the two track triggers. During 2004 an integrated luminosity of $\sim 25\,\mathrm{pb}^{-1}$ was collected with the DCrϕ trigger. This corresponds to 6.9 % of the integrated luminosity used in the electroproduction analysis.

The overall trigger efficiency of subtrigger s61 is determined to be $\epsilon_{\mathrm{Trigger}} = (97 \pm 2)\,\%$.

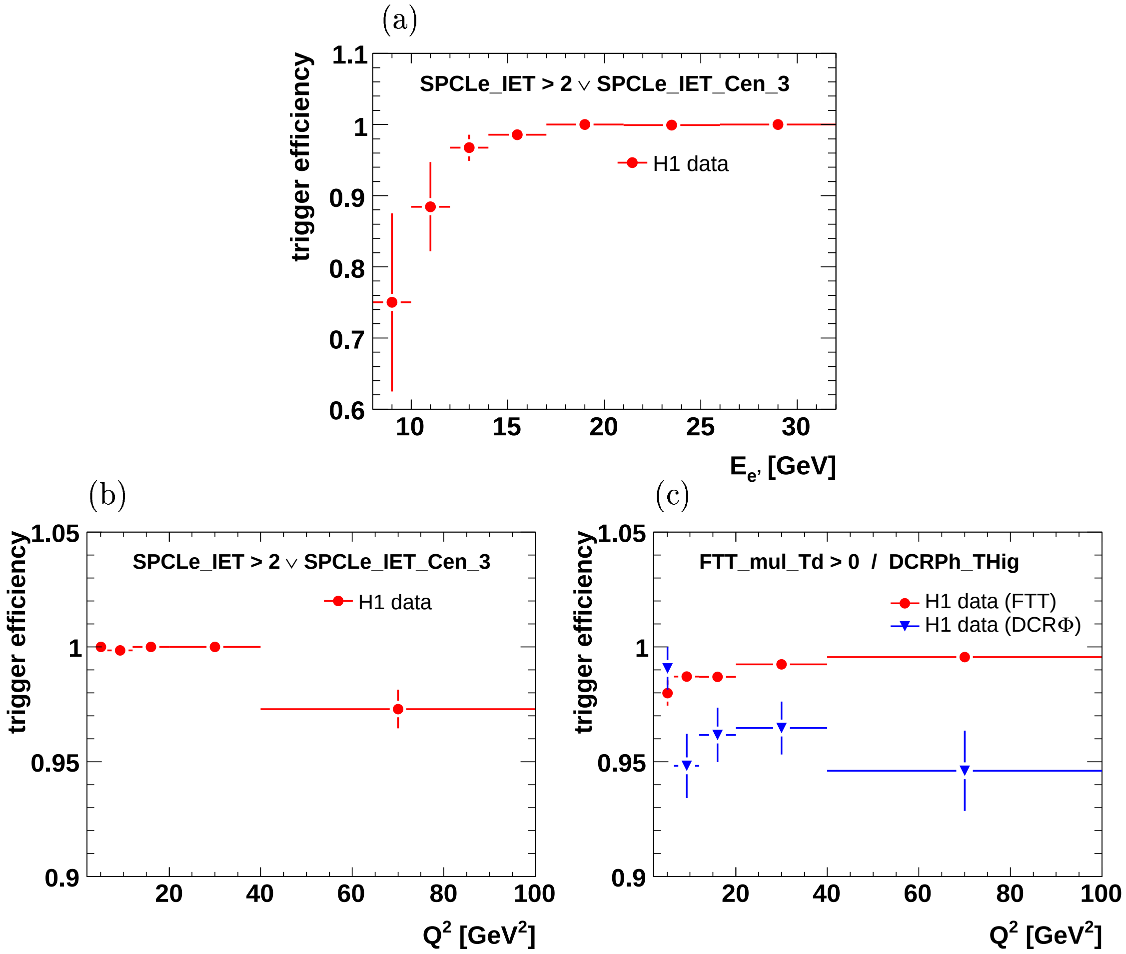

Figure 5.8: Efficiency of the SpaCal trigger elements of the subtrigger s61 used in the electroproduction analysis as a function of (a) the energy of the scattered beam lepton $\mathrm{E_{e'}}$ and (b) the four momentum transfer squared Q^2; (c) efficiency of the track trigger conditions (FTT: bullets, DCrϕ: triangles) of subtrigger s61 as a function of Q^2.

Photoproduction

In figure 5.9 the trigger efficiencies for the L1 photoproduction trigger elements are shown. The bullets correspond to the data, while the solid black line shows the reweighted CASCADE Monte Carlo simulation and the dashed black line the unweighted CASCADE. The photoproduction trigger efficiency is dominated by the efficiency of the muon trigger elements (`Mu_Bar` ∨ `Mu_ECQ`). The simulated trigger efficiency is a few percent too low, in particular at large values of the transverse momentum of the muon (cf. fig. 5.9(a)) and in the barrel region of the detector (cf. fig. 5.9(b)). The efficiency of the muon trigger elements in the Monte Carlo simulation is reweighted in bins of the transverse momentum $\mathrm{P_{T,Trk}}$ and the polar angle Θ_{Trk} of the track. The efficiency of the FTT and the CIP triggers, shown in the figures 5.9(c)–(f), are at a level of 99 %. These L1 trigger elements are very well

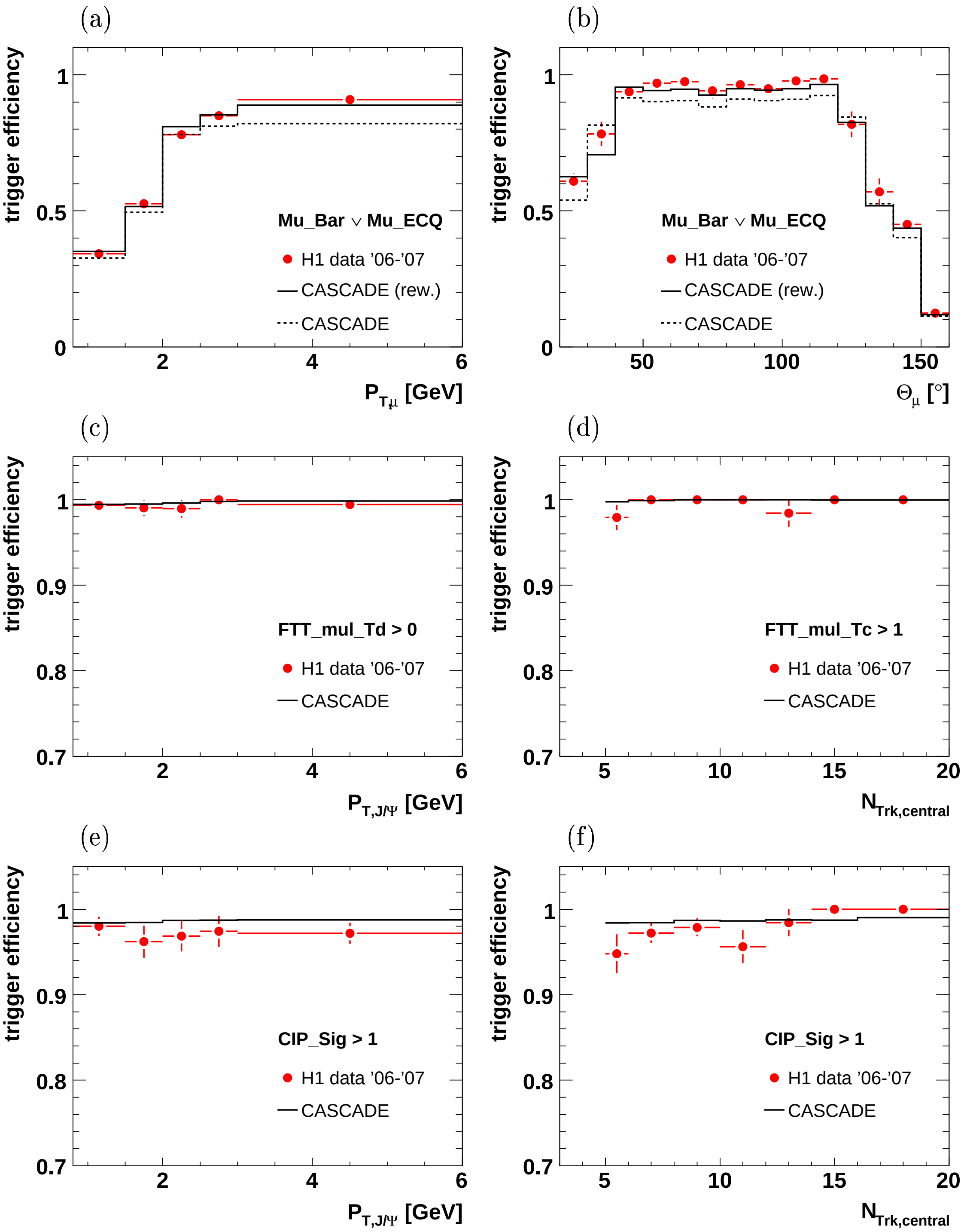

Figure 5.9: Efficiencies of the trigger elements of the photoproduction triggers (s19, s23) as a function of $\mathrm{P}_{\mathrm{T},\Psi}$, Θ_Ψ and the track multiplicity. The data (bullets) are compared to the CASCADE predictions with (solid line) and without (dashed line) reweighting.

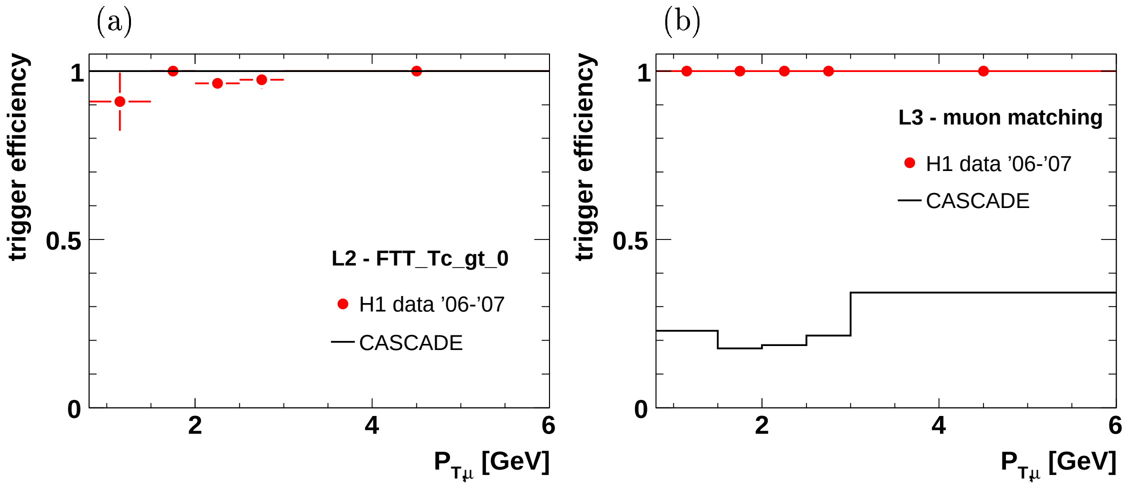

Figure 5.10: Efficiency of the L2 and L3 trigger conditions used in the photoproduction analysis in data (bullets) and CASCADE simulation (solid line). The L3 condition is wrongly simulated and ignored in the determination of the trigger efficiency in this analysis.

described by the simulation and no correction is necessary.

In figure 5.10 the L2 and L3 trigger conditions are plotted as a function of the transverse momentum of the muon. The L2 condition (`FTT_Tc_gt_0`) is well described by the simulation and almost 100 % efficient. The track muon matching condition imposed L3 as validation of the L1 muon trigger elements (`L3_V17[3]`) has an efficiency of 100 % in the data (bullets in fig. 5.10). Since the L3 trigger element of the FTT is not well simulated in the Monte Carlo and is 100 % in data, it is not required in the selection of Monte Carlo events.

5.5 Systematic Uncertainty

In the case of the electroproduction (s61) the trigger efficiency was determined from the data using independent trigger channels. The efficiency is found to be $\epsilon_{\mathrm{Trigger}} = (97 \pm 2)\,\%$. The statistical uncertainty of the trigger efficiency determination is taken as the systematic uncertainty of the electroproduction analysis.

For the photoproduction analysis remaining differences between data and corrected Monte Carlo simulation are below 4 %. The track trigger elements on L1 are very well described with efficiencies of more than 96 %. The uncertainty on the track trigger elements is 2 %. The L2 and L3 conditions are almost 100 % efficient. An uncertainty of 2 % is applied for each of the two trigger levels.
The uncertainties for the particular trigger levels lead to a systematic uncertainty of 5 % for the photoproduction trigger.

CHAPTER 6

Data Selection

In this thesis photo- and electroproduction event samples with inelastic J/Ψ mesons are discussed. The selection is quite similar for both analyses. In the following the data sample, the selection cuts and the cuts for background rejection will be introduced. Subsequently the method for the extraction of the number of signal events will be explained. The selection cuts of the analyses are summarised in table 6.1.

6.1 Data Samples and Preselection

In a first selection step, only runs with good and medium quality are selected. Run ranges with known problems are excluded and a run needs to have at least an integrated luminosity of 0.1 pb^{-1} in order to be selected. To achieve the best precision, all relevant components of the H1 detector must be fully operational. In particular high voltage (HV) must be switched on for the following subsystems:

- Central Jet Chambers (CJC1 & CJC2)
- Central Muon Detector (CMD)
- Luminosity System
- Fast Track Trigger (FTT)
- Liquid Argon Calorimeter (LAr)
- Spaghetti Calorimeter (SpaCal)
- Central Inner Proportional Chamber (CIP)
- Time-of-flight system (ToF)

Only events with a reconstructed position of the primary vertex on the z axis inside the central region of the detector with respect to the nominal interaction point ($-35\,\mathrm{cm} \leqslant z_{\mathrm{Vtx}} \leqslant 35\,\mathrm{cm}$) are selected. Thus background events from non ep collisions, cosmic ray muons or collisions of satellite bunches are suppressed.

6.2 Lepton Selection

Detailed information about lepton identification algorithms and the lepton quality bits can be found in chapter 4 of this thesis.

The J/Ψ meson candidates in this analysis are reconstructed through their leptonic decay into two muons or electrons with a branching ratio of $\mathcal{BR}_{\mu\mu} = (5.93 \pm 0.06)\%$ and $\mathcal{BR}_{ee} = (5.94 \pm 0.06)\%$ respectively [PDG08]. The trigger selection in photoproduction restricts the analysis to the muon channel. The branching ratio of J/Ψ mesons into two leptons fortunately is the largest of all vector mesons. This decay leads to a very clean hadronic final state. Most kinematic quantities can be reconstructed using the two decay lepton tracks, which can be measured very precisely in the central tracking detectors.
Only events with at least two reconstructed muon candidates or two electron candidates, of opposite charge are taken into account. The tracks need to have at least a transverse momentum of 800 MeV in order to be identified in the calorimeter.

Electrons are identified via their energy deposition in the electromagnetic part of the LAr calorimeter. Whereas muon tracks are identified as minimal ionising particles in the LAr calorimeter and as track segments reconstructed in the CMD. Tracks from muon candidates are restricted to polar angles in the range $20° < \Theta_{\mu} < 160°$ while electrons are selected in the range $20° < \Theta_{e} < 150°$. In this range the calorimeter identification is sufficiently controlled. Both decay muons need to have at least a medium quality ($\mathrm{Qual}_{\mu} \geqslant 2$). In the case of the photoproduction analysis one muon is identified in the central muon detector ($\mathrm{Qual}_{\mu} \geqslant 10$) in order to be able to control the trigger efficiency. The purity of the electron identification is lower than to that of the muons and hence the quality of decay electrons is required to be good ($\mathrm{Qual}_{e} = 3$). If the lepton identification requirement were loosened to one identified lepton, the combinatorial background would be too large, in particular in the region of low elasticities z which is dominated by events with high track multiplicities, and thus high combinatorial backgrounds.

6.3 Kinematic Selection

The photo- and electroproduction data samples are kinematically disjoint as the presence of a candidate for the scattered beam lepton separates the two kinematic

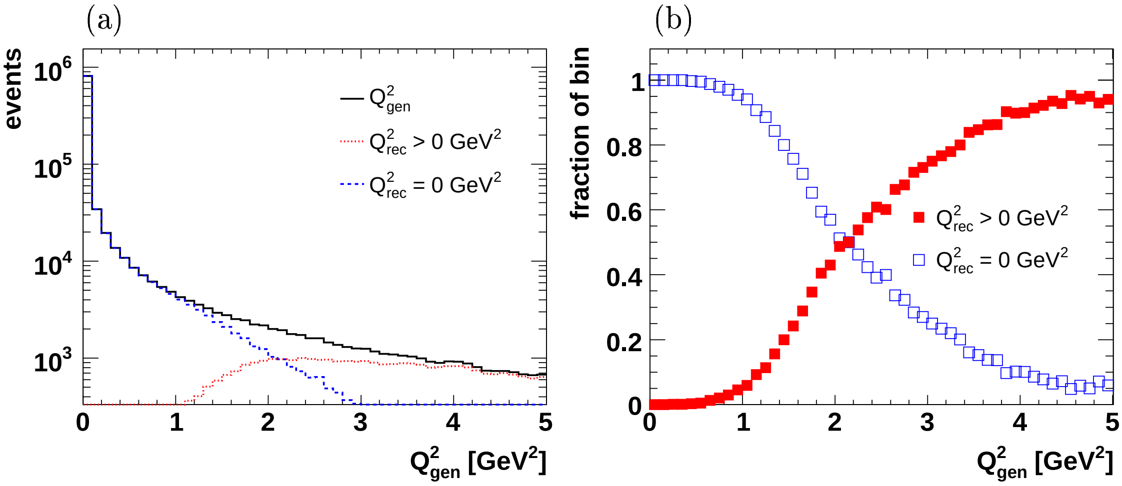

Figure 6.1: (a) Generated (CASCADE) Q^2 distribution with and without detected scattered lepton and (b) the efficiency for finding the scattered lepton as a function of Q^2.

regions of the analyses.

Electroproduction events are selected by the requirement that there has to be an isolated high energetic electromagnetic cluster ($E_{clus} \geqslant 8\,\mathrm{GeV}$) detected into the backward calorimeters (SpaCal) consistent with a signal from the scattered lepton. Demanding a reasonable acceptance and a good agreement between data and Monte Carlo simulation, the range of four momentum transfer squared is restricted to $3.6 \leqslant Q^2 \leqslant 100\,\mathrm{GeV}^2$ (cf. section 5.2). The energy of the scattered lepton $E_{e'}$ is required to be larger than 10 GeV. Below this energy the efficiency of the SpaCal lepton trigger drops (cf. chapter 5).

The upper Q^2 cut denotes the outer radius of the SpaCal. At $Q^2 > 100\,\mathrm{GeV}^2$ the beam lepton is mainly scattered in the LAr calorimeter. In this high Q^2 region no significant J/Ψ signal was found in the data.

Events are identified as photoproduction if there is no candidate for a scattered lepton found in the SpaCal or LAr calorimeter with an energy larger than 8 GeV. The identification efficiency of scattered leptons in the SpaCal is shown in figure 6.1(b). It starts at $Q^2 \approx 1\,\mathrm{GeV}^2$ and reaches the 50% level at $Q^2 \approx 2\,\mathrm{GeV}^2$, restricting the so called untagged photoproduction ($Q^2_{\mathbf{rec}} = 0$ GeV^2) to $Q^2 \lesssim 2$ GeV^2.

The average Q^2 for the photoproduction analysis is $\langle Q^2 \rangle \approx 0.085\,\mathrm{GeV}^2$.

6.4 Background Suppression

In addition to the non resonant background, J/Ψ mesons from other ep processes involving J/Ψ mesons contribute to the inelastic J/Ψ signal sample. Contributions can be either proton dissociative J/Ψ mesons at large values of z ($z > 0.9$) or feed

down from the cascade decay of $\Psi(2S)$ mesons[1]. In the case of diffractive $\Psi(2S)$ the elasticity of the resulting J/Ψ is measured to be $z \approx 0.85$. The diffractive production process has a much higher production cross section compared to the inelastic J/Ψ production.
At low values of the elasticity ($z \leqslant 0.45$) contributions from the decay of B mesons become significant. Contributions from χ_c mesons contribute only at very low elasticities ($z \leqslant 0.3$) and are neglected in this thesis [Kru01].

To reduce contributions from non prompt J/Ψ mesons for the measurement of cross sections of direct inelastic J/Ψ meson production, three cuts were introduced:

- $P^{(*)}_{\perp,\Psi} \geqslant 1\,\mathrm{GeV}$
  A cut on $P^{(*)}_{\perp,\Psi}$ therefore rejects most of the diffractive J/Ψ mesons. The spectrum of the transverse momentum (in the γp rest frame) of diffractive J/Ψ mesons $P^{(*)}_{\perp,\Psi}$ shows a much steeper decline compared to the spectrum of the inelastic production process.

- $0.3 \leqslant z \leqslant 0.9$
  The limited range of the elasticity z reduces contributions from diffractive processes at large values of z and from the decay of B mesons at low values of z. Outside this region towards lower values of z, the track multiplicity and with this the combinatorial background rises strongly.

- $N_{\mathrm{Trk,central}} \geqslant 5$
  In order to reject contributions from the cascade decay of the $\Psi(2S)$ into J/Ψ and two pions (which leads to events with 4 charged particles), selected events must have at least 5 tracks in the central region of the detector.

The remaining contributions from non prompt J/Ψ mesons will be analysed in chapter 7 and 8 of this thesis.

The cuts on the transverse momentum $P^{(*)}_{\perp,\Psi}$ and the elasticity z restrict the kinematic range of this analysis. The cut on the polar angle of the tracks and the acceptance of the detector constrains the center of mass energy of the photon proton rest frame $W_{\gamma p}$ for the electroproduction to $50 \leqslant W_{\gamma p} \leqslant 240\,\mathrm{GeV}$ and for photoproduction to $60 \leqslant W_{\gamma p} \leqslant 225\,\mathrm{GeV}$.

The cut on the track multiplicity is used to reduce diffractive contributions to the inelastic signal sample. The measured cross sections presented in this analysis are extrapolated down to $N_{\mathrm{Trk}} = 2$ (the two decay leptons) using the Monte Carlo simulation.

---

[1] $\Psi(2S) \rightarrow J/\Psi\ \pi^+\pi^-$, $\mathcal{BR} = (32.3 \pm 0.5)\%$ [PDG08]

DIS		γp
$J/\Psi \to ee$	$J/\Psi \to \mu\mu$	$J/\Psi \to \mu\mu$
Kinematic Cuts		
$3.6 \leqslant Q^2 \leqslant 100\,GeV^2$		$Q^2_{\mathbf{rec}} = 0\,GeV^2$
$50 \leqslant W_{\gamma p} \leqslant 225\,GeV$		$60 \leqslant W_{\gamma p} \leqslant 240\,GeV$
$0.3 \leqslant z \leqslant 0.9$		$0.3 \leqslant z \leqslant 0.9$
$P^*_{T,\Psi} \geqslant 1\,GeV$		$P_{T,\Psi} \geqslant 1\,GeV$
Selection Cuts		
$P_{T,Trk} \geqslant 0.8\,GeV$		$P_{T,Trk} \geqslant 0.8\,GeV$
$20^\circ \leqslant \Theta_e \leqslant 150^\circ$	$20^\circ \leqslant \Theta_\mu \leqslant 160^\circ$	$20^\circ \leqslant \Theta_\mu \leqslant 160^\circ$
$Qual_{e,1,2} = 3$	$Qual_{\mu,1,2} \geqslant 2$	$Qual_{\mu,1} \geqslant 10, Qual_{\mu,2} \geqslant 2$
$N_{Trk,Central} \geqslant 5$		$N_{Trk,Central} \geqslant 5$

Table 6.1: Summary of the selection cuts for the electroproduction (DIS) and the photoproduction (γp) analysis.

6.5 Signal Extraction

After applying all selection cuts, still significant contributions from non resonant backgrounds are part of the J/Ψ sample. In these background events one or both lepton tracks are wrongly identified as muon or electron. In the electron decay channel the signal to background ratio is worse due to a lower purity of the electron identification.
The relaxed muon selection criteria in the electroproduction analysis yield also a higher background with respect to the photoproduction analysis. In particular, the background rises with the increasing track multiplicity towards lower values of z (cf. fig. 6.2). To obtain the proper number of signal events for the cross section measurement, a log likelihood fit to the mass distribution in the interval $2 < m_{\ell\ell} < 6$ GeV is applied in each analysis bin.

The signal in the muon samples is fitted by a modified Gaussian function which is of the form [ZEUS05]

$$\mathcal{G}_{mod}(x) \sim \exp\left(-\frac{1}{2} \cdot x^{1+1/(1+0.5\cdot x)}\right), \quad \text{with } x = \left|\frac{m_{\mu\mu} - m_0}{\sigma}\right|. \tag{6.1}$$

This signal shape allows broader non Gaussian tails of the resonant signal around the nominal mass m_0 with a width of σ. This takes into account that the resolution of the J/Ψ mass reconstruction depends on the tracking detectors involved in the track fit. It varies in particular depending on the presence of hits in the few layers of the z chambers.
The signal shape for the decay into electrons cannot be described by a (symmetric) Gaussian because, as expected, it has a long 'radiative tail' down to much lower

reconstructed invariant masses due to QED radiation. The appearance of this tail can be explained by two reasons: On the one hand the radiative decay of J/Ψ mesons ($J/\Psi \to \gamma e^+ e^-$, $\mathcal{BR} = (0.88 \pm 0.14)\%$ [PDG08]) and on the other hand energy losses of the decay electrons due to bremsstrahlung in the tracking detector before they enter the calorimeter. Only the tracks are used for the reconstruction of the invariant mass, leading to a long tail on the lower slope of the invariant mass distribution. Therefore the signal in the electron sample is fitted by a Gaussian with an exponential added to the lower slope of the invariant mass distribution

$$\mathcal{G}_{\mathrm{ee}}(\mathrm{m_{ee}}) \sim \frac{\mathrm{N}_{J/\Psi}}{\{\sigma_{J/\Psi} + \mathcal{A}\} \cdot \sqrt{2\pi}} \cdot \mathrm{e}^{-\frac{1}{2} \cdot \left(\frac{\mathrm{m_{ee}} - \mathrm{m}_{J/\Psi}}{\sigma_{J/\Psi} + \mathcal{A}}\right)^2} \tag{6.2}$$

where $\mathcal{A} \sim |\mathrm{m_{ee}} - \mathrm{m}_{J/\Psi}| - (\mathrm{m_{ee}} - \mathrm{m}_{J/\Psi})$ denotes the asymmetry term.
In the fits the background is parametrised by a polynomial of third order with four free parameters. At the nominal mass of the $\Psi(2S)$ ($\mathrm{m}_{\Psi(2S)} = 3686.09 \pm 0.04\,\mathrm{MeV}$ [PDG08]) an additional Gaussian with fixed position and width is allowed.
For both, the electron and the muon sample, the shape of the fit to the signal, its width and position, is fixed to values determined in the overall mass plots. The measured width of the J/Ψ mesons arises only from the detector resolution. It is determined to be $\sigma_{J/\Psi} \approx 50\,\mathrm{MeV}$ The statistical uncertainties of the mass plot in the analysis bins are too large to constrain all free parameters of the signal shape.

Systematic Uncertainty

To obtain a systematic uncertainty for the extraction of the number of signal events, the result from the fit to signal and background is compared to the number of events above the fitted background function. In figure 6.3(a) the relative difference of this comparison is plotted, where '#Count' denotes the number of events above the fitted background and '#Fit' the number of events obtained from the fit. In case of the muon decay channel the observed difference is below 1% (for DIS and γp). For the electron channel the deviation is about 5 %. The uncertainty for the electron sample is larger due to the worse signal to background ratio and the difficulty to describe the radiative tail properly with the low statistics.
Figure 6.3(b) shows the development of this difference as a function of the used mass window for the photoproduction mass peak. In the first few bins the mass window is too narrow whereas the number of counted events is below the number determined by the fit. If the mass window is as big as $2.8 \leqslant \mathrm{M}_{\mu\mu} \leqslant 3.4\,\mathrm{GeV}$ most of the signal peak is included in the comparison. If the used mass window is enlarged further, the statistical fluctuations cancel each other out and the number obtained from the fit and the counted number become almost the same.

An additional uncertainty for the number of signal events arises from the normalisation of the function parametrising the background. To quantify this uncertainty

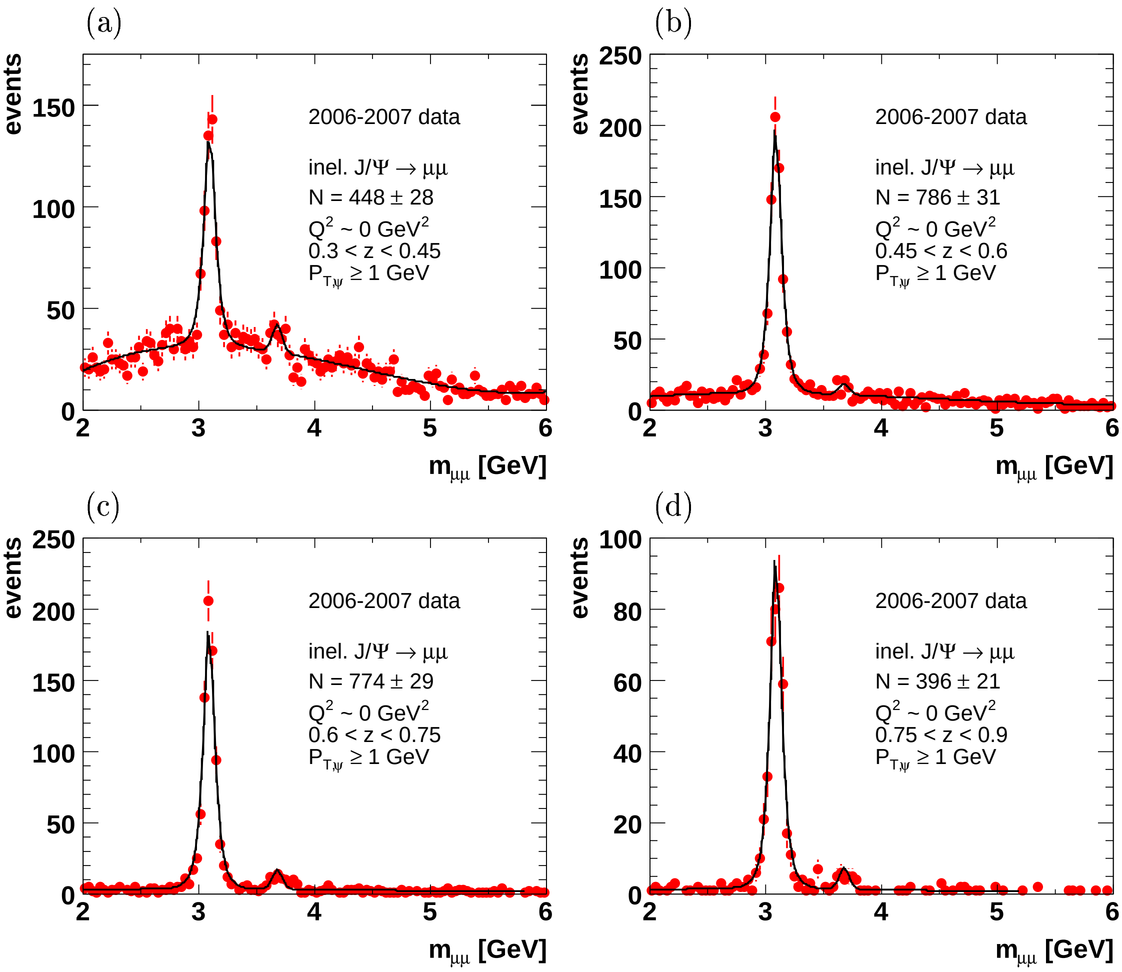

Figure 6.2: Invariant mass distribution of two oppositely charged muons at low and high values of the elasticity z: (a) $0.3 \leqslant z \leqslant 0.45$, (b) $0.45 \leqslant z \leqslant 0.6$, (c) $0.6 \leqslant z \leqslant 0.75$ and (d) $0.75 \leqslant z \leqslant 0.9$

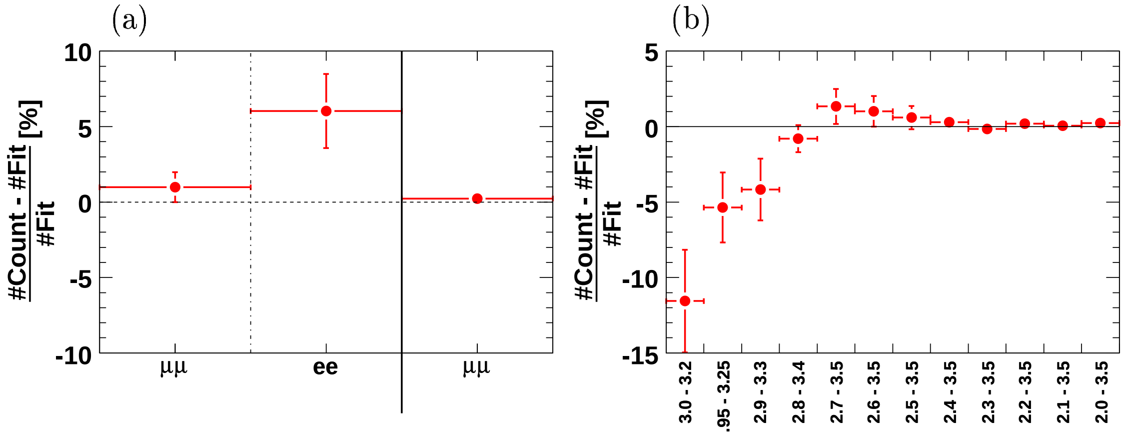

Figure 6.3: Systematic uncertainty arising from the extraction of the number of signal events. (a) comparison of the number of signal events obtained from the fit and the number of events above the fitted background function, (b) development of the comparison for different mass windows for the decay into muons in photoproduction.

the background function was varied up and down, and the impact on the number of signal events in the mass window $2.8 \leqslant M_{\ell\ell} \leqslant 3.4\,\text{GeV}$ was checked.

Altogether this leads to an uncertainty of 2–5% for the decay channel into muons and 6–8% for the decay channel into electrons, increasing with the amount of combinatorial background (i.e. towards lower values of the elasticity z).

Chapter 7

Photoproduction of J/Ψ Mesons

This chapter presents the results of the photoproduction analysis of inelastic J/Ψ mesons. The data sample of the analysis was recorded with the H1 experiment during the years 2006 and 2007 and corresponds to an integrated luminosity of $\mathcal{L} \approx 166\,\mathrm{pb}^{-1}$. The events were triggered by the subtriggers s19 or s23 by a combination of signals from the central muon detector and the central tracker. The J/Ψ mesons are identified via their leptonic decay into two muons. The mass distribution of the 2410 J/Ψ mesons in photoproduction is shown in figure 7.1. The results of this analysis are accepted as 'preliminary' by the H1 collaboration and were presented at the International Workshop on Heavy Quarkonia in 2007 [Ste07].

After a comparison with the Monte Carlo simulation, the results for the differential and double differential cross sections are presented and the sources of systematic uncertainties are explained. At the end of the chapter, the polarisation of the J/Ψ meson is analysed and contributions from higher resonances and the decay of B mesons are studied.

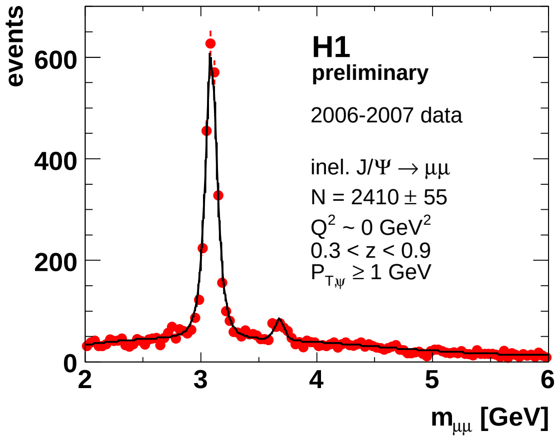

Figure 7.1: Invariant mass distribution of two oppositely charged muons in the kinematic range $Q^2 \approx 0\,\mathrm{GeV}^2$, $50 \leqslant W_{\gamma p} \leqslant 225\,\mathrm{GeV}$, $0.3 \leqslant z \leqslant 0.9$ and $P_{T,\Psi} \geqslant 1\,\mathrm{GeV}$.

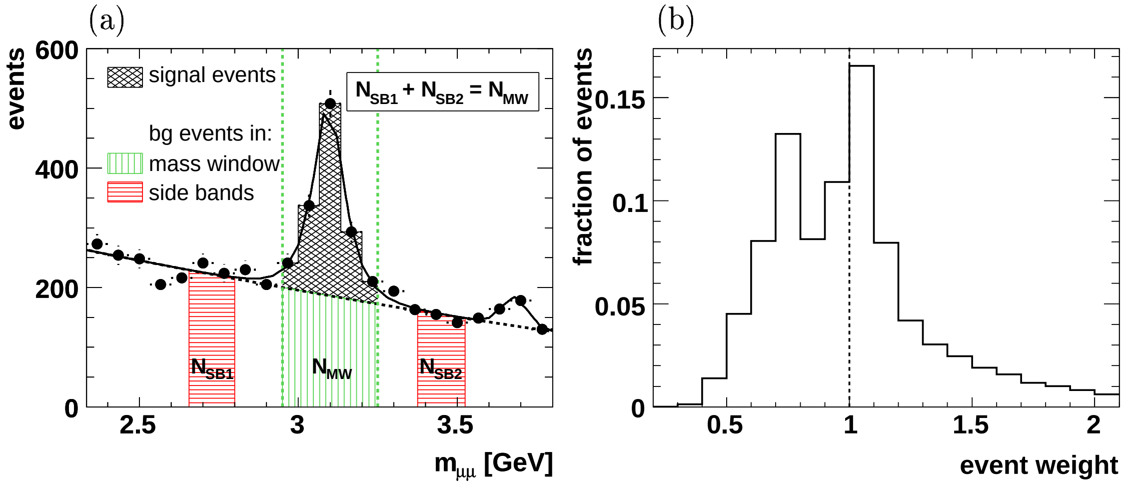

Figure 7.2: (a) Illustration of the side band method and (b) distribution of the event weights applied to the Monte Carlo simulation.

7.1 Comparison with the Monte Carlo Simulation

To determine the correct numbers for the reconstruction efficiency and the acceptance a good agreement between the data and the simulated distributions is crucial. Control plots, comparing data and Monte Carlo distributions, for the photoproduction of inelastic J/Ψ mesons are presented in this section.

The non resonant background is not included in the Monte Carlo simulation. In order to be able to compare data and simulation, the data distributions are background subtracted using a statistical method. The method is illustrated in figure 7.2. For a particular event in the mass window around the signal peak it is not possible to decide, whether it is a 'real' signal event (cross hatched area in fig. 7.2(a)) or whether it is part of the non resonant background (vertical lines in fig. 7.2(a)). However, statistically, using the side band method, the distributions of signal and background events can be determined.

The assumption is made, that the characteristics of events in the non resonant background are independent of the reconstructed mass. The distribution of a physical quantity should be identical for events in the two side bands (horizontal lines in fig. 7.2(a)) and for events in the non resonant background inside the mass window (vertical lines in fig. 7.2(a)). The distribution of the signal events can be obtained by subtracting the histogram filled with events in the side bands from the histogram filled with events in the mass window around the signal. For a correct subtraction the number of events within the side bands and within the mass window has to be the same ($N_{SB1} + N_{SB2} = N_{MW}$), hence the widths of the side bands have to be chosen properly.

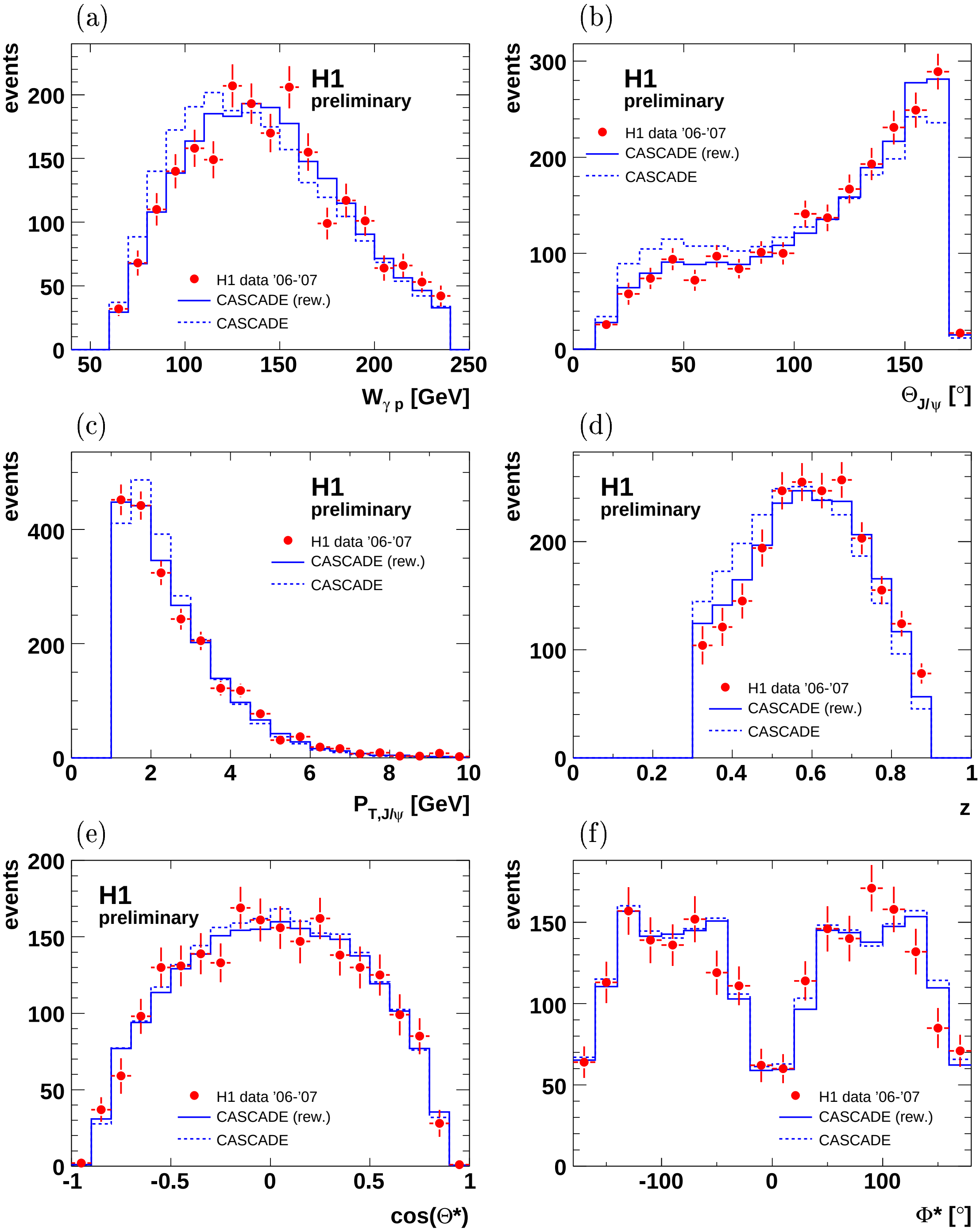

Figure 7.3: Distributions of (a) the photon proton center of mass energy $W_{\gamma p}$, (b) the polar angle of the J/Ψ mesons $\Theta_{J/\Psi}$, (c) the transverse momentum of the inelastic J/Ψ mesons $P_{T,\Psi}$, (d) the elasticity z, and the decay angular distributions (e) $\cos(\Theta^{*})$ and (f) ϕ^{*}. The data (bullets) are background subtracted and compared with the CASCADE simulation with (solid line) and without (dashed line) reweighting.

In order to achieve the best possible description of the data, the CASCADE Monte Carlo simulation is corrected to describe the kinematic distribution of the data. A fit is applied to all differing distributions in data and Monte Carlo simulation in order to minimize the impact of statistical fluctuations. Correction factors are determined as the ratio of the two corresponding fit functions as a function of $W_{\gamma p}$ and $P_{T,\Psi}$ in bins of the elasticity z. The reweighting factors are of the order of $\mathcal{O}(1)$, their distribution is plotted in figure 7.2(b).

In the figures the data (bullets) are compared with the reweighted (solid line) and the default (dashed line) CASCADE distributions.

Figure 7.3(a) shows the distribution of the photon proton center of mass energy $W_{\gamma p}$. The unweighted CASCADE simulation is shifted towards lower values with respect to the data. The reweighting as a function of $W_{\gamma p}$, additionally leads to a very good description of the polar angle distribution of the J/Ψ meson Θ_Ψ as shown in figure 7.3(b). The unweighted $P_{T,\Psi}$ spectrum of the CASCADE simulation, shown in figure 7.3(c), is somewhat shifted towards higher values. The elasticity distribution in figure 7.3(d) is too high at low values of z and too low at high values of z.

The decay angular distributions $\cos(\Theta^*)$ and ϕ^* in the figures 7.3(e) and 7.3(f) are well described by the CASCADE Monte Carlo simulation.

In all following control plots the muon μ_1 denotes the muon with the higher transverse momentum ($P_{\perp,\mu 1} > P_{\perp,\mu 2}$). In most of the events this also means that μ_1 is identified as 'iron muon' in the central muon detector (CMD) as required in the selection.

Figures 7.4(a) and (b) show the spectrum of the transverse momentum of the two decay muons. The spectrum of the muon with the higher P_T rises at 1.5–2 GeV, where the identification in the central muon detector starts. The other muons (7.4(b)) are usually identified in the calorimeter with transverse momenta starting at 0.8 GeV and a maximum in the distribution at $P_{T,\mathrm{Trk2}} \approx 1.2\,\mathrm{GeV}$.

The distributions of the polar angles Θ_μ are plotted in figure 7.4(c) and (d). Both histograms show a strong peak in the backward region of the detector ($140^\circ < \Theta < 150^\circ$). This peak is caused by the high muon reconstruction efficiency in this angular range, as explained in chapter 4 of this thesis.

To check the activity in addition to the J/Ψ meson in the detector, the scalar sum of the transverse momenta of all tracks (except the decay leptons) is plotted in figure 7.4(e). The predictions of the CASCADE simulation model the data very well.

Altogether, the data and the (reweighted) CASCADE Monte Carlo simulation match very well in all control plots.

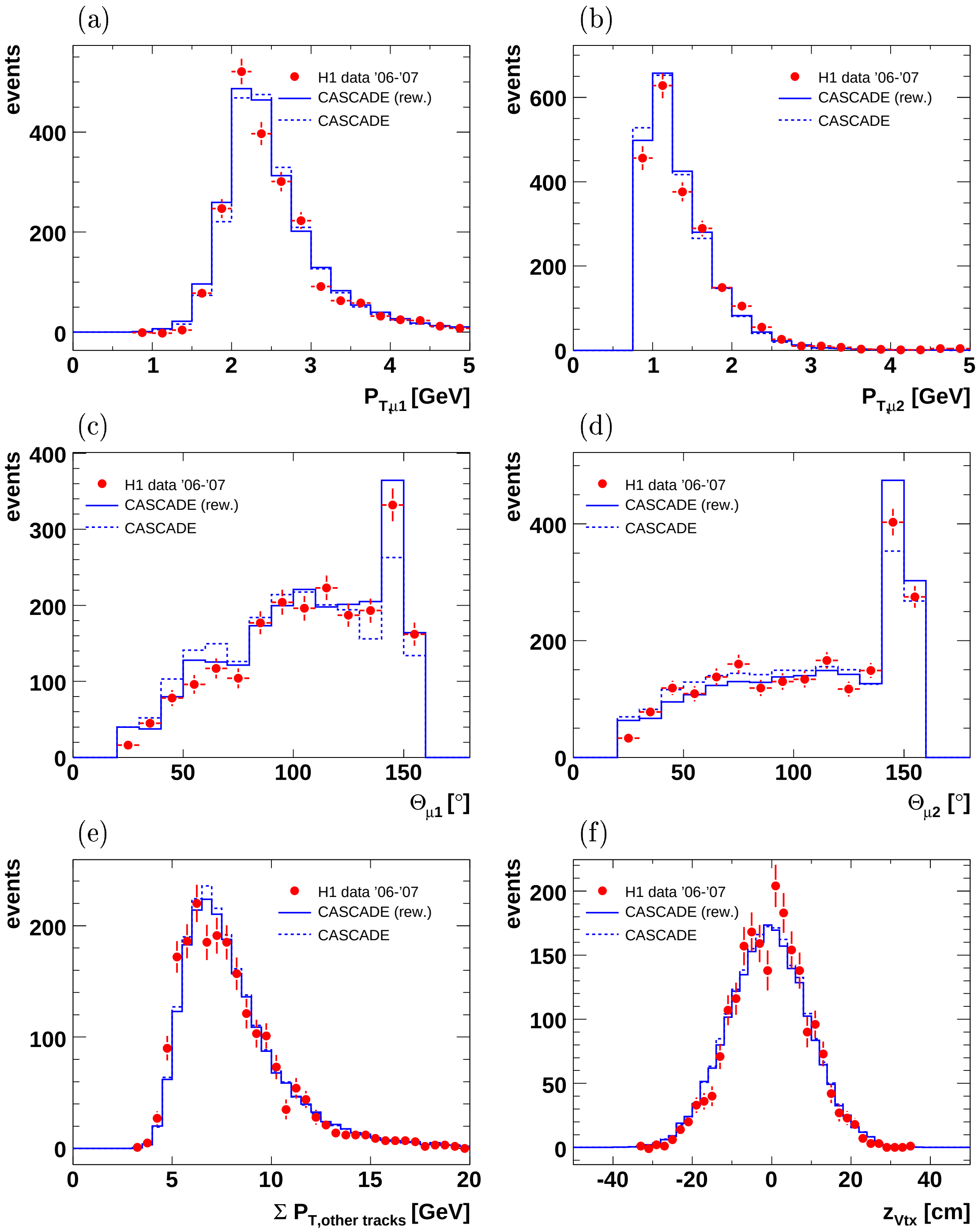

Figure 7.4: Distributions of the transverse momentum P_T [(a), (b)] and the polar angle Θ [(c), (d)] of the decay muon tracks, where μ_1 denotes the track with the larger transverse momentum. (e) shows the scalar sum of the transverse momenta of the other tracks and (f) the distribution of the z vertex. The data (bullets) are background subtracted and compared with the CASCADE simulation with (solid line) and without (dashed line) reweighting.

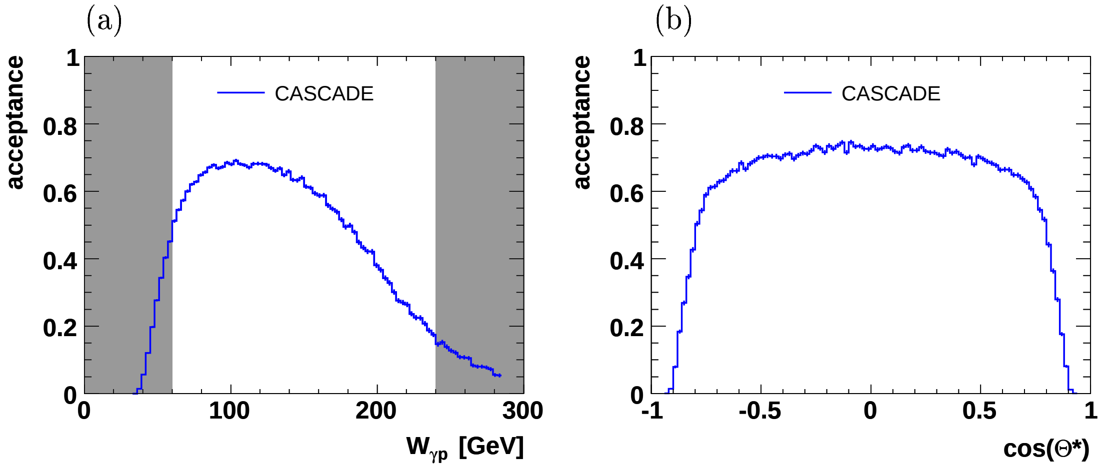

Figure 7.5: Geometrical Acceptance $\mathcal{A}_{\mathrm{Geom}}$ as determined from the CASCADE Monte Carlo simulation as a function of (a) the photon proton center of mass energy $\mathrm{W}_{\gamma p}$ and (b) the decay angular distribution $\cos(\Theta^*)$. The grey areas are rejected in the selection.

7.2 Cross Section Definition

For the measurement of the photoproduction cross section of inelastic J/Ψ mesons, the number of signal events in each bin is normalised to the integrated luminosity, correcting for detector efficiencies and acceptance

$$\sigma_{\mathrm{ep}} = \frac{\mathrm{N}_{\mathrm{signal}}}{\mathcal{L} \cdot \epsilon \cdot \mathcal{BR}} = \frac{\mathrm{N}_{\mathrm{signal}}}{\mathcal{L} \cdot \mathcal{BR}} \cdot \frac{1}{\epsilon_{\mathrm{Trigger}} \cdot \epsilon_{\mathrm{Reco}} \cdot \mathcal{A}_{\mathrm{Geom}}}, \qquad (7.1)$$

where $\mathrm{N}_{\mathrm{signal}}$ denotes the number of signal events in the analysis bin obtained from the fit. $\mathcal{L}$ corresponds to the total integrated luminosity of the analysed data taking period and $\mathcal{BR}$ to the branching ratio of the J/Ψ decay into a muon pair.
The efficiency ϵ gives the fraction of events which are actually reconstructed and triggered within the acceptance region of the H1 detector. It is split into the trigger efficiency $\epsilon_{\mathrm{Trigger}}$, the reconstruction efficiency ϵ_{Reco} and the geometrical acceptance $\mathcal{A}_{\mathrm{Geom}}$. In the photoproduction part of this analysis the trigger efficiency is taken from the Monte Carlo simulation as described in chapter 5 of this thesis. The measured ep cross sections are translated to γp cross sections using the photon flux factor Φ_γ (cf. section 2.2).

The reweighted CASCADE Monte Carlo sample describes the data precisely. It is used to correct the data for losses due to geometrical acceptance $\mathcal{A}_{\mathrm{Geom}}$ and reconstruction efficiency ϵ_{Reco}. The acceptance $\mathcal{A}_{\mathrm{Geom}} = \mathrm{N}_{\mathrm{gen,trk}}/\mathrm{N}_{\mathrm{all}}$ is purely geometric. It denotes the fraction of events for which both decay muons fulfil the track cuts of the analysis on generator level ($\mathrm{N}_{\mathrm{gen,trk}}$) with respect to all events within the analysed phase space ($\mathrm{N}_{\mathrm{all}}$). Figure 7.5 shows the geometric acceptance $\mathcal{A}_{\mathrm{Geom}}$ as a function of the center of mass energy in the photon proton rest frame $\mathrm{W}_{\gamma p}$ and the

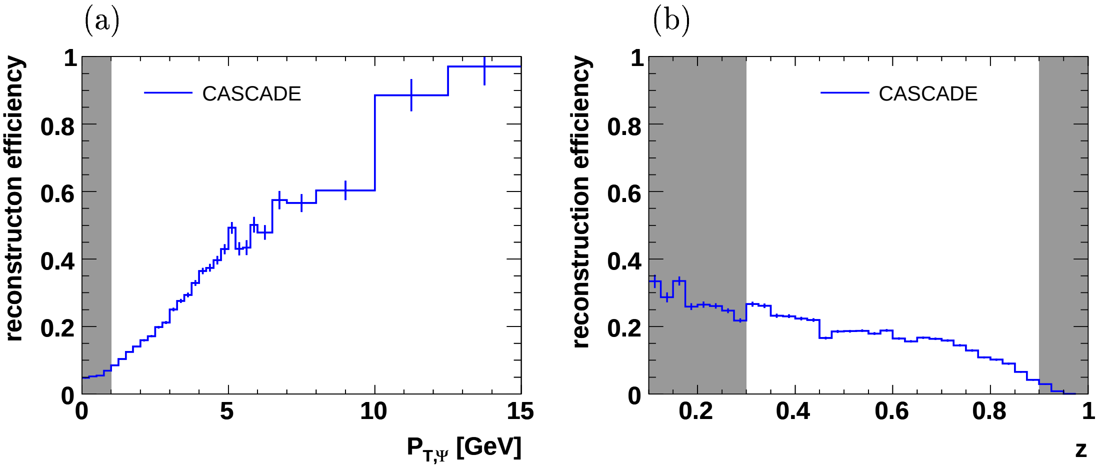

Figure 7.6: Reconstruction efficiency ϵ_{Reco} as obtained by the CASCADE Monte Carlo simulation as a function of (a) the transverse momentum of the J/Ψ meson $P_{T,\Psi}$ and (b) the elasticity z. The grey areas are rejected in the selection.

decay angular distribution $\cos(\Theta^*)$. Low values of $W_{\gamma p}$ are correlated to J/Ψ mesons in the forward direction (at low polar angles Θ_Ψ). Subsequently the decay tracks also tend to be in the very forward region and the acceptance breaks down. The photon proton center of mass energy in this analysis is restricted to $60 \leqslant W_{\gamma p} \leqslant 240\,\text{GeV}$, providing an acceptance of more than 25 % in the analysis bins.

The reconstruction efficiency $\epsilon_{\text{Reco}} = N_{\text{rec,trk}}/N_{\text{gen,trk}}$ corresponds to the fraction of events within the acceptance region of the H1 detector ($N_{\text{gen,trk}}$) which are actually reconstructed ($N_{\text{rec,trk}}$). The reconstruction efficiency is dominated by the lepton identification, while the track and vertex reconstruction in the central tracking detector is very efficient in the range of transverse momenta of this analysis. Figure 7.6(a) shows the reconstruction efficiency as a function of the transverse momentum of the J/Ψ meson $P_{T,\Psi}$. For $P_{T,\Psi} \lesssim 5\,\text{GeV}$ the reconstruction efficiency rises from 5 % to 50 %, due to the strong dependence on the track momentum of the lepton identification in the central muon detector.

Due to the cut on the track multiplicity, the reconstruction efficiency as a function of the elasticity z (cf. fig. 7.6(b)) decreases slightly towards larger values of the elasticity, for $z \gtrsim 0.9$ almost no J/Ψ mesons are reconstructed. The lowering at moderate values of the elasticity is caused by the correlation of z and $P_{T,\Psi}$. At larger values of z, the transverse momentum of the J/Ψ meson is expected to be lower, hence the reconstruction efficiency decreases as described before. The drop at large values of z is a consequence of the cut on the number of tracks in the central region ($N_{\text{Trk,central}} \geqslant 5$). At large values of the elasticity, the activity in the detector (beside the J/Ψ meson) is by definition small, and most of the events do not pass the cut on the track multiplicity.

The cuts on the transverse momentum of the J/Ψ meson $P_{T,\Psi} \geqslant 1\,\text{GeV}$ and on

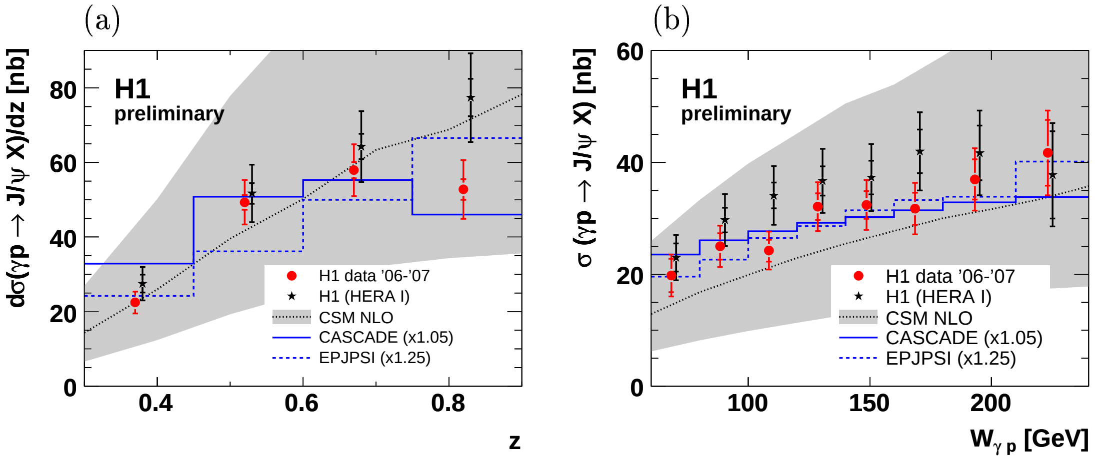

Figure 7.7: Differential cross sections for the photoproduction of inelastic J/Ψ mesons in the kinematic range $60 \leqslant \mathrm{W}_{\gamma p} \leqslant 240\,\mathrm{GeV}$, $\mathrm{P}_{\mathrm{T},\Psi} \geqslant 1\,\mathrm{GeV}$ and $0.3 \leqslant \mathrm{z} \leqslant 0.9$ as function of (a) the elasticity z and (b) the photon proton center of mass energy $\mathrm{W}_{\gamma p}$.

the elasticity $0.3 \leqslant \mathrm{z} \leqslant 0.9$ are introduced to reduce contributions from diffractive processes (at large values of z and low $\mathrm{P}_{\mathrm{T},\Psi}$) and from the decay of B mesons (at low values of z).

7.3 Cross Section Measurement

The measurement of the photoproduction of inelastic J/Ψ mesons is performed using data collected with the H1 experiment in the years 2006 and 2007 corresponding to an integrated luminosity of $\mathcal{L}_{\gamma\mathrm{p}} \approx 166\ \mathrm{pb}^{-1}$. The analysis is carried out at medium elasticities ($0.3 \leqslant \mathrm{z} \leqslant 0.9$) in the kinematic range $\mathrm{Q}^2 \approx 0\,\mathrm{GeV}^2$, $60 \leqslant \mathrm{W}_{\gamma p} \leqslant 240\,\mathrm{GeV}$ and $\mathrm{P}_{\mathrm{T},\Psi} \geqslant 1\,\mathrm{GeV}^2$.

The total photoproduction cross section at an average energy in the photon proton center of mass system of $\langle \mathrm{W}_{\gamma p} \rangle = 116\,\mathrm{GeV}$ is measured to be

$$\sigma_{\gamma\mathrm{p}}\,(\gamma\mathrm{p} \rightarrow \mathrm{J}/\Psi\mathrm{X}) \quad = \quad 26.8 \pm 1.6(\mathrm{stat.}) \pm 3.2(\mathrm{syst.})\,\mathrm{nb}. \tag{7.2}$$

The statistical uncertainty is 5.9 % on the total cross section measurement. The systematic uncertainty is quantified to be 11.5 %. The largest systematic uncertainties arise from the impact of model uncertainties on acceptance and reconstruction efficiency. The systematic uncertainties are explained later on in section 7.4. The photon flux factors Φ_γ^{T} which are used for the transition to the γp cross section are listed in section 2.2 of this thesis. The measured cross sections are not corrected for contributions from events with J/Ψ mesons that are produced in decays of B mesons or $\Psi(2\mathrm{S})$ mesons, these contributions are addressed later on in this section.

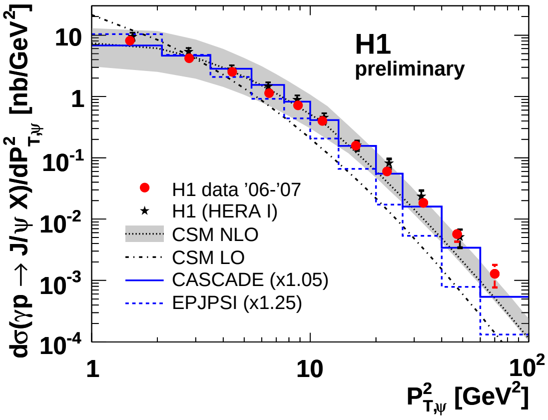

Figure 7.8: Differential cross sections for the photoproduction of inelastic J/Ψ mesons in the kinematic range $60 \leqslant \mathrm{W}_{\gamma p} \leqslant 240\,\mathrm{GeV}$, $\mathrm{P}_{\mathrm{T},\Psi} \geqslant 1\,\mathrm{GeV}$ and $0.3 \leqslant \mathrm{z} \leqslant 0.9$ as function of the squared transverse momentum of the J/Ψ meson $\mathrm{P}^2_{\mathrm{T},\Psi}$.

Differential Cross Sections

Single differential photoproduction cross sections were extracted as a function of the center of mass energy in the photon proton center of mass frame $\mathrm{W}_{\gamma p}$, the elasticity z, the transverse momentum squared of the J/Ψ meson $\mathrm{P}^2_{\mathrm{T},\Psi}$ and the decay angular distribution of the beam lepton signed decay muon $\cos(\Theta^*)$. The distributions in $\mathrm{P}^2_{\mathrm{T},\Psi}$ and z are further investigated by dividing the sample into bins of z and $\mathrm{P}_{\mathrm{T},\Psi}$ respectively. The measured cross sections are shown in the figures 7.7 to 7.9. In the figures the results of this analysis are plotted as bullets. The data points are compared to theoretical predictions in the framework of the color singlet model (CSM). Leading order calculations are shown as implemented in the Monte Carlo generators Cascade using k_T factorisation (solid line) and Epjpsi (dashed line) [JS01, Jun92]. For the cross section as a function of $\mathrm{P}^2_{\mathrm{T},\Psi}$ a leading order calculation is shown as dashed dotted line. Next to leading order calculations for the inelastic J/Ψ photoproduction [Kra96] are drawn as dotted line with grey error bands where available. The results are compared to former H1 results (black stars) [H102b].

The agreement between the H1 publication and this analysis at low and medium values of the elasticity z ($0.3 < \mathrm{z} \leqslant 0.75$) is very satisfactory (cf. fig. 7.7(a)). In the largest bin of the elasticity ($0.75 < \mathrm{z} \leqslant 0.9$) the Hera I cross section point exceeds the result of this analysis by roughly $1.5\,\sigma$. This leads to a difference in the total measured cross section with respect to the former H1 analysis. Except for this difference in the normalisation, both H1 results agree very well in all variables.
The difference in the highest bin of the elasticity was studied in detail. This analysis applies harder cuts to reduce contributions from diffractive $\Psi(2\mathrm{S})$. Therefore the amount of background events in the selected data sample at large values of the

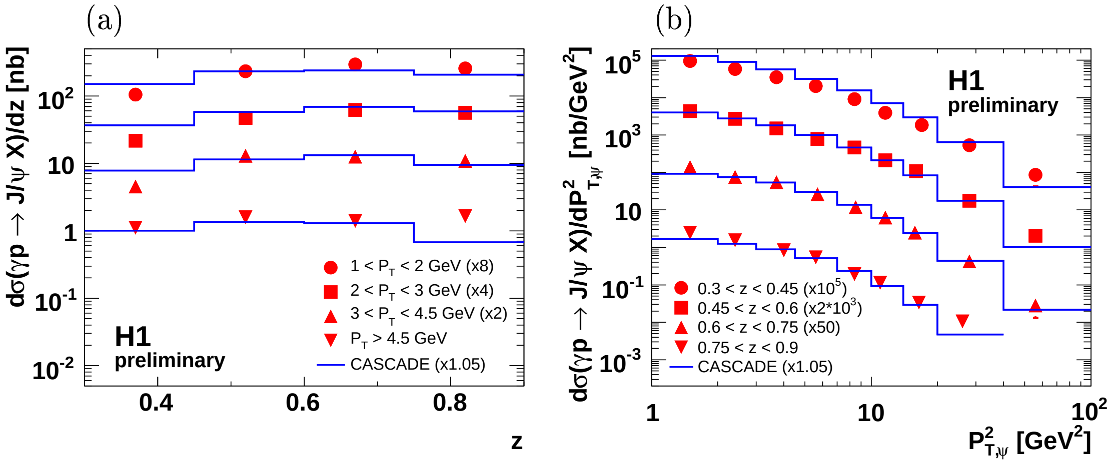

Figure 7.9: Double differential cross sections for the photoproduction of inelastic J/Ψ mesons in the kinematic range $60 \leqslant W_{\gamma p} \leqslant 240\,\mathrm{GeV}$, $P_{T,\Psi} \geqslant 1\,\mathrm{GeV}$ and $0.3 \leqslant z \leqslant 0.9$ as function of (a) the transverse momentum of the J/Ψ meson $P_{T,\Psi}$ in bins of the elasticity z and (b) the elasticity z in bins of the transverse momentum $P_{T,\Psi}$.

elasticity z is significantly lower with respect to the HERA I analysis.

Another difference arising from a correction of the data using different models, CASCADE or EPJPSI, is treated as a systematic uncertainty in section 7.4.

The predictions of the k_T factorisation ansatz as implemented in the Monte Carlo generator CASCADE, model the shapes and the overall normalisation of the data very well. As a function of $W_{\gamma p}$, plotted in figure 7.7(b), the CASCADE prediction is somewhat too high at low values of $W_{\gamma p}$ and slightly too low at large values of $W_{\gamma p}$. The double differential cross sections (cf. fig. 7.9) are also well described using the k_T factorisation ansatz in leading order. At the extreme values, low z/low $P_{T,\Psi}$ and large z/large $P_{T,\Psi}$, the CASCADE simulation deviates somewhat from the data. The overall cross section prediction of the CASCADE simulation is however very close to the measured one.

The predictions from the NLO calculations are indicated as dotted line. The uncertainty of the NLO calculation is drawn as grey band. It is obtained by a variation of the charm quark mass m_c and of α_s ($1.3 < m_c < 1.5\,\mathrm{GeV}$, $\alpha_s = 0.1200 \pm 0.0025$). Within the uncertainties the NLO calculations are able to describe the data, however the uncertainties are too large to draw a strong conclusions.

Color singlet model predictions in leading order (LO) fail to describe the data. The predicted $P_{T,\Psi}$ spectrum in the EPJPSI Monte Carlo simulation and in the CSM LO calculation overshoot the data at low values of the transverse momentum. As plotted in figure 7.8, the predicted cross sections are nearly one order of magnitude below the data at large $P_{T,\Psi}$. In contrast to the data, the CSM LO calculation predicts a continuous rise towards larger values of the elasticity z.

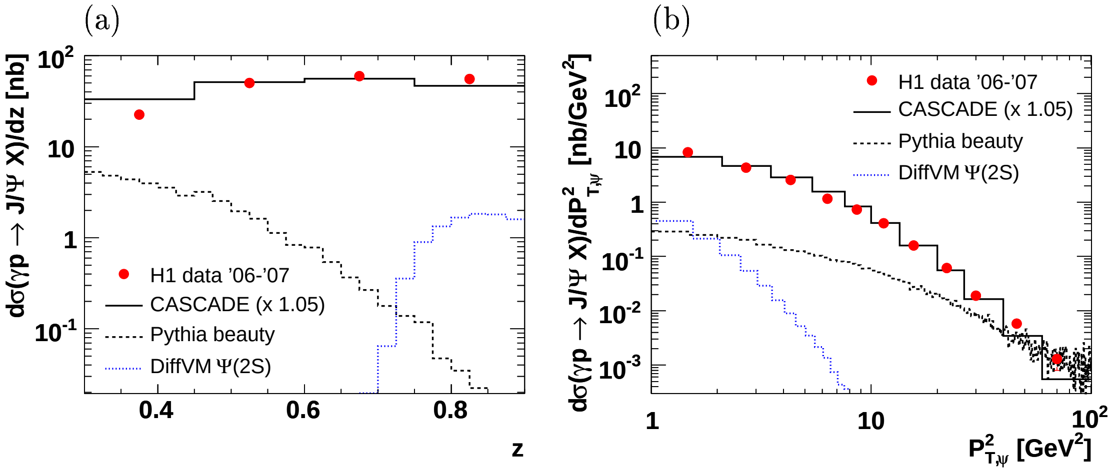

Figure 7.10: Contributions from decays of B mesons and diffractively produced $\Psi(2S)$ mesons to the differential cross sections as a function of the elasticity z and the squared transverse momentum $P^2_{T,\Psi}$.

In conclusion, the inelastic J/Ψ meson production at HERA can be described according to the color singlet model, provided that higher order corrections are taken into account. Higher order terms which are implicitly included in the k_T factorisation approach reproduce the measured cross sections very well, however already a calculation at next to leading order is capable of modelling the transverse momentum spectrum at HERA, though the error of this prediction is very large.

Contributions from color octet states in the factorisation ansatz in NRQCD are expected to manifest themselves at large elasticities and large transverse momenta. No indication for noticeable contributions from color octet states to the J/Ψ meson production at HERA are observed, since the measured cross sections are very well described by predictions in the color singlet model,

Contributions from Indirectly Produced J/Ψ Mesons

The measured cross sections contain noticeable contributions from non prompt produced J/Ψ mesons. Figure 7.10 shows the differential cross sections as a function of the elasticity and the transverse momentum of the J/Ψ meson on a logarithmic scale. In addition to the data points and the CASCADE prediction the dashed line depicts the contribution from J/Ψ mesons produced in the decay of B mesons. The dotted line corresponds to J/Ψ mesons from the cascade decay of diffractively produced Ψ(2S) mesons.

The contribution from B mesons is determined using a $b\bar{b}$ Monte Carlo sample generated with PYTHIA. To estimate the fraction of J/Ψ mesons coming from Ψ(2S) mesons a DIFFVM Monte Carlo sample is used.

The simulations are scaled to the luminosity of the data sample and the branching ratios into J/Ψ mesons are corrected to the values given in [PDG08]. Furthermore

Source		Uncertainty [%]
Reconstruction of decay leptons	track, vertex	4
	identification	5
Number of signal events		2
Trigger		5
Model uncertainties	decay angular distribution	5
	$P_{T,\Psi}$ spectrum	5
	(track multiplicity only $z \geqslant 0.75$	8)
Hadronic energy scale		2
Integrated luminosity		2
Decay branching ratio		1
Sum		11.5–14

Table 7.1: Sources of systematic uncertainties which are taken into account in the photoproduction analysis. For the highest bin of the elasticity z, the systematic uncertainty amounts to 14 % due to the additional error arising from the track multiplicity.

the total cross sections are adapted to published H1 measurements [H199, H196].
J/Ψ mesons from B meson decays have rather low elasticities due to the high track multiplicity of events involving beauty quarks. The contribution is estimated to be 20 % in the lowest elasticity bin and 3.5 % in the full data sample. Towards larger transverse momenta of the J/Ψ meson the beauty fraction rises continuously.
The elasticity distribution of J/Ψ mesons from the cascade decay of Ψ(2S) mesons has a maximum at $z \approx 0.85$. Diffractively produced charmonia are expected to show a much faster decrease in the $P_{T,\Psi}$ spectrum, which is also visible in figure 7.10(b). Overall the amount of J/Ψ mesons from the decay of diffractively produced Ψ(2S) mesons is determined to be 1.1 %. Most of them are located in the highest elasticity bin, where the contribution is quantified to be 3 %.
An irreducible fraction of about 22.7 % of the events is expected to originate from inelastic Ψ(2S) mesons, as calculated in section 7.6.

7.4 Systematic Uncertainties

To obtain the systematic uncertainty of the analysis, the different sources of uncertainties were studied. Various measured quantities, which serve as an input for the reconstruction of the kinematic variables, were varied in the Monte Carlo simulation. The simulation was reweighted within the visible range constrained by the data in order to check the impact on the acceptance. Finally different methods for the extraction of the number of signal events were compared.

In the following the sources of systematic uncertainties are described, the impact on the inelastic J/Ψ production cross section of each source is thoroughly studied. Unless differently specified, the systematic uncertainty for a particular source is taken as the variation of the measured cross section caused by the variation of the variable. The total systematic uncertainty of the measurements is obtained by adding all contributions in quadrature. It adds up to 11.5 % for the photoproduction analysis.

The sources of systematic uncertainties for photoproduction analysis are summarised in table 7.1.

Track Reconstruction and Lepton Identification

The decay lepton identification is described in detail in chapter 4 of this thesis. The study of the identification efficiency yields a systematic uncertainty of 5%.
The uncertainty of the track reconstruction efficiency is 2% per lepton track.

Signal Extraction

The method for the signal extraction is explained in detail in section 6.5 of this thesis. The systematic uncertainty for the extraction of the number of signal events is obtained by comparing the result from the fit to signal and background to the number of events above the fitted background function and a variation of the normalisation of the background function. This leads to an uncertainty of 2–5% for the decay channel into muons and 6–8% for the decay channel into electrons, increasing with the amount of combinatorial background (i.e. towards lower values of the elasticity z).

Trigger Efficiency

A detailed description of the trigger efficiency can be found in chapter 5 of this thesis. For the photoproduction analysis the trigger efficiency is taken from the Monte Carlo simulation. The efficiencies are corrected using data from independent trigger channels where necessary. The remaining uncertainty is 5%.

Model Uncertainties

Model uncertainties arise either from the need to correct for loss of events in the region where decay lepton tracks cannot be measured or from disagreements in the description of the data in the control plots. The following describes the three different model uncertainties which are taken into account.

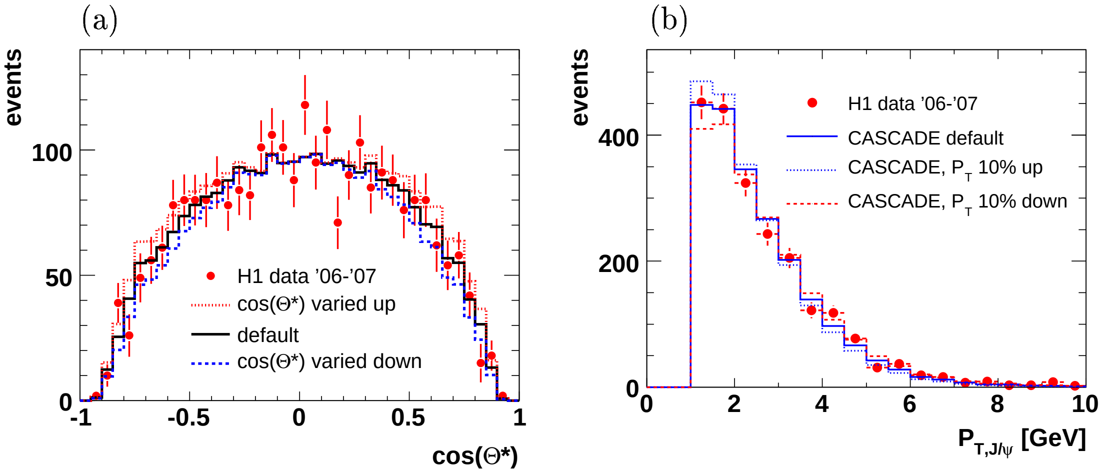

Figure 7.11: Variation of the distributions for (a) the decay angular variable $\cos(\Theta^*)$ and (b) the transverse momentum of the J/Ψ meson $P_{T,\Psi}$.

Geometric Acceptance $\mathcal{A}_{\mathrm{Geom}}$

The geometric acceptance $\mathcal{A}_{\mathrm{geom}}$ is determined by comparing the number of generated J/Ψ events with the number of J/Ψ events in which the decay leptons are within the detector acceptance. The result depends strongly on the assumed decay angular distribution of $\cos(\Theta^*)$. To determine the systematic uncertainty on the cross section measurement the shape of the angular distribution, shown in figure 7.11(a), was varied within the range constrained by the visible distribution of the data $(1 \pm 0.3 \cdot \cos^2(\Theta^*))$.

Figure 7.12(a) shows the dependence of the result on the model assumptions made in the CASCADE Monte Carlo simulation. The variation yields a systematic uncertainty of 5%. -

$P_{T,\Psi}$ distribution

As shown in section 7.2 of this thesis, the reconstruction efficiency depends strongly on the transverse momentum of the J/Ψ meson. An uncertainty on the description of the $P_{T,\Psi}$ spectrum (cf. fig. 7.11(b)) is taken into account by a variation of the slope of the $P_{T,\Psi}$ distribution in the CASCADE Monte Carlo simulation. The average value of the $P_{T,\Psi}$ spectrum, $\langle P_{T,\Psi} \rangle \approx 2.5\,\mathrm{GeV}$, is used as pivot for a linear variation of the slope. A variation by $\pm 10\,\%$ at values of $P_{T,\Psi} = 1\,\mathrm{GeV}$ leads to a reverse variation by $\mp 40\,\%$ at values of $P_{T,\Psi} \approx 10\,\mathrm{GeV}$.

This variation results in a change of the measured cross section of up to 5%.

Track Multiplicity

In the context of this thesis for the first time, the reliability of the acceptance correction arising from a cut on the track multiplicity and the impact of different model

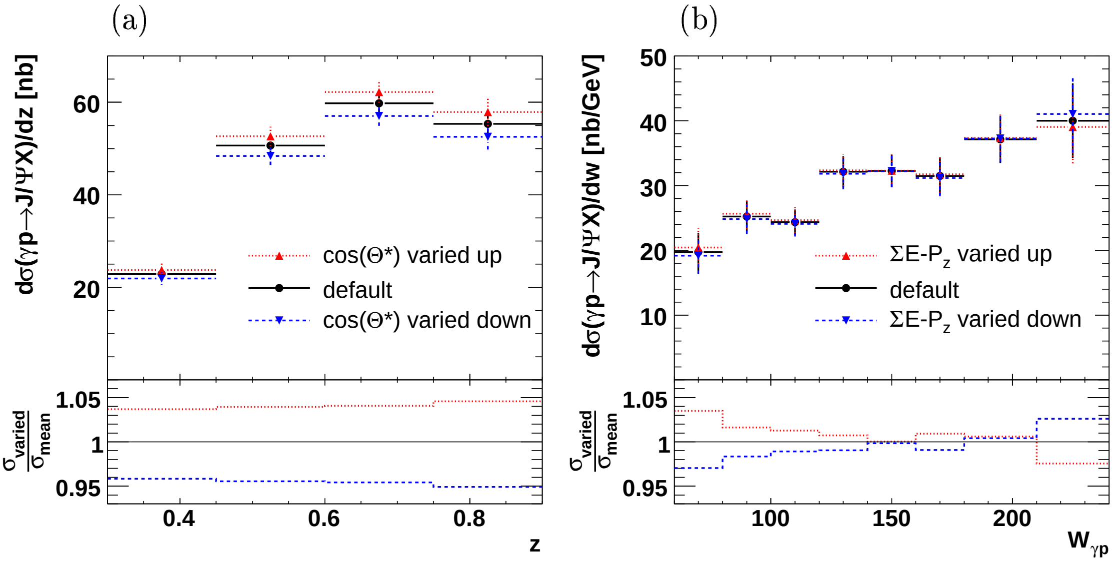

Figure 7.12: Systematic uncertainties arising from the variation of (a) the decay angular distribution $\cos(\Theta^*)$ $(1 \pm 0.3 \cdot \cos^2(\Theta^*))$ and (b) the hadronic energy scale (± 4% in LAr, ± 7% in SpaCal).

assumptions is studied in detail.

In figure 7.13 the track multiplicity is plotted down to $N_{\text{Trk,central}} = 3$. The data are compared to Cascade and Epjpsi simulations respectively.
Due to diffractively produced $\Psi(2S)$ mesons with subsequent decay into a J/Ψ meson and two charged pions the number of data events with three or four central tracks increases significantly. In order to reduce diffractively produced background at least five central tracks are required for the selected events in this analysis. In the end the measured cross sections are corrected for this cut using a Monte Carlo simulation.
In this analysis the Cascade Monte Carlo simulation is used to correct the measured number of signal events in the data. Epjpsi fails to describe many aspects of the data without the application of large correction factors. It is only used as a second model to cross check the acceptance corrections arising from the experimental cut on the track multiplicity.
The predictions for the track multiplicity below five tracks disagree in the Cascade and the Epjpsi Monte Carlo simulation. The Cascade simulation decreases instantly, while the Epjpsi Monte Carlo has its maximum for $N_{\text{Trk,central}} = 4$ before it decreases as well. For events with five and six tracks the Cascade expectation (dashed line in 7.13(a)) is below the data, whereas the Epjpsi Monte Carlo (dashed line in 7.13(b)) lies slightly above the data. However both generators describe the track multiplicity for $N_{\text{Trk,central}} \geqslant 5$ reasonably.
In order to model the track multiplicity in the data down to three tracks with the Monte Carlo simulation, events from a DiffVM Monte Carlo sample with proton dissociative $\Psi(2S)$ mesons (grey histogram) are added to the predictions from Cas-

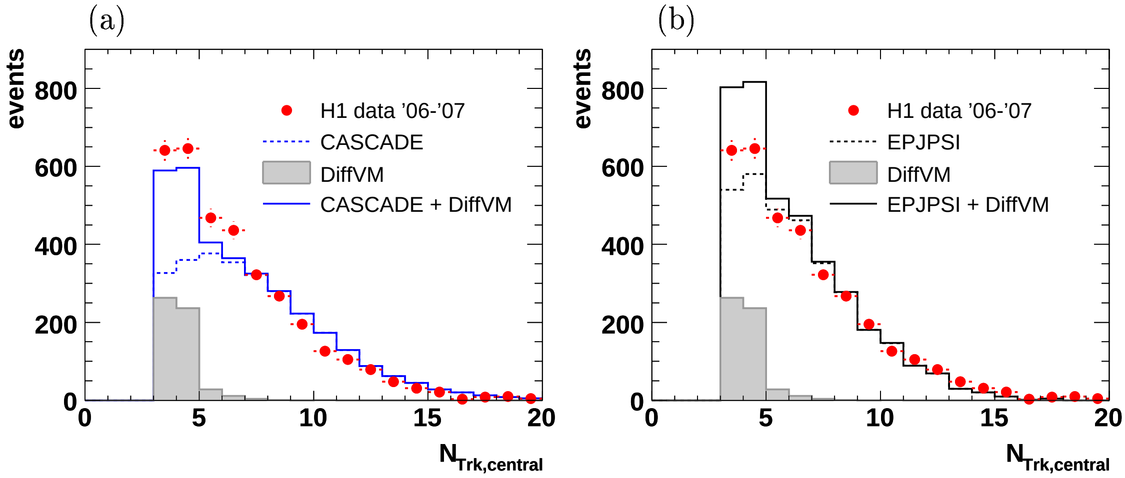

Figure 7.13: Track multiplicity for the photoproduction analysis down to three tracks. The data are compared to the (a) CASCADE and (b) EPJPSI Monte Carlo simulation. A DIFFVM MC sample is added in order to describe the data down to $\mathrm{N_{Trk,central}} = 3$.

CADE and EPJPSI (solid lines). The cross section of the DIFFVM Monte Carlo simulation is adapted to a previous H1 publication [H196]. The uncertainty on the normalisation of the DIFFVM Monte Carlo simulation is large and contributions from proton dissociative J/Ψ are not taken into account in this plot.

The track multiplicity below five tracks is better modelled by the sum of DIFFVM and CASCADE, while the EPJPSI simulation does not allow substantial contributions from diffractive processes.

The different track multiplicities yield different acceptance corrections and thus a difference in the measured cross sections. This affects predominantly the largest bin of the elasticity z, hence an additional systematic uncertainty of 8 % is applied for this bin.

Hadronic Energy Scale

The systematic error arising from the uncertainty of the hadronic energy scale is determined by varying the energy of the calorimeter objects in the data by ±4% in the LAr calorimeter and ±7% in the SpaCal. This leads to a variation of the measured cross sections of about 2% (cf. fig. 7.12).

Decay Branching Ratio

The decay branching ratio is known to a precision of 1% for both electrons and muons [PDG08].

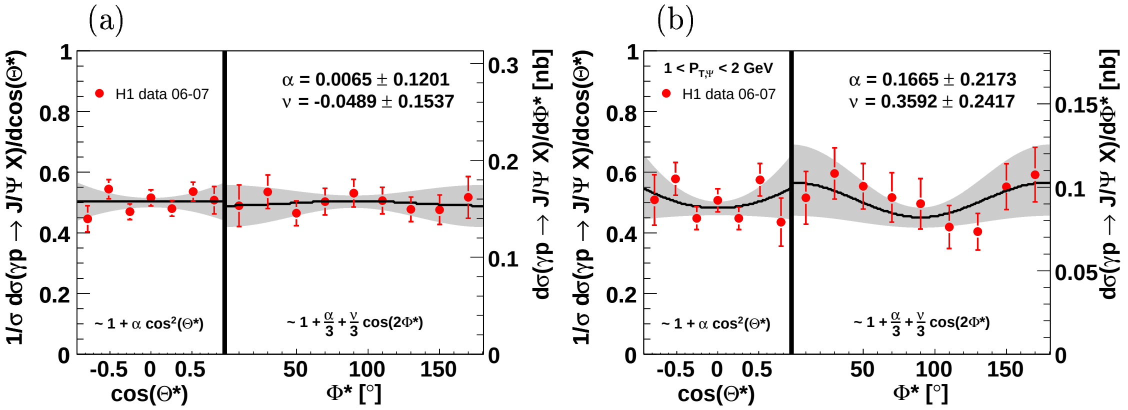

Figure 7.14: Cross sections as a function of the decay angular distributions $\cos(\Theta^*)$ shown in the range $-0.9 \leqslant \cos(\Theta^*) \leqslant 0.9$ and ϕ^* for (a) the overall sample and (b) the first bin in $P_{T,\Psi}$ ($1 < P_{T,\Psi} < 2\,\text{GeV}$). The fit result is drawn as black line, the grey band indicates the 1σ uncertainty of the fit result.

The same uncertainties are equally attributed to all bins of the measurement except for the uncertainty of the signal extraction which is 3% at moderate and large values of z and up to 5% at small values of z where the combinatorial background is largest. In the highest z bin of the photoproduction analysis an additional uncertainty for the Monte Carlo model of 8% is used.

7.5 J/Ψ Polarisation

The various models for the production of J/Ψ mesons predict different polarisations of the J/Ψ mesons. Thus preferred and unfavoured production processes can be distinguished by measuring the polarisation. The two polarisation variables α and ν are determined in a new way by a simultaneous fit to the decay angular distributions $\cos(\Theta^*)$ and ϕ^*. These angles are explained in detail in section 2.7.

The measurement of the polarisation variables depends on the shape of the measured cross section. It is not necessary to account for uncertainties on the absolute normalisation.

The systematic uncertainty can be neglected compared to the very large statistical errors.

The shape of the ϕ^* distribution depends on both polarisation variables, while the shape of the $\cos(\Theta^*)$ distribution is parametrised using only α

$$\frac{\mathrm{d}\sigma}{\mathrm{d}\cos(\Theta^*)} \propto 1 + \alpha \cdot \cos^2(\Theta^*) \tag{7.3}$$

$$\frac{\mathrm{d}\sigma}{\mathrm{d}\phi^*} \propto 1 + \frac{\alpha}{3} + \frac{\nu}{3}\cos\left(2 \cdot |\phi^*|\right) \tag{7.4}$$

Figure 7.14(a) shows the decay angular distributions $\cos(\Theta^*)$ and ϕ^* and the result of the fit to the whole data sample. Both decay angular distributions are

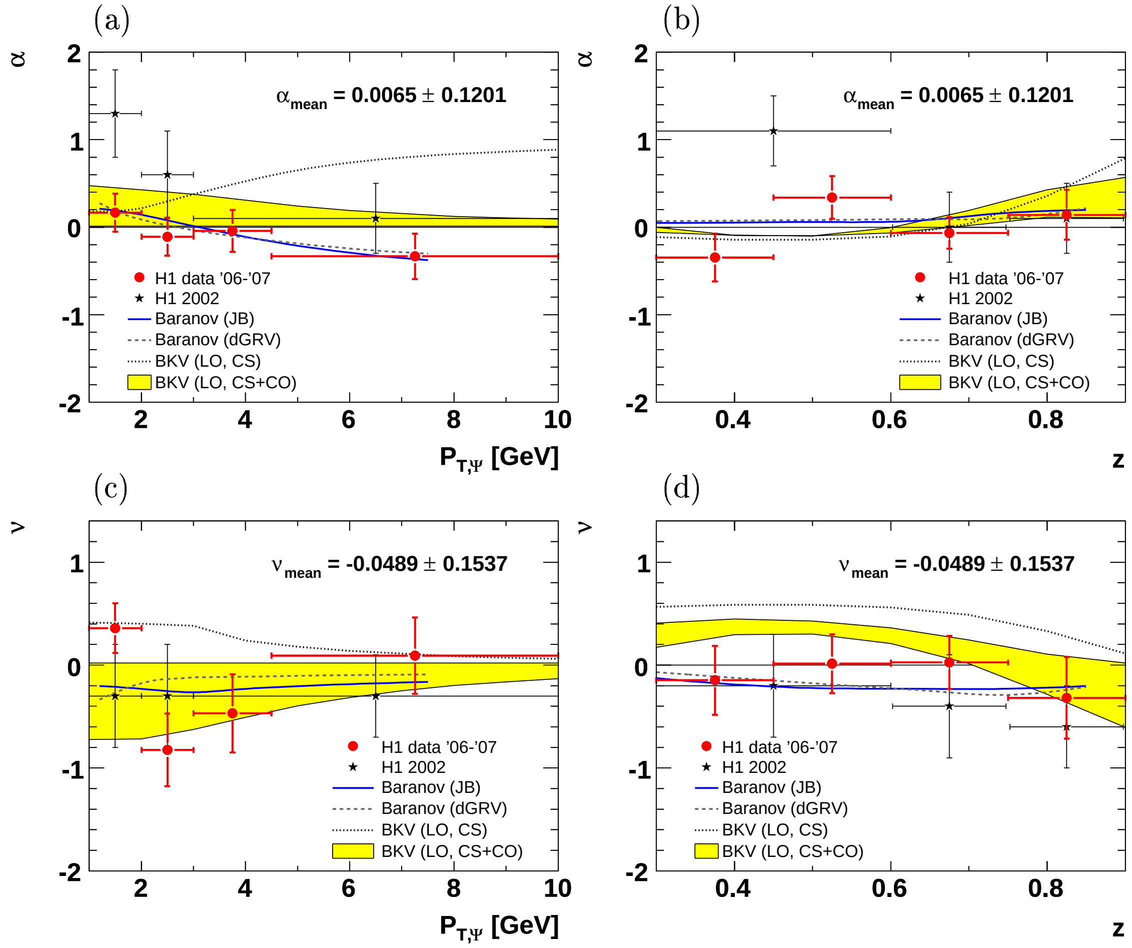

Figure 7.15: Polarisation variables α and ν as a function of the transverse momentum of the J/Ψ meson and the elasticity z. The results are compared to a previous H1 measurement [H102b]. Also shown are leading order theoretical calculations in the color singlet model (LO, CS), in the factorisation ansatz in NRQCD (LO, CS+CO) [BKV98] and in the CSM using k_T factorisation (Baranov), where 'JB' and 'dGRV' represent two different parametrisations of unintegrated gluon densities [Bru07].

flat. The resulting values for the polarisation variables are $\alpha = 0.0065 \pm 0.12$ and $\nu = -0.049 \pm 0.15$. This means that in average the J/Ψ mesons are produced unpolarised.

In addition, the polarisation variables were studied in bins of the transverse momentum of the J/Ψ meson $P_{T,\Psi}$ and the elasticity z. The distributions in the lowest bin of $P_{T,\Psi}$ ($1 < P_{T,\Psi} < 2\,\text{GeV}$) are shown in figure 7.14(b).

The obtained polarisation variables α and ν as a function of $P_{T,\Psi}$ and z are presented in the figures 7.15(a–d). The data are compared to a previous H1 publication [H102b] and to different theoretical predictions. A leading order CSM calculation by Martin Beneke, Michael Krämer and Mikko Vänttinen is represented by the

dotted line [BKV98]. The shaded area corresponds to a NRQCD prediction also published in the given paper. Calculations in the CSM using k_T factorisation performed by Sergey Baranov are shown as dashed and solid lines, where 'JB' and 'dGRV' represent two different parametrisations of unintegrated gluon densities [Bru07].
All models predict similar values for the polarisation variable α at low values of $P_{T,\Psi}$ as well as over the whole analysed elasticity range. Towards larger values of $P_{T,\Psi}$ a difference between the predictions becomes visible, while at the same time the statistical uncertainty of the measurement increases. The measured α shows a trend to small longitudinal polarisation towards larger $P_{T,\Psi}$, consistent with a recent CDF (run II) measurement [CDF07]. This trend is modelled very well by the k_T factorisation approach. The NRQCD calculation is also capable of describing the data within large errors, while the measurement seems to disfavour the leading order color singlet prediction.
Looking at the polarisation variable ν as a function of the elasticity, the data tend to be at small negative values. Again, this is reproduced by the k_T factorisation approach, while the NRQCD and all the more the CSM LO predictions are above the data in all bins.

The J/Ψ meson polarisation is very well reproduced by predictions using a k_T factorisation approach in the CSM, confirming the conclusion of the cross section measurement. At the moment the k_T factorisation approach achieves the best description of the data. Leading order CSM calculations seem to be disfavoured by this measurements, whereas NRQCD predictions cannot be withdrawn by means of the polarisation measurement, though the cross section measurement shows that color octet contributions are unnecessary to model the inelastic J/Ψ meson production at HERA.
However, the statistical uncertainty of the measurement is large and the measured polarisation variables are consistent with an unpolarised J/Ψ production in all bins.

7.6 $\Psi(2S)$ to J/Ψ Ratio

For two reasons it is worth measuring the ratio of the inelastic $\Psi(2S)$ cross section relative to the J/Ψ cross section, $\sigma_{\gamma p}^{\Psi(2S)}/\sigma_{\gamma p}^{J/\Psi}$. On the one hand this measurement can be used to determine the contribution of the cascade decay of inelastic $\Psi(2S)$ mesons to the J/Ψ cross sections. On the other hand theoretical predictions in the color singlet model exist, which can be compared to the measurement.

To obtain the cross section ratio, it is utilised that $\Psi(2S)$ mesons also decay directly into two leptons. In all invariant mass distributions of two oppositely charged muons an additional mass peak at the $\Psi(2S)$ meson mass is visible, e.g. in figure 7.16(a) in the elasticity range $0.6 < z < 0.75$.
In order to calculate the cross section ratio, the different branching ratios for the

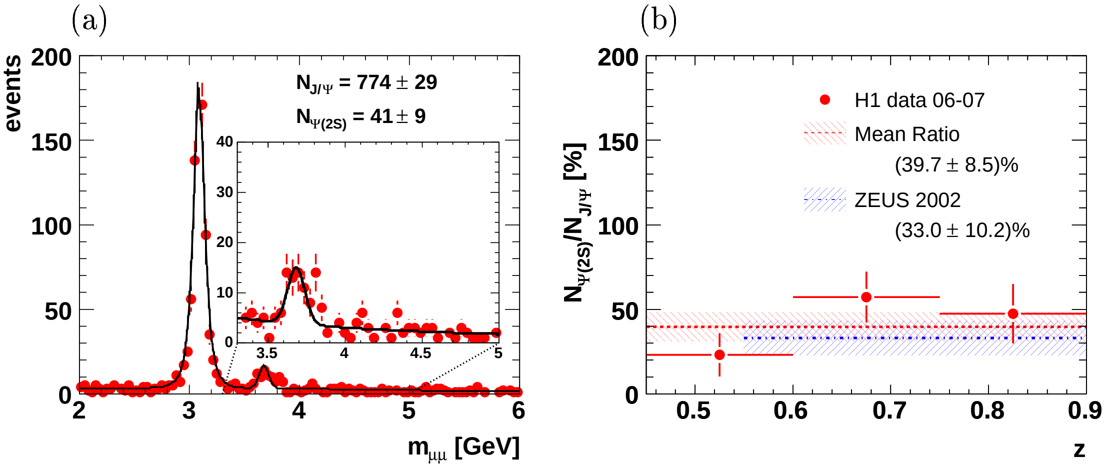
(a) (b)

Figure 7.16: (a) Invariant mass distribution for $\Psi(2S)$ and J/Ψ mesons in the elasticity range $0.6 < z < 0.75$ (the small histogram zooms into the mass region of the $\Psi(2S)$ meson) and (b) the cross section of $\Psi(2S)$ mesons with respect to the J/Ψ cross section as a function of z.

decay channel into muons of J/Ψ and $\Psi(2S)$ mesons and the cascade decay of the $\Psi(2S)$ meson have to be taken into account.
The 'real' numbers of J/Ψ and $\Psi(2S)$ mesons in the data sample are obtained by correcting the number of signal events extracted from the fit with the particular branching ratio

$$N_{J/\Psi} = \frac{N_{J/\Psi,\mathrm{Fit}}}{\mathcal{BR}_{J/\Psi\to\mu\mu}}, \quad \text{with } \mathcal{BR}_{J/\Psi\to\mu\mu} = (5.93 \pm 0.06)\% \tag{7.5}$$

$$N_{\Psi(2S)} = \frac{N_{\Psi(2S),\mathrm{Fit}}}{\mathcal{BR}_{\Psi(2S)\to\mu\mu}}, \quad \text{with } \mathcal{BR}_{\Psi(2S)\to\mu\mu} = (0.75 \pm 0.08)\% \tag{7.6}$$

A large fraction of the decay channels of the $\Psi(2S)$ mesons involves J/Ψ mesons

$$\mathcal{BR}_{\Psi(2S)\to J/\Psi\,+\,X} = (57.4 \pm 0.9)\%. \tag{7.7}$$

These events have to be subtracted from the number of J/Ψ mesons $N_{J/\Psi}$ in order to obtain the number of directly produced J/Ψ mesons. The ratio of the $\Psi(2S)$ and J/Ψ production cross section

$$\frac{\sigma_{\gamma p}^{\Psi(2S)}}{\sigma_{\gamma p}^{J/\Psi}} = \frac{N_{\Psi(2S)}}{N_{J/\Psi} - N_{\Psi(2S)} \cdot \mathcal{BR}_{\Psi(2S)\to J/\Psi\,+\,X}} \tag{7.8}$$

was determined in bins of the elasticity z.
The resulting cross section ratios are shown in figure 7.16(b). At very low values of the elasticity ($z < 0.3$), the uncertainty on the number of J/Ψ and $\Psi(2S)$ mesons rises due to the increasing amount of combinatorial background. The average ratio

is calculated to be

$$\frac{\sigma_{\gamma\mathrm{p}}^{\Psi(2\mathrm{S})}}{\sigma_{\gamma\mathrm{p}}^{\mathrm{J}/\Psi}} = (39.7 \pm 8.5)\% \tag{7.9}$$

which is in good agreement with a measurement from the Zeus collaboration, $\sigma_{\gamma\mathrm{p}}^{\Psi(2\mathrm{S})}/\sigma_{\gamma\mathrm{p}}^{\mathrm{J}/\Psi} = (33.0 \pm 10.2)\,\%$, which was performed in a slightly different kinematic range ($0.55 < \mathrm{z} < 0.9$, $50 < \mathrm{W}_{\gamma p} < 180\,\mathrm{GeV}$) [ZEUS03]. The measured ratio agrees with a leading order calculation in the CSM ($\sigma_{\gamma\mathrm{p}}^{\Psi(2\mathrm{S})}/\sigma_{\gamma\mathrm{p}}^{\mathrm{J}/\Psi} \approx 25\,\%$, [Kra96]) within large uncertainties.

Taking the branching ratio of $\Psi(2\mathrm{S})$ mesons into $\mathrm{J}/\Psi + \mathrm{X}$ into account, a contribution to the inelastic J/Ψ cross sections of $(22.7 \pm 5)\,\%$ is estimated. This is in good agreement with theoretical expectations, which predict a contribution of about 15 % to the measured inelastic J/Ψ cross section [Kra96].

Chapter 8

Electroproduction of J/Ψ mesons

In this chapter a measurement of electroproduction of inelastic J/Ψ mesons is presented. The data sample corresponds to an integrated luminosity of $\mathcal{L} \approx 315\,\mathrm{pb}^{-1}$ and was recorded during the Hera II running period in the years 2004 through 2007. The events were triggered by the subtrigger s61, i.e. by a combination of signals from the backward calorimeter (SpaCal) and the central tracking detector. The J/Ψ mesons are identified via their leptonic decays into muons and electrons respectively. The full data sample contains 702 J/Ψ mesons in the signal peak for the decay channel into muons and 471 mesons for the decay into electrons. Figure 8.1 shows the invariant mass distribution of two oppositely charged muons or electrons. The production cross section of inelastic J/Ψ mesons decreases with the fourth power of the the four momentum transfer. Hence the statistics for the electroproduction analysis is smaller with respect to the photoproduction, although the trigger efficiency is close to $100\,\%$, the whole integrated luminosity of Hera II, and both

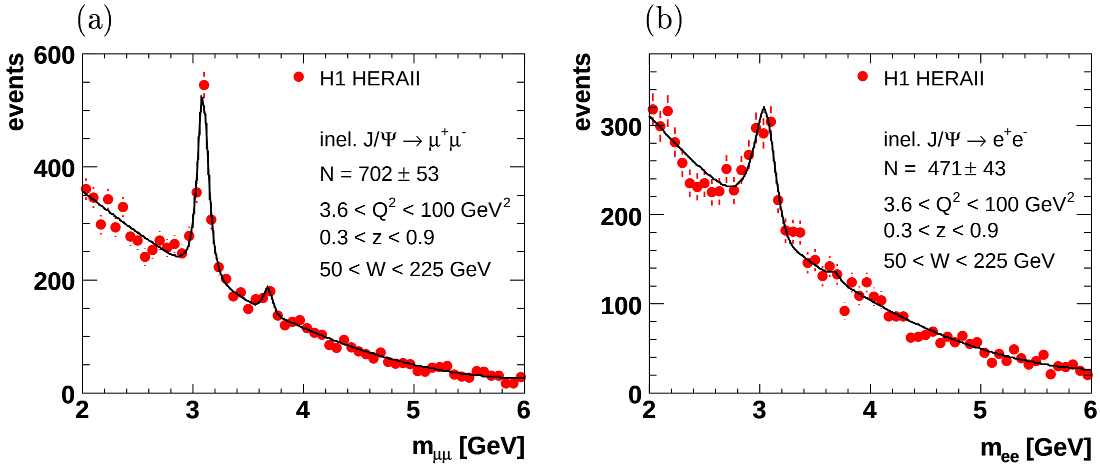

Figure 8.1: Invariant mass distribution of two oppositely charged a) muons and b) electrons in the kinematic range $3.6 \leqslant Q^2 \leqslant 100\,\mathrm{GeV}^2$, $50 \leqslant W_{\gamma p} \leqslant 225\,\mathrm{GeV}$, $0.3 \leqslant z \leqslant 0.9$ and $P^*_{T,\Psi} \geqslant 1\,\mathrm{GeV}$, where $P^*_{T,\Psi}$ denotes the transverse momentum of the J/Ψ in the γp center of mass frame.

leptonic decay channels are used.
In the following section control plots are shown, comparing data with the Monte Carlo simulation. Subsequently the results of the cross section measurement are presented. Afterwards, the sources of systematic uncertainties, which are specific to this sample, are discussed and the polarisation variables are shown.

8.1 Comparison with the Monte Carlo Simulation

In figures 8.2 and 8.3 control plots for the electroproduction analysis are shown. The data (bullets) are background subtracted as explained in section 7.1. The track with the higher transverse momentum is denoted by Trk_1. The distributions are compared to the CASCADE simulation. The Monte Carlo simulation is reweighted in order to achieve the best possible description of the data. The reweighting factors are determined as a function of the photon proton center of mass energy $\mathrm{W}_{\gamma p}$, the transverse momentum of the J/Ψ meson $\mathrm{P}_{\mathrm{T},\Psi}$ in bins of the elasticity z and the four momentum transfer Q^2.

The statistical uncertainties of the data distributions are quite large compared to those of the photoproduction analysis. The slopes of the Q^2 (cf. fig. 8.2(a)) and $\mathrm{P}^{*2}_{\mathrm{T},\Psi}$ (cf. fig. 8.2(c)) distributions are already well modelled by the CASCADE Monte Carlo simulation without reweighting. At large values of $\mathrm{P}^{*2}_{\mathrm{T},\Psi}$, the unweighted simulation is somewhat below the data. At low values of $\mathrm{W}_{\gamma p}$ (cf. fig. 8.2(b)), the CASCADE expectation overshoots the data by a factor of almost two. Meanwhile, the distribution of the elasticity z, shown in figure 8.2(d), is reasonably described. The reweighting has no greater impact on the shape of the elasticity distribution.
The control plots for the momentum of the tracks in figure 8.3(a,b) show a slightly 'harder' slope towards higher P_T in the data distribution, with quite large statistical uncertainties. Figure 8.3(c,d) shows a good agreement of the polar angular distribution of the tracks.

8.2 Cross Section Measurement

The measurement of electroproduction of inelastic J/Ψ mesons is performed using the full data sample collected with the H1 experiment during the HERA II running, which corresponds to an integrated luminosity of $\mathcal{L} \approx 315\ \mathrm{pb}^{-1}$. The analysis is carried out at medium elasticities $(0.3 \leqslant \mathrm{z} \leqslant 0.9)$ in the kinematic range $3.6 \leqslant \mathrm{Q}^2 \leqslant 100\,\mathrm{GeV}^2$, $50 \leqslant \mathrm{W}_{\gamma p} \leqslant 225\,\mathrm{GeV}$ and ${\mathrm{P}^*_{\mathrm{T},\Psi}}^2 \geqslant 1\,\mathrm{GeV}^2$.
The total cross section is measured to be

$$\sigma_{\mathrm{ep}}\,(\mathrm{ep} \rightarrow \mathrm{e}'\mathrm{J}/\Psi\mathrm{X}) \quad = \quad 143.8 \pm 20.0(\mathrm{stat.}) \pm 15.3(\mathrm{syst.})\,\mathrm{pb}. \qquad (8.1)$$

The statistical uncertainty on the total cross section measurement is 13.9 %, the systematic uncertainty is quantified to be 10.9 %. The largest systematic uncertain-

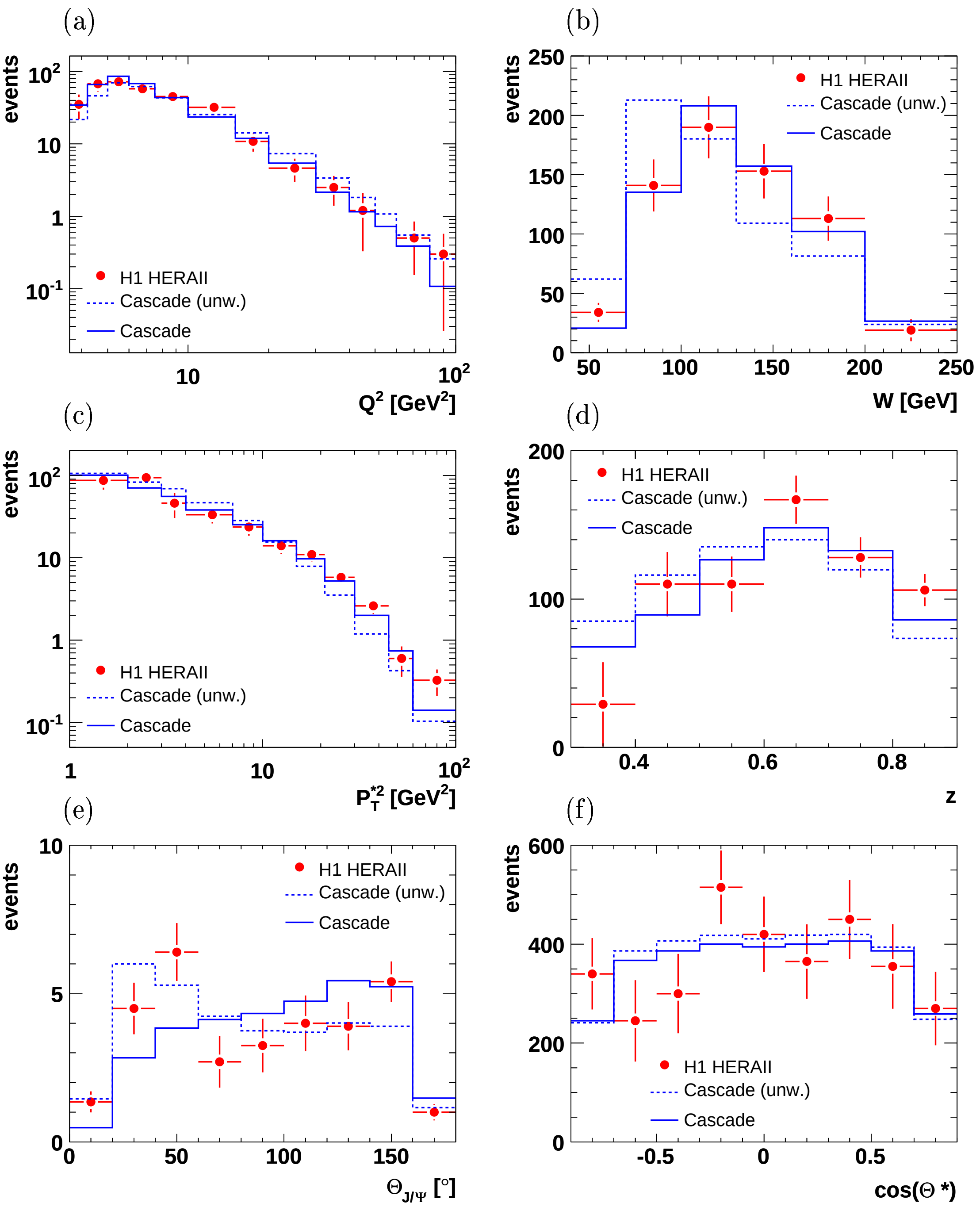

Figure 8.2: Distributions for (a) the four momentum transfer squared Q^2, (b) the photon proton center of mass energy $\mathrm{W}_{\gamma p}$, (c) the transverse momentum of the J/Ψ in the $\gamma\mathrm{p}$ rest frame $\mathrm{P}^*_{\mathrm{T},\Psi}$, (d) the elasticity z, (e) the polar angle of the J/Ψ meson Θ_Ψ and (f) the decay angle $\cos(\Theta^*)$. The data (bullets) are background subtracted and compared with the CASCADE simulation with (solid line) and without (dashed line) reweighting.

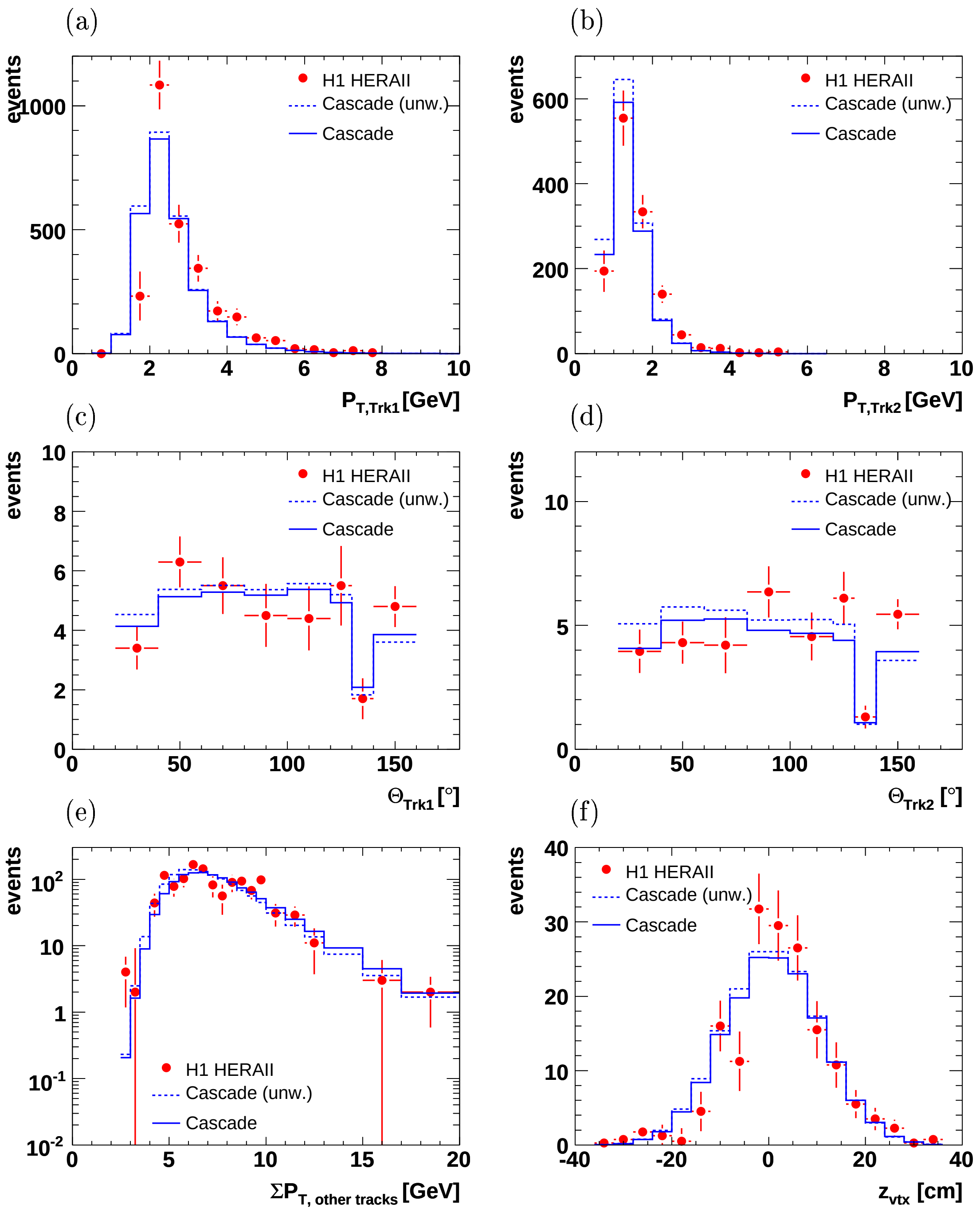

Figure 8.3: Distributions for (a,b) the transverse momentum of the tracks ($P_{T,Trk1} > P_{T,Trk2}$), (c,d) the polar angle of the tracks, (e) the scalar sum of the transverse momenta of all particles except the J/Ψ and (f) the z distribution of the vertex. The data (bullets) are background subtracted and compared with the CASCADE simulation with (solid line) and without (dashed line) reweighting.

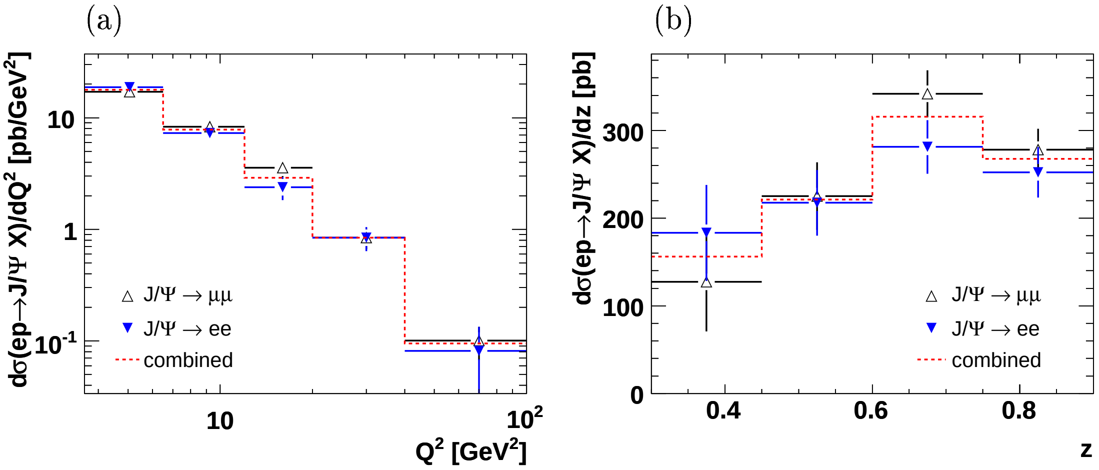

Figure 8.4: Differential cross sections as a function of Q^2 and z for the decay channels into muons (open triangles) and electrons (filled triangles) separately. The dashed line is the resulting cross section after error weighted averaging.

ties arise from the impact of model uncertainties on acceptance and reconstruction efficiency. The systematic uncertainties are explained later on in section 8.3. The measured cross sections are not corrected for contributions of secondary J/Ψ mesons from the decay of B, χ_c or Ψ(2S) mesons.

The differential and double differential cross sections were determined separately for the decay channels into muons and electrons. The cross sections are then combined by error weighted averaging in order to account for the different statistical accuracies of both measurements

$$\sigma_{\text{comb.}} = \frac{\sum\limits_{\text{e},\mu} \frac{\sigma_\ell}{(\Delta\sigma_\ell)^2}}{\sum\limits_{\text{e},\mu} \frac{1}{(\Delta\sigma_\ell)^2}} \pm \sqrt{\frac{1}{\sum\limits_{\text{e},\mu} \frac{1}{(\Delta\sigma_\ell)^2}}}, \tag{8.2}$$

where σ_ℓ and $\Delta\sigma_\ell$ denote the measured cross sections and corresponding errors for the decay channel into muons or electrons respectively. In figure 8.4, the measured cross section as a function of Q^2 and z is shown for the decay channels into muons (open triangles) and electrons (filled triangles). The dashed line corresponds to the combined cross section obtained from the error weighted averaging. In the following, all presented cross sections are combined as described above.

Differential Cross Sections

The measured electroproduction cross sections of inelastic J/Ψ mesons are shown in figures 8.5 and 8.6. Single differential cross sections were measured as a function of the four momentum transfer Q^2, the squared transverse momentum of the J/Ψ

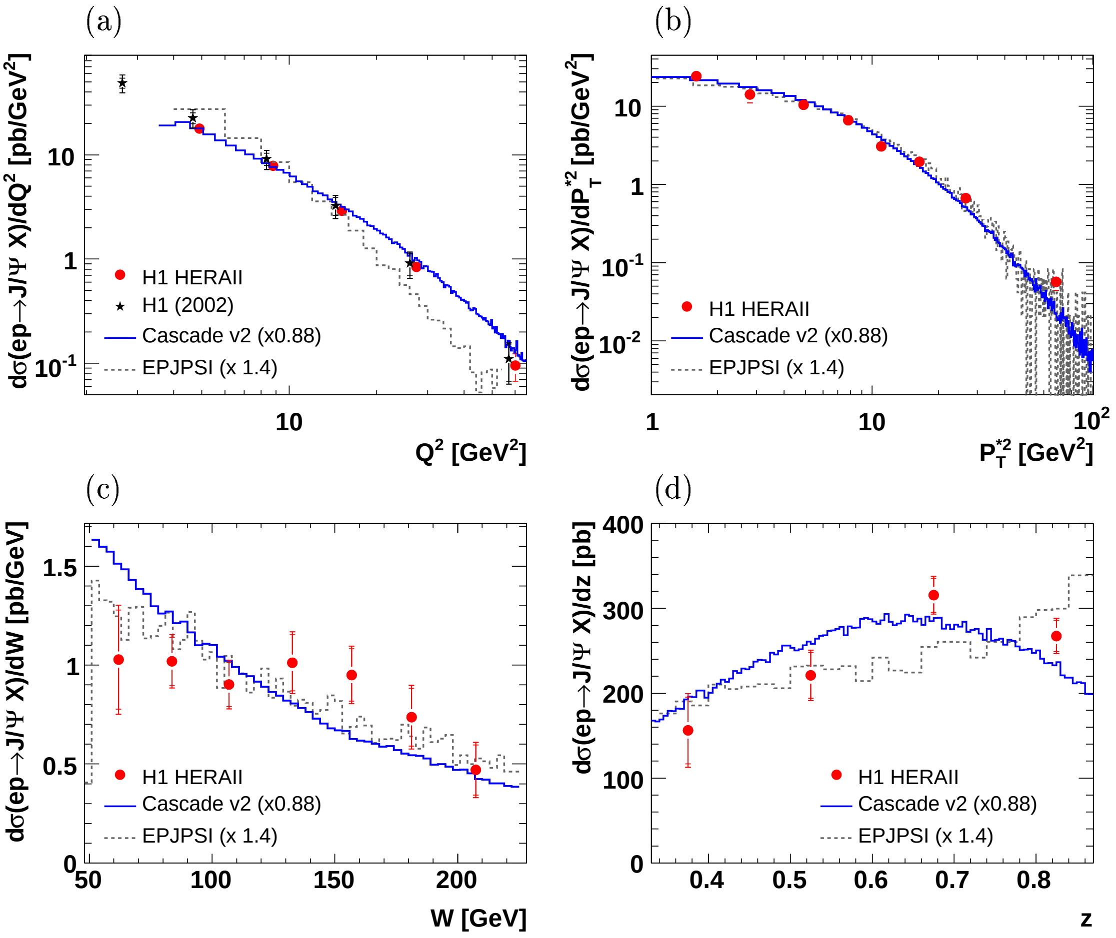

Figure 8.5: Differential cross sections for the electroproduction ($3.6 \leqslant \mathrm{Q}^2 \leqslant 100\,\mathrm{GeV}^2$) of inelastic J/Ψ mesons in the kinematic range $50 \leqslant \mathrm{W}_{\gamma p} \leqslant 225\,\mathrm{GeV}$, $\mathrm{P}^{*2}_{\mathrm{T},\Psi} \geqslant 1\,\mathrm{GeV}^2$ and $0.3 \leqslant \mathrm{z} \leqslant 0.9$ as a function of (a) the four momentum transfer squared Q^2, (b) the squared transverse momentum of the J/Ψ meson in the $\gamma\mathrm{p}$ rest frame $\mathrm{P}^{*2}_{\mathrm{T},\Psi}$, (c) the photon proton center of mass energy $\mathrm{W}_{\gamma p}$ and (d) the elasticity z.

meson in the photon proton rest frame $P^{*2}_{T,\Psi}$, the energy in the photon proton rest frame $W_{\gamma p}$, and the elasticity z.
As a function of the transverse momentum in the photon proton rest frame $P^{*2}_{T,\Psi}$ and the elasticity z, the samples are further investigated by dividing the sample into bins of z and $P^{*}_{T,\Psi}$ respectively.
The data points (bullets) are compared to theoretical predictions of the color singlet model in leading order (CSM LO) as implemented in the Monte Carlo generator CASCADE using k_T factorisation (solid line) and EPJPSI (dashed line) [JS01, Jun92]. The total cross sections of the Monte Carlo simulations are normalised to the total cross section of the measurement. The CASCADE expectation is roughly 10 % too high, while the total cross section predicted by EPJPSI lies about 30 % below.
The cross section as a function of Q^2 (cf. fig. 8.5(a)) is compared to a result from a H1 publication [H102a]. The published analysis and the results presented in this thesis agree to a considerable degree. The lowest bin in Q^2 of the HERA I analysis can not be measured with the HERA II data, due to changes in the SpaCal during the upgrade to HERA II.

The shapes of the cross sections, in particular as a function of the elasticity z in figure 8.5(d), are equal for the photo- and the electroproduction analysis. As in the photoproduction analysis, the CSM LO using k_T factorisation (CASCADE) describes the data quite well, while EPJPSI (CSM LO) fails to describe the data.
The new matrix element implementing the full DIS cross section in CASCADE v2.0.1 [LZ03, BZ03, Bar02], models the slope of the Q^2 dependence, shown in figure 8.5(a), almost perfectly. Predictions in the CSM LO (EPJPSI) predict a much too steep slope as a function of Q^2.
The $P^{*2}_{T,\Psi}$ spectrum is well described by the CASCADE predictions in the overall distribution (cf. fig. 8.5(b)) as well as in bins of the elasticity z (cf. fig. 8.6(a)). In contrast to the photoproduction analysis, the $P^{*}_{T,\Psi}$ spectrum is also reasonably described by the CS LO prediction as implemented in the EPJPSI generator. At large values of $P^{*2}_{T,\Psi}$, both predictions are somewhat below the data. As plotted in figure 8.6(a), this differences arises mainly from the region of large elasticities z.
The $W_{\gamma p}$ distribution shows the same behaviour as in the photoproduction analysis. At low values of $W_{\gamma p}$ CASCADE overshoots the data and falls off too steeply towards larger values of $W_{\gamma p}$

Up to now, no calculations at next to leading order are available for the electroproduction of J/Ψ mesons at HERA, due to unsolved theoretical problems with multiple scales (Q^2, $P_{T,\Psi}$, m_c). Nevertheless, the necessity of higher order corrections, as shown in photoproduction, is confirmed by the electroproduction measurement, since the k_T factorisation approach is again capable of modelling the measured cross sections. No color octet state contributions, as included in the factorisation ansatz in NRQCD, are necessary to describe the data. However, it would be worthwhile to compare the data with NLO calculations in order to prove the importance of next

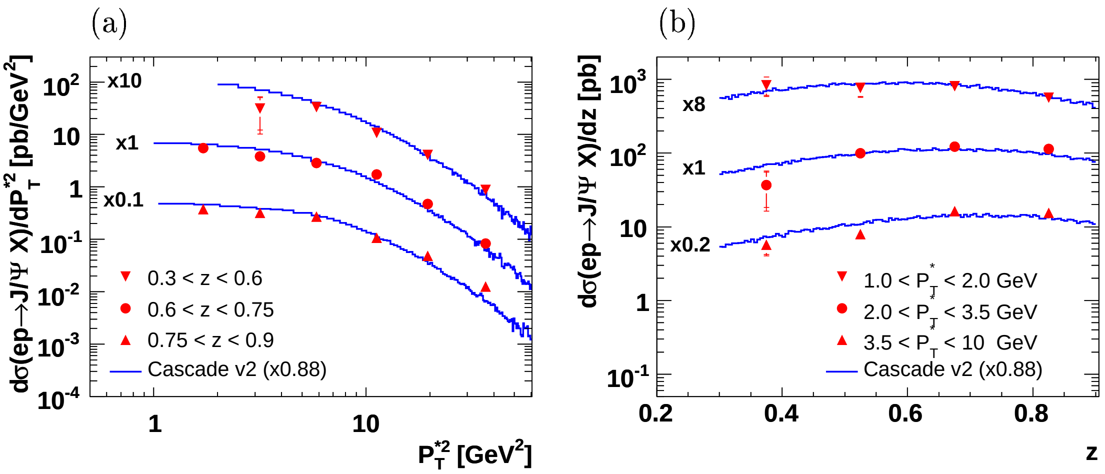

Figure 8.6: Double differential cross sections for the electroproduction ($3.6 \leqslant Q^2 \leqslant 100\,\mathrm{GeV}^2$) of inelastic J/Ψ mesons in the kinematic range $50 \leqslant W_{\gamma p} \leqslant 225\,\mathrm{GeV}$, $P^{*2}_{T,\Psi} \geqslant 1\,\mathrm{GeV}^2$ and $0.3 \leqslant z \leqslant 0.9$ as a function of (a) the squared transverse momentum of the J/Ψ meson in the γp rest frame $P^{*2}_{T,\Psi}$ in bins of z and (b) the elasticity z in bins of $P^{*}_{T,\Psi}$. The cross sections are scaled (factors given next to it) in order to allow a presentation in a single figure.

to leading order contributions in the CSM supplementary to the success of the k_T factorisation approach.

Contributions from Indirectly Produced J/Ψ mesons

Contributions from the decay of higher resonances or B mesons are not subtracted from the measured cross sections. DIFFVM ($\Psi(2S)$) and PYTHIA (B mesons) Monte Carlo simulations have been used to estimate the remaining contributions.
The fraction of events arising from diffractive $\Psi(2S)$ meson production with subsequent decay of the $\Psi(2S)$ into $J/\Psi + X$ is estimated to be 1.5 % in the total sample and about 5 % in the highest z bin. The fraction of events arising from the decay of B mesons is estimated to be 3.6 % in the total sample and about 20 % in the lowest z bin.

8.3 Systematic Uncertainties

In the following the sources of systematic uncertainties, which are not covered in the photoproduction chapter, are described. The impact on the inelastic J/Ψ production cross section of each source was studied in detail. Unless differently specified, the systematic uncertainty for a particular source is taken as the variation of the measured cross section caused by the variation of the variable. The sources of systematic uncertainties for electroproduction analysis are summarised in table 8.1.

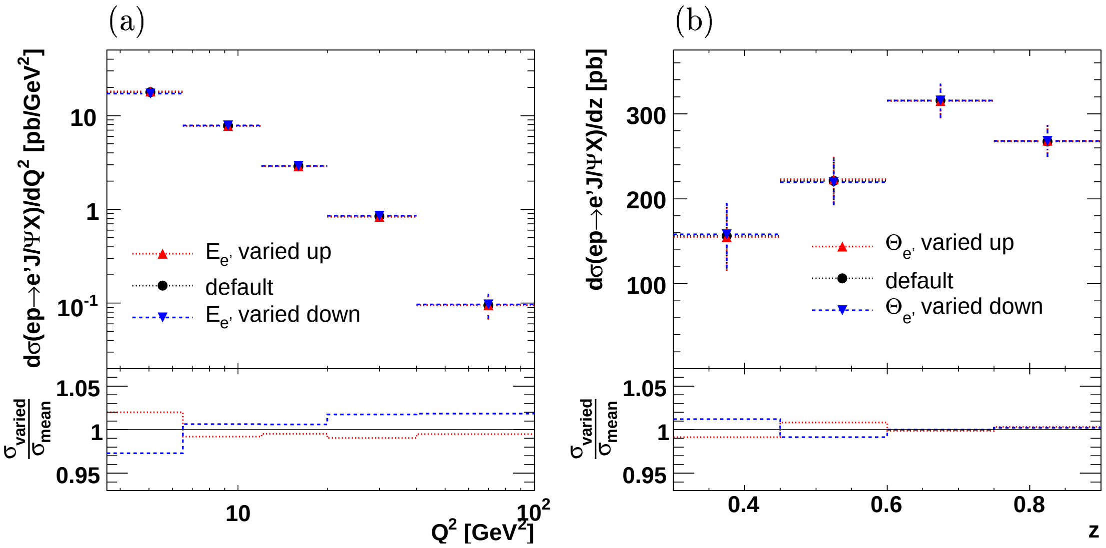

Figure 8.7: Systematic uncertainty arising from the variation of (a) the measured energy of the scattered lepton (1–3 %) and (b) the measured polar angle of the scattered lepton (±1 mrad).

Scattered Lepton

The energy measurement of the scattered lepton in the SpaCal is known to a level of 1 % close to the lepton beam energy ($E_{e'} \approx 27.5\,\mathrm{GeV}$) increasing linearly to 3 % for low energies of the scattered lepton ($E_{e'} \approx 8\,\mathrm{GeV}$).
The uncertainty of the scattering angle is 1 mrad.
Varying the energy of the scattered lepton within this range, leads to an uncertainty of the measured cross section of 2%. The variation of the scattering angle yields an uncertainty of 1 % (cf. fig. 8.7).

Trigger Efficiency

A detailed description of the trigger efficiency can be found in chapter 5 of this thesis. For the electroproduction analysis the trigger efficiency is determined from data to be $\epsilon_{\mathrm{Trigger}} = 97 \pm 2\,\%$. The statistical uncertainty of the trigger efficiency is taken as systematic uncertainty.

Radiative Corrections

For the electroproduction of J/Ψ mesons the measured cross section includes higher order processes. The Born cross section is recovered by applying a correction for initial state photon radiation of the incoming lepton. The uncertainty of the cross section was determined to be 4% [Mey98].

Source		Uncertainty [%]
Reconstruction of scattered lepton:	angle	1
	energy	2
Reconstruction of decay leptons:	track, vertex	4
	identification	5
Number of signal events		3–5
Trigger		2
Model uncertainties	decay angular distribution	5
	(track multiplicity only $z \geqslant 0.75$	8)
Radiative corrections		4
Hadronic energy scale		2
Integrated luminosity		2
Decay branching ratio		1
Sum		10.5–13.5

Table 8.1: Sources of systematic uncertainties taken into account in the electroproduction analysis.

In the electroproduction sample the electron and muon cross section results are combined by weighted averaging. For the combined sample the systematic error of the muon sample, which amounts to 10.5 %, is assigned. The same uncertainties are equally attributed to all bins of the measurement except for the uncertainty of the signal extraction which is 3 % at moderate and large values of z and up to 5 % at small values of z where the combinatorial background is largest.

8.4 J/Ψ Polarisation

As in the photoproduction analysis, the two polarisation variables α and ν are determined by a simultaneous fit to the decay angular distributions $\cos(\Theta^*)$ and ϕ^*, taking only the large statistical uncertainties into account. A measurement of ν in electroproduction is performed for the first time at H1. The distributions of $\cos(\Theta^*)$ and ϕ^* for the medium Q^2 bin ($7.5 \leqslant Q^2 \leqslant 15\,\mathrm{GeV}^2$) are shown in figure 8.8(b). A statistical fluctuation in the lowest bin of $\cos(\Theta^*)$ leads to a very large transverse polarisation, which is still consistent with zero due to the large uncertainties. Figure 8.9 summarises the polarisation variables α and ν for the electroproduction measurement. The polarisation variable α as a function of Q^2 is in good agreement with the result from a previous H1 measurement [H102a]. No predictions for the polarisation of J/Ψ mesons are available for the electroproduction range, however the measurement yields a polarisation similar to those in photoproduction. The measured polarisation is also consistent with unpolarised J/Ψ meson production at HERA within large errors.

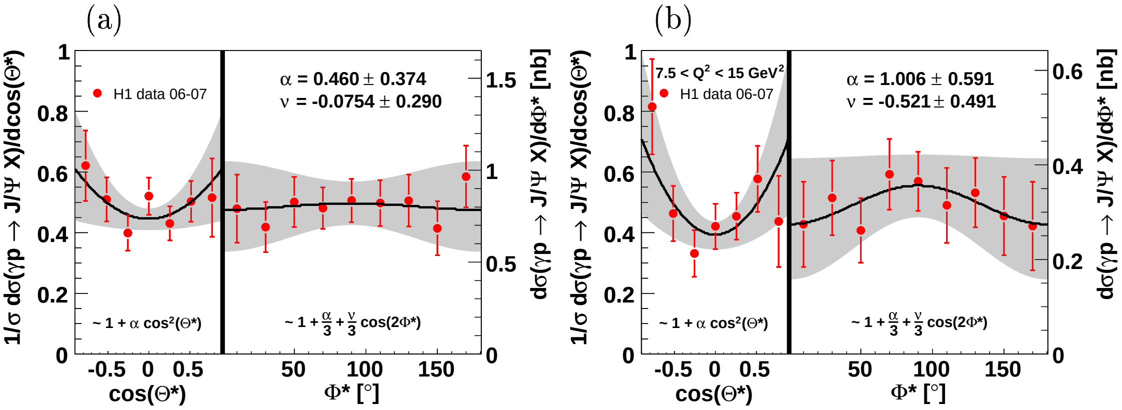

Figure 8.8: Cross sections as a function of the decay angular distributions $\cos(\Theta^*)$ shown in the range $-0.9 \leqslant \cos(\Theta^*) \leqslant 0.9$ and ϕ^* for (a) the overall sample and (b) the medium bin in Q^2 ($7.5 \leqslant Q^2 \leqslant 15\,\mathrm{GeV}^2$). The fit result is drawn as black line, the grey band indicates the 1σ uncertainty of the fit result.

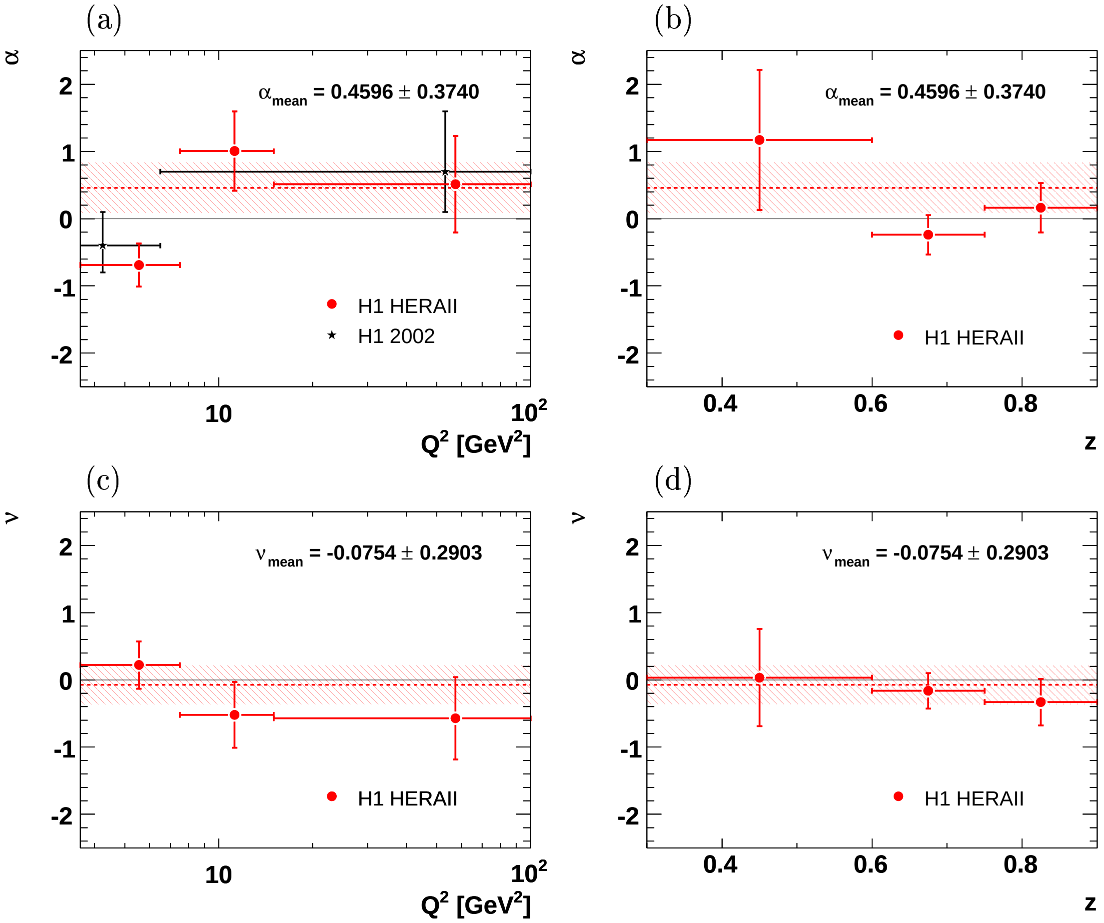

Figure 8.9: Polarisation variables α and ν as a function of the four momentum transfer Q^2 and the elasticity z. The dashed line denotes the values obtained from the full sample, the hatched area corresponds to the error on the average value. The results are compared to a previous H1 measurement of α (stars) [H102a].

CHAPTER 9

Conclusions

This thesis presents new measurements of photoproduction and electroproduction of inelastic J/Ψ mesons at HERA with improved precision compared to previous measurements. The results are in good agreement with measurements from H1 and ZEUS.

The J/Ψ mesons in the electroproduction analysis were identified via their leptonic decays into two electrons or two muons, whereas the trigger setup in the photoproduction sample restricts the analysis to the muonic decay channel.

The photoproduction analysis is carried out in the kinematic range $Q^2 \approx 0\,\text{GeV}^2$, $50 \leqslant W_{\gamma p} \leqslant 225\,\text{GeV}$, $0.3 \leqslant z \leqslant 0.9$ and $P_{T,\Psi} \geqslant 1\,\text{GeV}$ using a data sample recorded with the H1 detector in the years 2006 and 2007 corresponding to an integrated luminosity of $\mathcal{L} \approx 166\ \text{pb}^{-1}$. In the electroproduction analysis the whole HERA II data is analysed ($\mathcal{L} \approx 315\ \text{pb}^{-1}$). The kinematic range of the electroproduction analysis is given by $3.6 \leqslant Q^2 \leqslant 100\,\text{GeV}^2$, $50 \leqslant W_{\gamma p} \leqslant 225\,\text{GeV}$, $0.3 \leqslant z \leqslant 0.9$ and $P^*_{T,\Psi} \geqslant 1\,\text{GeV}$, where $P^*_{T,\Psi}$ denotes the transverse momentum of the J/Ψ in the γp center of mass frame. The integrated luminosity used in the photoproduction analysis is two times larger compared to published H1 analyses, while the integrated luminosity of the electroproduction analysis is increased by a factor of four.

In this thesis, background contributions due to diffractively produced Ψ(2S) mesons decaying into J/Ψ + X are reduced with respect to the previous analyses, since tighter selection cuts are applied. For the comparison of the data with the Monte Carlo simulations, a statistical background subtraction method was used, based on the side bands of the resonance distribution. This results in improved corrections for the simulation and consequently a more accurate description of the data. Finally, the impact of different model assumptions in the Monte Carlo simulation was studied in detail leading to an improved understanding of acceptance corrections and systematic uncertainties.

The measured cross sections are compared to different theoretical predictions in the color singlet model (CSM).

The best description of the data is achieved by the Monte Carlo generator CASCADE

using a k_T factorisation approach in leading order CSM. The off shell calculations of the hard scattering in k_T factorisation implicitly include higher order terms.
The total cross section predicted by the CASCADE generator deviates only a few percent from the measured one. The slopes of the single and double differential cross sections as a function of $P^2_{T,\Psi}$, $P^{*2}_{T,\Psi}$ and Q^2 are very well reproduced. At low values of the elasticity z, the CASCADE expectation overshoots the measured cross section by about 30 % and the cross section as a function of the photon proton effective mass $W_{\gamma p}$ is not well reproduced.
An analytic CSM NLO calculation by Michael Krämer and Peter Zerwas is also able to describe the data, however the errors of this prediction are very large.
NLO contributions are dominated by strong negative contributions at $z \to 1$ and $P_{T,\Psi} \to 0\,\mathrm{GeV}$, leading to a harder $P_{T,\Psi}$ spectrum which is needed in order to describe the data. In addition they increase the total cross section significantly.
Leading order (LO) predictions, as implemented in the Monte Carlo generator EPJPSI, fail to describe the data. The total predicted cross section is too low by 25 % or 40 % respectively.
At large values of the elasticity z, the cross section in the data decreases in both analyses, whereas a continuous rise is predicted in the CSM LO. The slope of the $P^2_{T,\Psi}$ spectrum in photoproduction as well as the slope of Q^2 in electroproduction is much too steep. The predicted cross section at large values of $P^2_{T,\Psi}$ lies almost one order of magnitude below the data, while at low values of $P^2_{T,\Psi}$ it overshoots the data by a factor of two. The predictions from the EPJPSI Monte Carlo generator show the same characteristics as an analytic CSM LO calculation of the cross section as a function of $P^2_{T,\Psi}$ by Michael Krämer.

For the first time at H1, the polarisation variables α and ν are determined by a simultaneous fit to the shapes of the cross sections as a function of $\cos(\Theta^*)$ and ϕ^*. Furthermore this thesis presents the first measurement of the variable ν in electroproduction. The measured polarisation of the J/Ψ meson is in agreement with previous H1 publications and consistent with recent CDF (run II) measurements, where α tends to be small and negative towards large transverse momenta of the J/Ψ mesons.
The polarisation is very well modelled by a k_T factorisation calculation in the CSM which was accomplished by Sergey Baranov. In particular, the trend towards longitudinal polarisation ($\alpha < 0$) as a function of $P_{T,\Psi}$ is predicted by k_T factorisation, whereas calculations in CSM LO and the NRQCD ansatz do not predict any longitudinal polarisation. However, due to large statistical uncertainties of the measurement none of the production models can be excluded, though leading order CSM predictions seem to be disfavoured by the measurements. All models predict a similar polarisation α at low transverse momenta $P_{T,\Psi}$ as well as over the whole analysed elasticity range. Towards large values of $P_{T,\Psi}$, the difference between the models rises continuously. Unfortunately, the statistical error of the measurements becomes large in this kinematic range.

The HERA measurements and recent predictions for the TEVATRON emphasise the necessity to account for higher order corrections in calculations of inelastic J/Ψ meson production. These corrections were unforeseen large.
Up to now, only the k_T factorisation approach provides a well working tool to study inelastic J/Ψ meson production at HERA. However, a more detailed study in the collinear factorisation would be desirable. In order to draw strong conclusions, the uncertainties of the CSM NLO calculations need to be reduced significantly. Furthermore, color singlet calculations at next to leading order need to be performed for the electroproduction of inelastic J/Ψ mesons.
It would be worth to check the impact of higher order corrections on the predicted polarisation. Unfortunately, polarisation predictions are only available at leading order for photoproduction of J/Ψ mesons at HERA.

In conclusion, the presented analyses show that a k_T factorisation approach in the CSM is capable of describing both the measured cross sections and the polarisation very well. The success of k_T factorisation arises from higher order corrections, which are implicitly included due to a resummation to all orders of the unintegrated gluon density. Hence, it is confirmed that higher order contributions are crucial for a proper description of the inelastic J/Ψ meson production.
No indications for color octet state contributions to the inelastic J/Ψ meson production at HERA are visible. Although the results of the polarisation measurement do not exclude the NRQCD predictions, the cross sections are well reproduced by the CSM alone, provided that higher order terms, such as present in the k_T factorisation approach or the full NLO calculation, are included.

APPENDIX A

Photoproduction Cross Section Tables

z	$\langle z \rangle$	$d\sigma_{\mathrm{ep}}/dz$ [nb]	$d\sigma_{\gamma\mathrm{p}}/dz$ [nb]
$0.30 - 0.45$	0.375	2.29 ± 0.14	$22.60 \pm 1.42 \pm 2.60$
$0.45 - 0.60$	0.525	5.09 ± 0.20	$50.32 \pm 2.01 \pm 5.79$
$0.60 - 0.75$	0.675	6.03 ± 0.23	$59.60 \pm 2.24 \pm 6.85$
$0.75 - 0.90$	0.825	5.60 ± 0.30	$55.30 \pm 2.91 \pm 7.74$

Table A.1: Differential cross section for the photoproduction ($Q^2 \approx 0\,\mathrm{GeV}^2$) of inelastic J/Ψ mesons in the kinematic range $60 \leqslant W_{\gamma p} \leqslant 240\,\mathrm{GeV}$, $P_{T,\Psi} \geqslant 1\,\mathrm{GeV}$ and $0.3 \leqslant z \leqslant 0.9$ as a function of the elasticity z. The first error corresponds to the statistical uncertainty, the second denotes the systematic uncertainty.

$W_{\gamma p}$ [GeV]	$\langle W_{\gamma p} \rangle$	σ_{ep} [nb]	$\sigma_{\gamma\mathrm{p}}$ [nb]
$60 - 80$	69.3	0.52 ± 0.076	$19.15 \pm 2.81 \pm 2.20$
$80 - 100$	89.4	0.44 ± 0.045	$25.22 \pm 2.33 \pm 2.90$
$100 - 120$	109.5	0.35 ± 0.028	$24.35 \pm 1.96 \pm 2.80$
$120 - 140$	129.6	0.36 ± 0.027	$32.12 \pm 2.39 \pm 3.69$
$140 - 160$	149.6	0.29 ± 0.022	$32.27 \pm 2.50 \pm 3.71$
$160 - 180$	169.6	0.23 ± 0.021	$31.46 \pm 2.87 \pm 3.62$
$180 - 210$	194.2	0.31 ± 0.030	$37.05 \pm 3.64 \pm 4.26$
$210 - 240$	224.2	0.24 ± 0.033	$37.88 \pm 5.36 \pm 4.36$

Table A.2: Total cross section in bins of $W_{\gamma p}$ for the photoproduction ($Q^2 \approx 0\,\mathrm{GeV}^2$) of inelastic J/Ψ mesons in the kinematic range $60 \leqslant W_{\gamma p} \leqslant 240\,\mathrm{GeV}$, $P_{T,\Psi} \geqslant 1\,\mathrm{GeV}$ and $0.3 \leqslant z \leqslant 0.9$. The first error corresponds to the statistical uncertainty, the second denotes the systematic uncertainty.

$\mathrm{P}^2_{\mathrm{T},\Psi}$ [GeV^2]	$\langle \mathrm{P}^2_{\mathrm{T},\Psi} \rangle$	$\mathrm{d}\sigma_{\mathrm{ep}}/\mathrm{dP}^2_{\mathrm{T},\Psi}[\mathrm{nb}/\mathrm{GeV}^2]$	$\mathrm{d}\sigma_{\gamma \mathrm{p}}/\mathrm{dP}^2_{\mathrm{T},\Psi}[\mathrm{nb}/\mathrm{GeV}^2]$
$1.0 - 2.1$	1.47	0.85 ± 0.046	$8.35 \pm 0.46 \pm 0.96$
$2.1 - 3.5$	2.70	0.44 ± 0.025	$4.31 \pm 0.25 \pm 0.50$
$3.5 - 5.4$	4.31	0.26 ± 0.015	$2.56 \pm 0.15 \pm 0.29$
$5.4 - 7.6$	6.34	0.12 ± 0.0091	$1.16 \pm 0.090 \pm 0.13$
$7.6 - 10.0$	8.63	0.074 ± 0.0062	$0.73 \pm 0.061 \pm 0.084$
$10.0 - 13.5$	11.40	0.041 ± 0.0034	$0.41 \pm 0.033 \pm 0.047$
$13.5 - 20.0$	15.63	0.016 ± 0.0014	$0.16 \pm 0.014 \pm 0.019$
$20.0 - 26.5$	22.13	0.0062 ± 0.00074	$0.061 \pm 0.0073 \pm 0.0071$
$26.5 - 40.0$	30.00	0.0019 ± 0.00029	$0.019 \pm 0.0029 \pm 0.0022$
$40.0 - 60.0$	46.00	0.00059 ± 0.00014	$0.0058 \pm 0.0014 \pm 0.00067$
$60.0 - 100.0$	70.00	0.00013 ± 0.000051	$0.0013 \pm 0.00050 \pm 0.00015$

Table A.3: Differential cross section for the photoproduction ($\mathrm{Q}^2 \approx 0\,\mathrm{GeV}^2$) of inelastic J/Ψ mesons in the kinematic range $60 \leqslant \mathrm{W}_{\gamma p} \leqslant 240\,\mathrm{GeV}$, $\mathrm{P}_{\mathrm{T},\Psi} \geqslant 1\,\mathrm{GeV}$ and $0.3 \leqslant \mathrm{z} \leqslant 0.9$ as a function of the squared transverse momentum of the J/Ψ meson $\mathrm{P}^2_{\mathrm{T},\Psi}$. The first error corresponds to the statistical uncertainty, the second denotes the systematic uncertainty.

$\mathbf{1 \leqslant P_{T,\Psi} \leqslant 2}$ GeV

z	$\langle z \rangle$	$\mathrm{d}\sigma_{\mathrm{ep}}/\mathrm{dz}$ [nb]	$\mathrm{d}\sigma_{\gamma \mathrm{p}}/\mathrm{dz}$ [nb]
$0.30 - 0.45$	0.375	1.32 ± 0.14	$13.03 \pm 1.38 \pm 1.50$
$0.45 - 0.60$	0.525	2.96 ± 0.19	$29.28 \pm 1.88 \pm 3.37$
$0.60 - 0.75$	0.675	3.76 ± 0.21	$37.18 \pm 2.10 \pm 4.28$
$0.75 - 0.90$	0.825	3.30 ± 0.26	$32.58 \pm 2.57 \pm 4.56$

Table A.4: Differential cross section for the photoproduction ($\mathrm{Q}^2 \approx 0\,\mathrm{GeV}^2$) of inelastic J/Ψ mesons in the kinematic range $60 \leqslant \mathrm{W}_{\gamma p} \leqslant 240\,\mathrm{GeV}$, $1 \leqslant \mathrm{P}_{\mathrm{T},\Psi} \leqslant 2\,\mathrm{GeV}$ and $0.3 \leqslant \mathrm{z} \leqslant 0.9$ as a function of the elasticity z. The first error corresponds to the statistical uncertainty, the second denotes the systematic uncertainty.

$\mathbf{2 \leqslant P_{T,\Psi} \leqslant 3}$ GeV

z	$\langle z \rangle$	$\mathrm{d}\sigma_{\mathrm{ep}}/\mathrm{dz}$ [nb]	$\mathrm{d}\sigma_{\gamma \mathrm{p}}/\mathrm{dz}$ [nb]
$0.30 - 0.45$	0.375	0.55 ± 0.066	$5.45 \pm 0.65 \pm 0.63$
$0.45 - 0.60$	0.525	1.21 ± 0.095	$11.91 \pm 0.93 \pm 1.37$
$0.60 - 0.75$	0.675	1.59 ± 0.11	$15.72 \pm 1.13 \pm 1.81$
$0.75 - 0.90$	0.825	1.44 ± 0.15	$14.25 \pm 1.45 \pm 1.99$

Table A.5: Double differential cross section for the photoproduction ($\mathrm{Q}^2 \approx 0\,\mathrm{GeV}^2$) of inelastic J/Ψ mesons in the kinematic range $60 \leqslant \mathrm{W}_{\gamma p} \leqslant 240\,\mathrm{GeV}$, $2 \leqslant \mathrm{P}_{\mathrm{T},\Psi} \leqslant 3\,\mathrm{GeV}$ and $0.3 \leqslant \mathrm{z} \leqslant 0.9$ as a function of the elasticity z. The first error corresponds to the statistical uncertainty, the second denotes the systematic uncertainty.

$3 \leqslant \mathbf{P_{T,\Psi}} \leqslant 4.5$ GeV

z	$\langle z \rangle$	$d\sigma_{ep}/dz$ [nb]	$d\sigma_{\gamma p}/dz$ [nb]
$0.30 - 0.45$	0.375	0.23 ± 0.031	$2.28 \pm 0.31 \pm 0.26$
$0.45 - 0.60$	0.525	0.66 ± 0.052	$6.52 \pm 0.51 \pm 0.75$
$0.60 - 0.75$	0.675	0.64 ± 0.054	$6.33 \pm 0.53 \pm 0.73$
$0.75 - 0.90$	0.825	0.56 ± 0.069	$5.52 \pm 0.68 \pm 0.77$

Table A.6: Double differential cross section for the photoproduction ($Q^2 \approx 0\,\mathrm{GeV}^2$) of inelastic J/Ψ mesons in the kinematic range $60 \leqslant W_{\gamma p} \leqslant 240\,\mathrm{GeV}$, $3 \leqslant P_{T,\Psi} \leqslant 4.5\,\mathrm{GeV}$ and $0.3 \leqslant z \leqslant 0.9$ as a function of the elasticity z. The first error corresponds to the statistical uncertainty, the second denotes the systematic uncertainty.

$\mathbf{P_{T,\Psi}} \geqslant 4.5$ GeV

z	$\langle z \rangle$	$d\sigma_{ep}/dz$ [nb]	$d\sigma_{\gamma p}/dz$ [nb]
$0.30 - 0.45$	0.375	0.11 ± 0.016	$1.10 \pm 0.16 \pm 0.13$
$0.45 - 0.60$	0.525	0.16 ± 0.020	$1.59 \pm 0.19 \pm 0.18$
$0.60 - 0.75$	0.675	0.14 ± 0.018	$1.41 \pm 0.18 \pm 0.16$
$0.75 - 0.90$	0.825	0.17 ± 0.025	$1.66 \pm 0.25 \pm 0.23$

Table A.7: Double differential cross section for the photoproduction ($Q^2 \approx 0\,\mathrm{GeV}^2$) of inelastic J/Ψ mesons in the kinematic range $60 \leqslant W_{\gamma p} \leqslant 240\,\mathrm{GeV}$, $P_{T,\Psi} \geqslant 4.5\,\mathrm{GeV}$ and $0.3 \leqslant z \leqslant 0.9$ as a function of the elasticity z. The first error corresponds to the statistical uncertainty, the second denotes the systematic uncertainty.

$0.30 \leqslant \mathbf{z} \leqslant 0.45$

$P^2_{T,\Psi}$ [GeV^2]	$\langle P^2_{T,\Psi} \rangle$	$d\sigma_{ep}/dP^2_{T,\Psi}$[nb/GeV^2]		$d\sigma_{\gamma p}/dP^2_{T,\Psi}$[nb/GeV^2]		
$1.0 - 2.0$	1.44	0.096	$\pm$ 0.017	0.95	$\pm$ 0.17	$\pm$ 0.11
$2.0 - 3.0$	2.45	0.058	$\pm$ 0.011	0.58	$\pm$ 0.11	$\pm$ 0.067
$3.0 - 4.5$	3.64	0.035	$\pm$ 0.0060	0.35	$\pm$ 0.060	$\pm$ 0.040
$4.5 - 7.0$	5.51	0.021	$\pm$ 0.0033	0.20	$\pm$ 0.032	$\pm$ 0.023
$7.0 - 10.0$	8.24	0.0092	$\pm$ 0.0018	0.091	$\pm$ 0.018	$\pm$ 0.010
$10.0 - 14.0$	11.61	0.0040	$\pm$ 0.00086	0.040	$\pm$ 0.0084	$\pm$ 0.0046
$14.0 - 20.0$	16.21	0.0019	$\pm$ 0.00041	0.019	$\pm$ 0.0041	$\pm$ 0.0021
$20.0 - 40.0$	25.00	0.00055	$\pm$ 0.00014	0.0054	$\pm$ 0.0014	$\pm$ 0.00062
$40.0 - 100.0$	49.00	0.000085	$\pm$ 0.000041	0.00084	$\pm$ 0.00041	$\pm$ 0.000097

Table A.8: Differential cross section for the photoproduction ($Q^2 \approx 0\,\mathrm{GeV}^2$) of inelastic J/Ψ mesons in the kinematic range $60 \leqslant W_{\gamma p} \leqslant 240\,\mathrm{GeV}$, $P_{T,\Psi} \geqslant 1\,\mathrm{GeV}$ and $0.3 \leqslant z \leqslant 0.45$ as a function of the squared transverse momentum of the J/Ψ meson $P^2_{T,\Psi}$. The first error corresponds to the statistical uncertainty, the second denotes the systematic uncertainty.

$\mathbf{0.45 \leqslant z \leqslant 0.60}$

$\mathrm{P}^2_{\mathrm{T},\Psi}$ [GeV^2]	$\langle \mathrm{P}^2_{\mathrm{T},\Psi} \rangle$	$\mathrm{d}\sigma_{\mathrm{ep}}/\mathrm{dP}^2_{\mathrm{T},\Psi}$[nb/GeV^2]		$\mathrm{d}\sigma_{\gamma\mathrm{p}}/\mathrm{dP}^2_{\mathrm{T},\Psi}$[nb/GeV^2]		
1.0 − 2.0	1.44	0.22	± 0.023	2.18	± 0.22	± 0.25
2.0 − 3.0	2.45	0.14	± 0.015	1.36	± 0.15	± 0.16
3.0 − 4.5	3.64	0.077	± 0.0088	0.76	± 0.087	± 0.087
4.5 − 7.0	5.51	0.040	± 0.0044	0.39	± 0.044	± 0.045
7.0 − 10.0	8.24	0.023	± 0.0028	0.23	± 0.028	± 0.027
10.0 − 14.0	11.61	0.011	± 0.0015	0.11	± 0.014	± 0.012
14.0 − 20.0	16.21	0.0056	± 0.00078	0.055	± 0.0077	± 0.0063
20.0 − 40.0	25.00	0.00090	± 0.00017	0.0089	± 0.0017	± 0.0010
40.0 − 100.0	49.00	0.00010	± 0.000047	0.0010	± 0.00046	± 0.00012

Table A.9: Differential cross section for the photoproduction ($\mathrm{Q}^2 \approx 0\,\mathrm{GeV}^2$) of inelastic J/Ψ mesons in the kinematic range $60 \leqslant \mathrm{W}_{\gamma p} \leqslant 240\,\mathrm{GeV}$, $\mathrm{P}_{\mathrm{T},\Psi} \geqslant 1\,\mathrm{GeV}$ and $0.45 \leqslant \mathrm{z} \leqslant 0.60$ as a function of the squared transverse momentum of the J/Ψ meson $\mathrm{P}^2_{\mathrm{T},\Psi}$. The first error corresponds to the statistical uncertainty, the second denotes the systematic uncertainty.

$\mathbf{0.60 \leqslant z \leqslant 0.75}$

$\mathrm{P}^2_{\mathrm{T},\Psi}$ [GeV^2]	$\langle \mathrm{P}^2_{\mathrm{T},\Psi} \rangle$	$\mathrm{d}\sigma_{\mathrm{ep}}/\mathrm{dP}^2_{\mathrm{T},\Psi}$[nb/GeV^2]		$\mathrm{d}\sigma_{\gamma\mathrm{p}}/\mathrm{dP}^2_{\mathrm{T},\Psi}$[nb/GeV^2]		
1.0 − 2.0	1.44	0.28	± 0.025	2.80	± 0.25	± 0.32
2.0 − 3.0	2.45	0.16	± 0.017	1.55	± 0.17	± 0.18
3.0 − 4.5	3.64	0.11	± 0.011	1.11	± 0.11	± 0.13
4.5 − 7.0	5.51	0.054	± 0.0056	0.53	± 0.056	± 0.061
7.0 − 10.0	8.24	0.024	± 0.0030	0.24	± 0.029	± 0.027
10.0 − 14.0	11.61	0.013	± 0.0017	0.13	± 0.016	± 0.015
14.0 − 20.0	16.21	0.0051	± 0.00077	0.050	± 0.0076	± 0.0058
20.0 − 40.0	25.00	0.00086	± 0.00017	0.0085	± 0.0017	± 0.00098
40.0 − 100.0	49.00	0.000058	± 0.000030	0.00057	± 0.00030	± 0.000065

Table A.10: Differential cross section for the photoproduction ($\mathrm{Q}^2 \approx 0\,\mathrm{GeV}^2$) of inelastic J/Ψ mesons in the kinematic range $60 \leqslant \mathrm{W}_{\gamma p} \leqslant 240\,\mathrm{GeV}$, $\mathrm{P}_{\mathrm{T},\Psi} \geqslant 1\,\mathrm{GeV}$ and $0.60 \leqslant \mathrm{z} \leqslant 0.75$ as a function of the squared transverse momentum of the J/Ψ meson $\mathrm{P}^2_{\mathrm{T},\Psi}$. The first error corresponds to the statistical uncertainty, the second denotes the systematic uncertainty.

$\mathbf{0.75 \leqslant z \leqslant 0.90}$

$P^2_{T,\Psi}$ [GeV^2]	$\langle P^2_{T,\Psi} \rangle$	$d\sigma_{ep}/dP^2_{T,\Psi}$[nb/GeV^2]		$d\sigma_{\gamma p}/dP^2_{T,\Psi}$[nb/GeV^2]		
$1.0 - 2.0$	1.44	0.25	± 0.030	2.50	± 0.30	± 0.35
$2.0 - 3.0$	2.45	0.16	± 0.022	1.56	± 0.21	± 0.22
$3.0 - 4.5$	3.64	0.086	± 0.013	0.85	± 0.13	± 0.12
$4.5 - 7.0$	5.51	0.056	± 0.0054	0.55	± 0.053	± 0.077
$7.0 - 10.0$	8.24	0.020	± 0.0036	0.19	± 0.036	± 0.027
$10.0 - 14.0$	11.61	0.012	± 0.0023	0.12	± 0.023	± 0.017
$14.0 - 20.0$	16.21	0.0034	± 0.00088	0.034	± 0.0087	± 0.0048
$20.0 - 40.0$	25.00	0.0011	± 0.00029	0.011	± 0.0029	± 0.0015

Table A.11: Differential cross section for the photoproduction ($Q^2 \approx 0\,\mathrm{GeV}^2$) of inelastic J/Ψ mesons in the kinematic range $60 \leqslant W_{\gamma p} \leqslant 240\,\mathrm{GeV}$, $P_{T,\Psi} \geqslant 1\,\mathrm{GeV}$ and $0.75 \leqslant z \leqslant 0.90$ as a function of the squared transverse momentum of the J/Ψ meson $P^2_{T,\Psi}$. The first error corresponds to the statistical uncertainty, the second denotes the systematic uncertainty.

Appendix B

Electroproduction Cross Section Tables

Q^2 [GeV^2]	$\langle Q^2 \rangle$	$d\sigma_{ep}/dQ^2$ [pb/GeV^2]		
3.6 – 6.5	4.85	17.84	± 1.94	± 1.94
6.5 – 12.0	8.63	7.83	± 0.71	± 0.85
12.0 – 20.0	15.01	2.90	± 0.42	± 0.321
20.0 – 40.0	26.67	0.84	± 0.13	± 0.092
40.0 – 100.0	53.00	0.095	± 0.028	± 0.010

Table B.1: Differential cross section for the electroproduction ($3.6 \leqslant Q^2 \leqslant 100\,\mathrm{GeV}^2$) of inelastic J/Ψ mesons in the kinematic range $50 \leqslant W_{\gamma p} \leqslant 225\,\mathrm{GeV}$, $P^*_{T,\Psi} \geqslant 1\,\mathrm{GeV}$ and $0.3 \leqslant z \leqslant 0.9$ as a function of the photon virtuality Q^2. The first error corresponds to the statistical uncertainty, the second denotes the systematic uncertainty.

$P^{*2}_{T,\Psi}$ [GeV^2]	$\langle P^{*2}_{T,\Psi} \rangle$	$d\sigma_{ep}/dP^{*2}_{T,\Psi}$ [pb/GeV^2]		
$1.0 - 2.2$	1.57	24.10	± 3.86	± 2.63
$2.2 - 3.7$	2.90	14.13	± 2.81	± 1.54
$3.7 - 6.4$	4.88	10.40	± 1.63	± 1.13
$6.4 - 9.6$	7.77	6.58	± 0.95	± 0.72
$9.6 - 13.5$	11.24	3.06	± 0.51	± 0.33
$13.5 - 20.0$	16.01	1.94	± 0.26	± 0.21
$20.0 - 40.0$	25.67	0.67	± 0.071	± 0.073
$40.0 - 100.0$	51.00	0.057	± 0.011	± 0.0062

Table B.2: Differential cross section for the electroproduction ($3.6 \leqslant Q^2 \leqslant 100\,\mathrm{GeV}^2$) of inelastic J/Ψ mesons in the kinematic range $50 \leqslant W_{\gamma p} \leqslant 225\,\mathrm{GeV}$, $P^{*}_{T,\Psi} \geqslant 1\,\mathrm{GeV}$ and $0.3 \leqslant z \leqslant 0.9$ as a function of the squared transverse momentum of the J/Ψ meson in the photon proton rest frame $P^{*2}_{T,\Psi}$. The first error corresponds to the statistical uncertainty, the second denotes the systematic uncertainty.

$W_{\gamma p}$ [GeV]	$\langle W_{\gamma p} \rangle$	$d\sigma_{ep}/dW_{\gamma p}$ [pb/GeV]		
$50 - 70$	58.0	1.03	± 0.25	± 0.11
$70 - 95$	81.8	1.02	± 0.12	± 0.11
$95 - 120$	106.7	0.90	± 0.11	± 0.10
$120 - 145$	131.8	1.01	± 0.14	± 0.11
$145 - 170$	156.8	0.95	± 0.13	± 0.10
$170 - 195$	181.9	0.74	± 0.15	± 0.080
$195 - 225$	209.1	0.47	± 0.13	± 0.051

Table B.3: Differential cross section for the electroproduction ($3.6 \leqslant Q^2 \leqslant 100\,\mathrm{GeV}^2$) of inelastic J/Ψ mesons in the kinematic range $50 \leqslant W_{\gamma p} \leqslant 225\,\mathrm{GeV}$, $P^{*}_{T,\Psi} \geqslant 1\,\mathrm{GeV}$ and $0.3 \leqslant z \leqslant 0.9$ as a function of the photon proton center of mass energy $W_{\gamma p}$. The first error corresponds to the statistical uncertainty, the second denotes the systematic uncertainty.

z	$\langle z \rangle$	$d\sigma_{ep}/dz$ [pb]		
$0.30 - 0.45$	0.375	156.17	± 39.36	± 17.76
$0.45 - 0.60$	0.525	221.18	± 26.94	± 24.61
$0.60 - 0.75$	0.675	315.55	± 20.17	± 34.32
$0.75 - 0.90$	0.825	267.52	± 18.42	± 36.12

Table B.4: Differential cross section for the electroproduction ($3.6 \leqslant Q^2 \leqslant 100\,\mathrm{GeV}^2$) of inelastic J/Ψ mesons in the kinematic range $50 \leqslant W_{\gamma p} \leqslant 225\,\mathrm{GeV}$, $P^{*}_{T,\Psi} \geqslant 1\,\mathrm{GeV}$ and $0.3 \leqslant z \leqslant 0.9$ as a function of the elasticity z. The first error corresponds to the statistical uncertainty, the second denotes the systematic uncertainty.

$\mathbf{0.3 \leqslant z \leqslant 0.6}$

$P^{*2}_{T,\Psi}$ [GeV^2]	$\langle P^{*2}_{T,\Psi} \rangle$	$d\sigma_{ep}/dP^{*2}_{T,\Psi}$ [pb/GeV^2]
$2.5 - 4.0$	3.18	$3.13 \pm 1.91 \pm 0.34$
$4.0 - 8.0$	5.58	$3.31 \pm 0.89 \pm 0.36$
$8.0 - 15.0$	10.46	$1.07 \pm 0.28 \pm 0.12$
$15.0 - 25.0$	18.50	$0.41 \pm 0.10 \pm 0.044$
$25.0 - 60.0$	32.00	$0.088 \pm 0.021 \pm 0.0095$

Table B.5: Differential cross section for the electroproduction ($3.6 \leqslant Q^2 \leqslant 100\,\mathrm{GeV}^2$) of inelastic J/Ψ mesons in the kinematic range $50 \leqslant W_{\gamma p} \leqslant 225\,\mathrm{GeV}$, $P^{*}_{T,\Psi} \geqslant 1\,\mathrm{GeV}$ and $0.3 \leqslant z \leqslant 0.6$ as a function of the squared transverse momentum of the J/Ψ meson in the photon proton rest frame $P^{*2}_{T,\Psi}$. The first error corresponds to the statistical uncertainty, the second denotes the systematic uncertainty.

$\mathbf{0.6 \leqslant z \leqslant 0.75}$

$P^{*2}_{T,\Psi}$ [GeV^2]	$\langle P^{*2}_{T,\Psi} \rangle$	$d\sigma_{ep}/dP^{*2}_{T,\Psi}$ [pb/GeV^2]
$1.0 - 2.5$	1.70	$5.50 \pm 0.97 \pm 0.60$
$2.5 - 4.0$	3.20	$3.81 \pm 0.82 \pm 0.42$
$4.0 - 8.0$	5.65	$2.85 \pm 0.42 \pm 0.31$
$8.0 - 15.0$	10.54	$1.71 \pm 0.21 \pm 0.19$
$15.0 - 25.0$	18.47	$0.47 \pm 0.078 \pm 0.051$
$25.0 - 60.0$	33.00	$0.083 \pm 0.018 \pm 0.0091$

Table B.6: Differential cross section for the electroproduction ($3.6 \leqslant Q^2 \leqslant 100\,\mathrm{GeV}^2$) of inelastic J/Ψ mesons in the kinematic range $50 \leqslant W_{\gamma p} \leqslant 225\,\mathrm{GeV}$, $P^{*}_{T,\Psi} \geqslant 1\,\mathrm{GeV}$ and $0.6 \leqslant z \leqslant 0.75$ as a function of the squared transverse momentum of the J/Ψ meson in the photon proton rest frame $P^{*2}_{T,\Psi}$. The first error corresponds to the statistical uncertainty, the second denotes the systematic uncertainty.

$\mathbf{0.75 \leqslant z \leqslant 0.9}$

$P^{*2}_{T,\Psi}$ [GeV^2]	$\langle P^{*2}_{T,\Psi} \rangle$	$d\sigma_{ep}/dP^{*2}_{T,\Psi}$ [pb/GeV^2]
$1.0 - 2.5$	1.71	$3.74 \pm 0.76 \pm 0.50$
$2.5 - 4.0$	3.21	$3.18 \pm 0.73 \pm 0.43$
$4.0 - 8.0$	5.71	$2.71 \pm 0.40 \pm 0.37$
$8.0 - 15.0$	10.63	$1.07 \pm 0.18 \pm 0.14$
$15.0 - 25.0$	18.40	$0.48 \pm 0.081 \pm 0.065$
$25.0 - 60.0$	33.00	$0.13 \pm 0.022 \pm 0.018$

Table B.7: Differential cross section for the electroproduction ($3.6 \leqslant Q^2 \leqslant 100\,\mathrm{GeV}^2$) of inelastic J/Ψ mesons in the kinematic range $50 \leqslant W_{\gamma p} \leqslant 225\,\mathrm{GeV}$, $P^{*}_{T,\Psi} \geqslant 1\,\mathrm{GeV}$ and $0.75 \leqslant z \leqslant 0.9$ as a function of the squared transverse momentum of the J/Ψ meson in the photon proton rest frame $P^{*2}_{T,\Psi}$. The first error corresponds to the statistical uncertainty, the second denotes the systematic uncertainty.

$1 \leqslant P^*_{T,\Psi} \leqslant 2$ GeV

z	$\langle z \rangle$	$d\sigma_{ep}/dz$ [pb]
0.30 − 0.45	0.375	103.65 ± 27.86 ± 11.79
0.45 − 0.60	0.525	95.06 ± 22.01 ± 10.58
0.60 − 0.75	0.675	100.74 ± 13.32 ± 10.96
0.75 − 0.90	0.825	70.49 ± 10.49 ± 9.52

Table B.8: Differential cross section for the electroproduction ($3.6 \leqslant Q^2 \leqslant 100\,\mathrm{GeV}^2$) of inelastic J/Ψ mesons in the kinematic range $50 \leqslant W_{\gamma p} \leqslant 225\,\mathrm{GeV}$, $1 \leqslant P^*_{T,\Psi} \leqslant 2\,\mathrm{GeV}$ and $0.3 \leqslant z \leqslant 0.9$ as a function of the elasticity z. The first error corresponds to the statistical uncertainty, the second denotes the systematic uncertainty.

$2 \leqslant P^*_{T,\Psi} \leqslant 3.5$ GeV

z	$\langle z \rangle$	$d\sigma_{ep}/dz$ [pb]
0.30 − 0.45	0.375	36.64 ± 18.41 ± 4.17
0.45 − 0.60	0.525	99.60 ± 18.68 ± 11.08
0.60 − 0.75	0.675	121.74 ± 12.99 ± 13.23
0.75 − 0.90	0.825	113.49 ± 12.98 ± 15.32

Table B.9: Differential cross section for the electroproduction ($3.6 \leqslant Q^2 \leqslant 100\,\mathrm{GeV}^2$) of inelastic J/Ψ mesons in the kinematic range $50 \leqslant W_{\gamma p} \leqslant 225\,\mathrm{GeV}$, $2 \leqslant P^*_{T,\Psi} \leqslant 3.5\,\mathrm{GeV}$ and $0.3 \leqslant z \leqslant 0.9$ as a function of the elasticity z. The first error corresponds to the statistical uncertainty, the second denotes the systematic uncertainty.

$3.5 \leqslant P^*_{T,\Psi} \leqslant 10$ GeV

z	$\langle z \rangle$	$d\sigma_{ep}/dz$ [pb]
0.30 − 0.45	0.375	28.66 ± 7.62 ± 3.26
0.45 − 0.60	0.525	39.79 ± 7.78 ± 4.43
0.60 − 0.75	0.675	81.15 ± 8.16 ± 8.82
0.75 − 0.90	0.825	77.03 ± 8.13± 10.40

Table B.10: Differential cross section for the electroproduction ($3.6 \leqslant Q^2 \leqslant 100\,\mathrm{GeV}^2$) of inelastic J/Ψ mesons in the kinematic range $50 \leqslant W_{\gamma p} \leqslant 225\,\mathrm{GeV}$, $3.5 \leqslant P^*_{T,\Psi} \leqslant 10\,\mathrm{GeV}$ and $0.3 \leqslant z \leqslant 0.9$ as a function of the elasticity z. The first error corresponds to the statistical uncertainty, the second denotes the systematic uncertainty.

Appendix C

J/Ψ Polarisation Tables

z	⟨z⟩	α	ν
0.30 − 0.90	0.600	0.007 ± 0.120	−0.049 ± 0.154
0.30 − 0.45	0.375	−0.346 ± 0.274	−0.147 ± 0.335
0.45 − 0.60	0.525	0.340 ± 0.243	0.013 ± 0.286
0.60 − 0.75	0.675	−0.064 ± 0.181	0.025 ± 0.259
0.75 − 0.90	0.825	0.142 ± 0.285	−0.319 ± 0.396

Table C.1: Polarisation variables α and ν for the photoproduction ($Q^2 \approx 0\,\mathrm{GeV}^2$) of inelastic J/Ψ mesons in the kinematic range $60 \leqslant W_{\gamma p} \leqslant 240\,\mathrm{GeV}$, $P_{T,\Psi} \geqslant 1\,\mathrm{GeV}$ and $0.3 \leqslant z \leqslant 0.9$ as a function of the elasticity z.

$P_{T,\Psi}$ [GeV]	$\langle P_{T,\Psi} \rangle$	α	ν
1.0 − 100.0	6.00	0.007 ± 0.120	−0.049 ± 0.154
1.0 − 2.0	1.45	0.166 ± 0.217	0.359 ± 0.242
2.0 − 3.0	2.46	−0.108 ± 0.217	−0.825 ± 0.353
3.0 − 4.5	3.65	−0.042 ± 0.238	−0.469 ± 0.380
4.5 − 10.0	6.21	−0.333 ± 0.261	−0.319 ± 0.396

Table C.2: Polarisation variables α and ν for the photoproduction ($Q^2 \approx 0\,\mathrm{GeV}^2$) of inelastic J/Ψ mesons in the kinematic range $60 \leqslant W_{\gamma p} \leqslant 240\,\mathrm{GeV}$, $P_{T,\Psi} \geqslant 1\,\mathrm{GeV}$ and $0.3 \leqslant z \leqslant 0.9$ as a function of the transverse momentum of the J/Ψ meson.

z	$\langle z \rangle$	α	ν
$0.30 - 0.90$	0.600	0.460 ± 0.374	-0.075 ± 0.290
$0.30 - 0.60$	0.450	1.170 ± 1.043	0.034 ± 0.724
$0.60 - 0.75$	0.675	-0.239 ± 0.294	-0.164 ± 0.263
$0.75 - 0.90$	0.825	0.161 ± 0.368	-0.331 ± 0.347

Table C.3: Polarisation variables α and ν for the electroproduction ($3.6 \leqslant Q^2 \leqslant 100\,\mathrm{GeV}^2$) of inelastic J/Ψ mesons in the kinematic range $50 \leqslant W_{\gamma p} \leqslant 225\,\mathrm{GeV}$, $P^*_{T,\Psi} \geqslant 1\,\mathrm{GeV}$ and $0.3 \leqslant z \leqslant 0.9$ as a function of the elasticity z.

Q^2 [GeV^2]	$\langle Q^2 \rangle$	α	ν
$3.6 - 100.0$	16.00	0.460 ± 0.374	-0.075 ± 0.290
$3.6 - 7.5$	5.20	-0.690 ± 0.323	0.221 ± 0.353
$7.5 - 15.0$	10.19	1.006 ± 0.591	-0.521 ± 0.491
$15.0 - 100.0$	24.73	0.512 ± 0.717	-0.573 ± 0.613

Table C.4: Polarisation variables α and ν for the electroproduction ($3.6 \leqslant Q^2 \leqslant 100\,\mathrm{GeV}^2$) of inelastic J/Ψ mesons in the kinematic range $50 \leqslant W_{\gamma p} \leqslant 225\,\mathrm{GeV}$, $P^*_{T,\Psi} \geqslant 1\,\mathrm{GeV}$ and $0.3 \leqslant z \leqslant 0.9$ as a function of the photon virtuality Q^2.

Appendix D

Bin Center Correction

The measured cross sections in this analysis are average cross sections in bins of one or more variables. In order to be able to compare with theoretical predictions it is desirable to measure differential cross sections at certain values of each variable.
If the cross section in a particular analysis bin changes linearly, the measured average cross section in that bin is the same as the differential cross section at the center of the bin. However in case of a rapidly changing distribution (e.g. $\mathrm{P}_{\mathrm{T},\Psi}$) a bin center correction has to be applied in order to get the barycenter of the bin, for which the assumption that the measured cross section is equal to the differential cross section holds.
The bin center for a certain variable ζ in the bin $\zeta_1 \leqslant \zeta \leqslant \zeta_2$ can be calculated by

$$\frac{\mathrm{d}\sigma_{\gamma\mathrm{p}}}{\mathrm{d}\zeta}(\langle\zeta\rangle) = \frac{1}{\zeta_2 - \zeta_1} \int\limits_{\zeta_1}^{\zeta_2} \mathrm{d}\zeta \frac{\mathrm{d}\sigma_{\gamma\mathrm{p}}}{\mathrm{d}\zeta}\left(\zeta\right) \tag{D.1}$$

assuming a functional form for the differential cross section $\mathrm{d}\sigma_{\gamma\mathrm{p}}/\mathrm{d}\zeta$. In praxi the corrected bin centers are taken as the average values of the Monte Carlo simulation in the range of the analysis bin.

The bin center correction for the γp cross section in bins of the photon proton center of mass energy $\mathrm{W}_{\gamma p}$ has to be treated separately because the photon flux Φ_γ^{T} depends on y which is proportional to $\mathrm{W}_{\gamma p}$. For a given bin $\mathrm{W}_{\mathrm{low}} \leqslant \mathrm{W}_{\gamma p} \leqslant \mathrm{W}_{\mathrm{high}}$ the γp cross section at the expectation value $\langle \mathrm{W}_{\gamma p}\rangle$ can be expressed as

$$\sigma_{\gamma\mathrm{p}}\left(\langle \mathrm{W}_{\gamma p}\rangle\right) = \frac{\int_{\mathrm{W}_{\mathrm{low}}}^{\mathrm{W}_{\mathrm{high}}} \mathrm{dW}\ \Phi_\gamma^{\mathrm{T}}\left(\mathrm{W}\right) \cdot \sigma_{\gamma\mathrm{p}}\left(\mathrm{W}\right)}{\int_{\mathrm{W}_{\mathrm{low}}}^{\mathrm{W}_{\mathrm{high}}} \mathrm{dW}\ \Phi_\gamma^{\mathrm{T}}\left(\mathrm{W}\right)} \tag{D.2}$$

The solution of this equation requires an assumption on the functional form of $\sigma_{\gamma\mathrm{p}}\left(\mathrm{W}\right)$. The data is well described by $\sigma_{\gamma\mathrm{p}}\left(\mathrm{W}\right) \propto \mathrm{W}^\delta$, with $\delta = 0.69 \pm 0.011$. The deviation of the calculated expectation value $\langle \mathrm{W}_{\gamma p}\rangle$ from the center of the bin is of the order of $\mathcal{O}(1\ \mathrm{GeV}^2)$ in the used binning.

References

[A^+74a] J. J. Aubert et al., *Experimental Observation of a Heavy Particle J*, Phys. Rev. Lett. **33**, 1404–1406 (1974).

[A^+74b] J. E. Augustin et al., *Discovery of a Narrow Resonance in e+ e- Annihilation*, Phys. Rev. Lett. **33**, 1406–1408 (1974).

[ACL^+08] P. Artoisenet, J. Campbell, J. P. Lansberg, F. Maltoni and F. Tramontano, *Upsilon production at the Tevatron and the LHC*, (2008), 0806.3282.

[AP77] G. Altarelli and G. Parisi, *Asymptotic Freedom in Parton Language*, Nucl. Phys. **B126**, 298 (1977).

[B^+94] P. Biddulph et al., *The H1 forward muon spectrometer*, Nucl. Instrum. Meth. **A340**, 304–308 (1994).

[Bar02] S. P. Baranov, *Highlights from the* $\mathrm{k_T}$*-factorization approach on the quarkonium production puzzles*, Phys. Rev. **D66**, 114003 (2002).

[BBL92] G. T. Bodwin, E. Braaten and G. P. Lepage, *Rigorous QCD predictions for decays of P wave quarkonia*, Phys. Rev. **D46**, 1914–1918 (1992), hep-lat/9205006.

[BBL95] G. T. Bodwin, E. Braaten and G. P. Lepage, *Rigorous QCD analysis of inclusive annihilation and production of heavy quarkonium*, Phys. Rev. **D51**, 1125–1171 (1995), hep-ph/9407339.

[Beh05] O. Behnke, *Production of charm and beauty quarks at HERA*, Habilitationsschrift, Ruprecht–Karls–Universität Heidelberg, 2005.

[Ben07] D. Benekenstein, *Effizienzstudie und Optimierung der dritten Stufe des schnellen Spurtriggers bei H1*, diploma thesis, Universität Hamburg, 2007.

[Ber07] N. E. Berger, *Measurement of diffractive* ϕ *meson photoproduction with the Fast Track Trigger at H1*, PhD thesis, ETH Zürich, 2007.

[BGMS74] V. M. Budnev, I. F. Ginzburg, G. V. Meledin and V. G. Serbo, *The Two photon particle production mechanism. Physical problems. Applications. Equivalent photon approximation*, Phys. Rept. **15**, 181–281 (1974).

[BHPS80] S. J. Brodsky, P. Hoyer, C. Peterson and N. Sakai, *The Intrinsic Charm of the Proton*, Phys. Lett. **B93**, 451–455 (1980).

[BJ81] E. L. Berger and D. L. Jones, *Inelastic Photoproduction of* J/Ψ *and* Υ *by Gluons*, Phys. Rev. **D23**, 1521–1530 (1981).

[Bjo69] J. D. Bjorken, *Asymptotic Sum Rules at Infinite Momentum*, Phys. Rev. **179**, 1547–1553 (1969).

[BK97] M. Beneke and M. Kramer, *Direct* J/Ψ *and* Ψ' *polarization and cross-sections at the Tevatron*, Phys. Rev. **D55**, 5269–5272 (1997), hep-ph/9611218.

[BKV98] M. Beneke, M. Kramer and M. Vanttinen, *Inelastic photoproduction of polarised J/psi*, Phys. Rev. **D57**, 4258–4274 (1998), hep-ph/9709376.

[BL78] I. I. Balitsky and L. N. Lipatov, *The Pomeranchuk Singularity in Quantum Chromodynamics*, Sov. J. Nucl. Phys. **28**, 822–829 (1978).

[Boe07] M.-O. Boenig, *Messung des D^*-Meson-Produktionsquerschnitts in tiefinelastischer Streuung*, PhD thesis, Universität Dortmund, 2007.

[BP69] J. D. Bjorken and E. A. Paschos, *Inelastic Electron Proton and gamma Proton Scattering, and the Structure of the Nucleon*, Phys. Rev. **185**, 1975–1982 (1969).

[BR81] R. Baier and R. Ruckl, *Hadronic Production of* J/Ψ *and* Υ*: Transverse Momentum Distributions*, Phys. Lett. **B102**, 364 (1981).

[Bru07] R. Brugnera, *Measurement of inelastic* J/Ψ *helicity distribution*, (2007), ZEUS-prel-07-036.

[BZ03] S. P. Baranov and N. P. Zotov, *Deep inelastic* J/Ψ *production at HERA in the k(T)- factorization approach and its consequences for the nonrelativistic QCD*, J. Phys. **G29**, 1395–1408 (2003), hep-ph/0302022.

[CCH91] S. Catani, M. Ciafaloni and F. Hautmann, *High-energy factorization and small x heavy flavor production*, Nucl. Phys. **B366**, 135–188 (1991).

[CDF07] A. Abulencia et al. (CDF), *Polarization of J/ψ and ψ_{2S} mesons produced in $p\bar{p}$ collisions at $\sqrt{s} = 1.96$-TeV*, Phys. Rev. Lett. **99**, 132001 (2007), 0704.0638.

[CE91] J. C. Collins and R. K. Ellis, *Heavy quark production in very high-energy hadron collisions*, Nucl. Phys. **B360**, 3–30 (1991).

[CFM90a] S. Catani, F. Fiorani and G. Marchesini, *QCD Coherence in Initial State Radiation*, Phys. Lett. **B234**, 339 (1990).

[CFM90b] S. Catani, F. Fiorani and G. Marchesini, *Small x Behavior of Initial State Radiation in Perturbative QCD*, Nucl. Phys. **B336**, 18 (1990).

[Cha80] C.-H. Chang, *Hadronic production of* J/Ψ *associated with a gluon*, Nucl. Phys. **B172**, 425–434 (1980).

[Cia88] M. Ciafaloni, *Coherence Effects in Initial Jets at Small q**2 / s*, Nucl. Phys. **B296**, 49 (1988).

[CS87] J. C. Collins and D. E. Soper, *The Theorems of Perturbative QCD*, Ann. Rev. Nucl. Part. Sci. **37**, 383–409 (1987).

[dG$^+$79] J. G. H. de Groot et al., *Inclusive Interactions of High-Energy Neutrinos and anti- neutrinos in Iron*, Zeit. Phys. **C1**, 143 (1979).

[Dok77] Y. L. Dokshitzer, *Calculation of the Structure Functions for Deep Inelastic Scattering and e+ e- Annihilation by Perturbation Theory in Quantum Chromodynamics. (In Russian)*, Sov. Phys. JETP **46**, 641–653 (1977).

[E78997] D. M. Kaplan (E789), *Charmonium production in Fermilab E789*, Int. J. Mod. Phys. **A12**, 3827–3836 (1997), hep-ex/9610003.

[F$^+$74] D. J. Fox et al., *Test of Scale Invariance in High-Energy Muon Scattering*, Phys. Rev. Lett. **33**, 1504 (1974).

[Fey69] R. P. Feynman, *Very high-energy collisions of hadrons*, Phys. Rev. Lett. **23**, 1415–1417 (1969).

[FGML73] H. Fritzsch, M. Gell-Mann and H. Leutwyler, *Advantages of the Color Octet Gluon Picture*, Phys. Lett. **B47**, 365–368 (1973).

[FK72] J. I. Friedman and H. W. Kendall, *Deep inelastic electron scattering*, Ann. Rev. Nucl. Part. Sci. **22**, 203–254 (1972).

[FKS98] L. Frankfurt, W. Koepf and M. Strikman, *Diffractive heavy quarkonium photo- and electroproduction in QCD*, Phys. Rev. **D57**, 512–526 (1998), hep-ph/9702216.

[Fle04] P. Fleischmann, *Elastic* J/Ψ *production at HERA*, Phd thesis, Universität Hamburg, 2004.

[GIM70] S. L. Glashow, J. Iliopoulos and L. Maiani, *Weak Interactions with Lepton-Hadron Symmetry*, Phys. Rev. **D2**, 1285–1292 (1970).

[GL72] V. N. Gribov and L. N. Lipatov, *Deep inelastic e p scattering in perturbation theory*, Sov. J. Nucl. Phys. **15**, 438–450 (1972).

[GM64] M. Gell-Mann, *A Schematic Model of Baryons and Mesons*, Phys. Lett. **8**, 214–215 (1964).

[H193a] B. Andrieu et al. (Calorimeter Group of H1), *Results from pion calibration runs for the H1 liquid argon calorimeter and comparisons with simulations*, Nucl. Instrum. Meth. **A336**, 499–509 (1993).

[H193b] B. Andrieu et al. (Calorimeter Group of H1), *The H1 liquid argon calorimeter system*, Nucl. Instrum. Meth. **A336**, 460–498 (1993).

[H196] S. Aid et al. (H1), *Elastic and Inelastic Photoproduction of* J/Ψ *Mesons at HERA*, Nucl. Phys. **B472**, 3–31 (1996), hep-ex/9603005.

[H197a] I. Abt et al. (H1), *The H1 detector at HERA*, Nucl. Instrum. Meth. **A386**, 310–347 (1997).

[H197b] I. Abt et al. (H1), *The Tracking, calorimeter and muon detectors of the H1 experiment at HERA* , Nucl. Instrum. Meth. **A386**, 348–396 (1997).

[H197c] R. D. Appuhn et al. (SPACAL Group of H1), *The H1 lead/scintillating-fibre calorimeter*, Nucl. Instrum. Meth. **A386**, 397–408 (1997).

[H198] H1, *Subtrigger Changes (web page)*, (1998), https://www-h1.desy.de/icgi-trigger/trigchange.cgi.

[H199] C. Adloff et al. (H1), *Measurement of open beauty production at HERA*, Phys. Lett. **B467**, 156–164 (1999), hep-ex/9909029.

[H102a] Adloff, C. et al. (H1), *Inelastic leptoproduction of* J/Ψ *mesons at HERA*, Eur. Phys. J. **C25**, 41–53 (2002), hep-ex/0205065.

[H102b] Adloff, C. et al. (H1), *Inelastic photoproduction of* J/Ψ *mesons at HERA*, Eur. Phys. J. **C25**, 25–39 (2002), hep-ex/0205064.

[H107a] A. Aktas et al. (H1), *Tests of QCD factorisation in the diffractive production of dijets in deep-inelastic scattering and photoproduction at HERA*, Eur. Phys. J. **C51**, 549–568 (2007), hep-ex/0703022.

[H107b] H1, *H1oo analysis software, release 3.0.13 (web page)*, (2007), https://www-h1.desy.de/icgi-h1wiki/moin.cgi/AnalysisSoftware/Releases.

[IKKS95] H. Itterbeck, C. Keuker, C. Kleinwort and R. Starosta, *Improvement of the Trigger Timing of the H1 Digital Muon System*, H1 internal note (1995), H1-02/95-427.

[JKGW93] H. Jung, D. Krucker, C. Greub and D. Wyler, *Relativistic corrections to photoproduction of* J/Ψ, Z. Phys. **C60**, 721–730 (1993).

[JS01] H. Jung and G. P. Salam, *Hadronic final state predictions from CCFM: The hadron- level Monte Carlo generator CASCADE*, Eur. Phys. J. **C19**, 351–360 (2001), hep-ph/0012143.

[Jun92] H. Jung, *The Monte Carlo generator EPJPSI for* J/Ψ *mesons in high-energy electron proton collisions*, (1992), Aachen Tech. Hochsch. - PITHA-92-10 (92/04,rec.Apr.) 10 p.

[Kas07] R. Kastner, *Diffraktive Photoproduktion von* J/Ψ*-Mesonen bei hohen Impulsüberträgen bei* HERA , diploma thesis, Universität Hamburg, 2007.

[Kle92] Kleinwort, C. and Krüger, U. P., *Track reconstruction in the IRON*, H1 software note (1992).

[Kle07] C. Kleinwort, private communication, 2007.

[KLF77] E. A. Kuraev, L. N. Lipatov and V. S. Fadin, *The Pomeranchuk Singularity in Nonabelian Gauge Theories*, Sov. Phys. JETP **45**, 199–204 (1977).

[Kra96] M. Kraemer, *QCD Corrections to Inelastic* J/Ψ *Photoproduction*, Nucl. Phys. **B459**, 3–50 (1996), hep-ph/9508409.

[Kru01] K. Krueger, *Photoproduction of* J/Ψ *Mesons at Medium and Low Elasticities at* HERA , PhD thesis, Universität Hamburg, 2001.

[Lev95] A. Levy, *Low-x physics at HERA*, (1995), Lectures given at Strong Interaction Study Days, Kloster Banz, Germany, 10-12 Oct 1995.

[Lip75] L. N. Lipatov, *The parton model and perturbation theory*, Sov. J. Nucl. Phys. **20**, 94–102 (1975).

[LZ03] A. V. Lipatov and N. P. Zotov, *Inelastic* J/Ψ *production at HERA in the colour singlet model with k(T)-factorization*, Eur. Phys. J. **C27**, 87–99 (2003), hep-ph/0210310.

[Mal07] F. Maltoni, *QCD corrections to* J/Ψ *and* Υ *production at hadron colliders*, (2007), International Workshop on Heavy Quarkonia QWG07 (talk).

[Mar95] G. Marchesini, *QCD coherence in the structure function and associated distributions at small* x, Nucl. Phys. **B445**, 49–80 (1995), hep-ph/9412327.

[Mey97] A. Meyer, *Measurement of the structure function F2(x,*Q^2*) of the proton at low* Q^2 *with the H1 detector at HERA using the new detector components Spacal and BDC*, PhD thesis, Universität Hamburg, 1997.

[Mey98] A. Meyer, *Charmonium Production in deep inelastic scattering at HERA*, PhD thesis, Universität Hamburg, 1998.

[NSS97] B. Naroska, S. Schiek and G. Schmidt, *Lepton Identification in the H1 Detector at Low Momenta*, H1 internal note (1997), H1-05/97-518.

[PDG08] C. Amsler et al. (PDG, Particle Data Group), *Review of Particle Physics*, Phys. Lett. B667, 1 (2008), http://www-pdg.lbl.gov/.

[QWG04] N. Brambilla et al. (Quarkonium Working Group QWG), *Heavy quarkonium physics*, (2004), hep-ph/0412158.

[Rey98] D. Reyna, *Modifications to SpaCal for H1 High Luminosity Operation and the Effect on Acceptance*, H1 internal note (1998), H1-11/98-555.

[Sch94] G. A. Schuler, *Quarkonium production and decays*, (1994), hep-ph/9403387.

[Sch96] S. Schiek, *Untersuchung der inelastischen Photoproduktion von* J/Ψ*-Mesonen im H1-Detektor bei* HERA , PhD thesis, Universität Hamburg, 1996.

[Sch97] G. Schmidt, *Untersuchung der diffraktiven Photoproduktion von* J/Ψ*-Mesonen im H1-Detektor bei* HERA , PhD thesis, Universität Hamburg, 1997.

[Sjo94] T. Sjostrand, *High-energy physics event generation with PYTHIA 5.7 and JETSET 7.4*, Comput. Phys. Commun. **82**, 74–90 (1994).

[Ste05] M. Steder, *Myonidentifikation im Kalorimeter des H1 Detektors mit Neuronalen Netzen*, diploma thesis, Universität Hamburg, 2005.

[Ste07] M. Steder, *Inelastic Photoproduction of* J/Ψ *mesons at HERA*, (2007), H1prelim-07-172.

[Urb04] M. C. Urban, *The new CIP2k z-Vertex Trigger for the H1 Experiment at HERA*, PhD thesis, Universität Zürich, 2004.

[Wis03] C. Wissing, *Entwicklung eines Simulationsprogramms und Implementierung schneller Spurfitalgorithmen für den neuen H1-Driftkammertrigger*, PhD thesis, Universität Dortmund, 2003.

[ZEUS03] S. Chekanov et al. (ZEUS), *Measurements of inelastic* J/Ψ *and* Ψ' *photoproduction at HERA*, Eur. Phys. J. **C27**, 173–188 (2003), hep-ex/0211011.

[ZEUS05] S. Chekanov et al. (ZEUS), *Measurement of inelastic* J/Ψ *production in deep inelastic scattering at HERA*, Eur. Phys. J. **C44**, 13–25 (2005), hep-ex/0505008.

[Zwe64a] G. Zweig, (1964), CERN-TH-412 (unpublished).

[Zwe64b] G. Zweig, *An SU(3) Model for Strong Interaction Symmetry and its Breaking. 2*, (1964), CERN-TH-412.

Danksagung

Wir sind nicht nur die Kinder unserer Eltern. Und dennoch haben sie großen Einfluß darauf 'was' und in noch viel stärkerem Maße 'wie' wir geworden sind. Ich danke Euch, liebe Familie, daß Ihr wesentlich dazu beigetragen habt, die Voraussetzungen für diese Arbeit zu schaffen.
Dir, meine liebe Lea, danke ich für jeden Tag! Deine ebenso ausdauernde wie aufmunternde Unterstützung hat das Schreiben dieser Arbeit sehr erleichtert.

Diese Arbeit wäre nie begonnen worden, ohne daß Frau Prof. Dr. Beate Naroska durch Ihre ansteckende Begeisterung für die Teilchenphysik mein Interesse an diesem Thema geweckt hätte. Ich empfinde große Dankbarkeit für die vorbildliche Betreuung meiner Diplom- und Doktorarbeit, umso mehr da ich Frau Naroska zu meinem tiefen Bedauern nicht mehr persönlich danken kann.

Mein Dank geht an Herrn PD Dr. Andreas Meyer, der sich bereit erklärt hat, die Betreuung meiner Arbeit sowie die Anfertigung des Erstgutachtens zu übernehmen. Aber, lieber Andreas, das wäre zu wenig. Ebenso denke ich gerne an die Zeit in der H1 Halle und die gemeinsame Arbeit am Myonsystem zurück. Ich danke Dir für Deine Unterstützung bei den preliminary requests und nicht zuletzt ganz besonders dafür, daß Du immer Zeit für die Betreuung meiner Arbeit gefunden hast, ungeachtet Deiner Doppelbelastung der letzten Monate.

Ich danke Herrn Prof. Dr. Robert Klanner für seine Anmerkungen zur Dissertation sowie für die Übernahme des Zweitgutachtens und Herrn JProf. Johannes Haller dafür, daß er sich bereit erklärt hat, Gutachter der Disputation zu sein.

Hilfreiche Kommentare und Anmerkungen haben in den letzten Wochen sehr dazu beigetragen, Verständlichkeit und Lesbarkeit dieser Arbeit zu verbessern. Liebe Barbara, liebe Claudia, liebe Lea, liebe Sanna, lieber Andreas, lieber Benno, lieber Hannes, lieber Joachim, lieber Shiraz, ich danke Euch herzlich für alle sprachlichen Verbesserungen und inhaltlichen Hinweise, aber auch für jedes Lob, das ich ebenso gerne aufgenommen habe wie ich versucht habe, Eure Anregungen einzuarbeiten. Selbstverständlich nehme ich alle verbleibenden Fehler auf meine Kappe.

Ein Dankeschön geht an alle Mitglieder der H1 Kollaboration, insbesondere der heavy flavour Arbeitsgruppe, für die angenehme und fruchtbare Zusammenarbeit in den letzten Jahren.

Abschließend möchte ich mich bei all denjenigen bedanken, die mich in den letzten Jahren von Zeit zu Zeit durch Verzehr von Heißgetränken, Klettern, Theater spielen, Fußball gucken, Grillen oder 'curry chicken' vom eigentlichen Thema dieser Dissertation abgelenkt haben.